Technical University Delft

Transport Phenomena group

Extending a RANS Solver with heat and pollution modules for dispersion problems in urban areas with vegetation

Author:
Espen Tierolff
4537033

Committee:
Assoc. Prof. S. Kenjeres, Dr., Dipl.-Ing. (supervisor)
Prof. C.R. Kleijn, Dr., Ir.
Prof. D.J.E.M. Roekarts, Dr.
Dr. S. J. de Roode

To obtain the degree of Master of Science at the Delft University of Technology, to be defended publicly on June 18, 2018

May 31, 2018

Abstract

Currently, 54% of the general population lives in urban areas. This number is estimated to increase to 66% by 2050. Urbanization is generally linked to several phenomena that are detrimental to the overall quality of life; the urban heat island effect, and the decrease of air quality due to pollutants. The addition of vegetation to urban areas is generally seen as the best measure to combat these phenomena, due to their suggested filtering and cooling capacity. Currently, both phenomena are studied as separate processes, but research suggest that the cooling power of vegetation is linked to the amount of pollution that is present. This calls for a numerical implementation that is able to accurately model both the filtering, and cooling effect such that the interplay between them can be studied in the future.
In this work, an existing RANS $k-\epsilon$ solver is extended with the dry-deposition model to determine the filtering capacity of the vegetation, and the leaf energy balance model to determine the cooling effect of the vegetation.

Using the dry deposition model, we were able to accurately reproduce experimental measurements of the filtering capacity of a hawthorn hedge in an open field, obtained by Tiwary et al. [2006]. We assumed that the filtering took place due to both needle-like and broad leaf collectors. The same case was studied by Šíp and Beneš [2016], who obtained similar results, but used a different mixing parameters of the collector types. We concluded that additional studies are needed to determine the importance of the collector mixing parameters for multiple species, before the dry deposition model can be considered as valid.

Using the leaf energy balance model, we were able to determine the cooling power of a simple vegetation block, exactly reproducing the results obtained by [Manickathan et al., 2017]. Using the leaf energy balance model, we were not able to reproduce experimental measurements of the leaf temperature of potted impatiens, obtained by [Kichah et al., 2012]. This was caused by the nature of the flow, which proved to be barely turbulent and outside of the scope of our RANS $k-\epsilon$ solver. We concluded that the leaf energy balance model needs to tested against other experimental measurements, obtained under different flow conditions. As of yet, we can not determine if the model is able to accurately reproduce experimental measurements.

Preface

This thesis has been written as one of the final parts of my master's programme "Applied Physics: Transport Phenoma and Fluid Flow" at the Technical University Delft. I would like to express my gratitude towards Saša Kenjereš for guiding into the world of in-house Navier-Stokes solvers, asking critical questions and providing me with excellent guidance during the 9 months that I worked on this thesis. I would also like to thank Stefan Zwinkels for helping me in the early stages of exploring the wondrous world of Fortran.

Graag wil ik ook een aantal mensen bedanken die dit helse project dragelijk hebben gemaakt. De UvAstrijders voor alle koffiepauzes, peukies en goede gesprekken in de bieb, Derde Oost, voor de veilige thuisbasis in tijden van nood, Weekend in DS voor die zeldzame weekenden waar de knop even om mocht, en natuurlijk mijn ouders. Zonder jullie steun was dit allemaal niet gelukt.

Contents

1 Introduction

Currently, 54% of the general population lives in urban areas [United Nations, 2014]. Urbanization is generally linked to several phenomena that are detrimental to the overall quality of life; the decrease of air quality and the increase of local temperature; the urban heat island effect [Gromke et al., 2015], [Yang et al., 2017]. Taha [1997] states that the air pollutant concentration can be 10 $\times$ higher, and that the local temperature can be on average $2°C$ higher in urban areas compared to rural ones. According to Gkatsopoulos [2017], the temperature difference between urban and rural settings can be $10°C$.

The percentage of the population living in urban areas is estimated to increase to 66% by 2050 [United Nations, 2014], which means that a large portion of the total population will be subjected to these detrimental phenomena. This is reflected by the fact that it is expected that air pollution will account for the majority of environmental deaths by 2050 [Matter and Supply, 2012], and that the effects of climate change will be most prevalent in urban areas [Jacob and Winner, 2009]. Currently, the number of premature deaths related to air quality is 1 million, each year [World Health Organization, 2006].

Generally, vegetation is seen as the most fitting measure to combat both phenomena. Vegetation decreases the local temperature by shading and evapotranspiration, potentially alleviating the urban heat island effect Taha [1997], Gkatsopoulos [2017], [Shashua-Bar et al., 2009], [Rahman et al., 2011], [McPherson et al., 1997], Takakura et al. [2000], Bauerle et al. [2009]. The air quality is said be improved due to the filtering capacity of the vegetation, lowering the concentration of harmful pollutants. Also, carbon dioxide is absorbed to perform photosynthesis [McPherson et al., 1997], [Nowak et al., 2002].

However, simply adding vegetation to any urban setting does not always achieve the desired result. Gromke and Blocken [2015] observed that in a street canyon, a simple road flanked by parallel buildings, the concentration of pollutants can increase due to the presence of vegetation. Shashua-Bar et al. [2009] performed temperature measurement in a hot, dry climate and observed that the configuration of the test site had a large influence on the result. This is caused by the influence of the flow field on the dispersion of the heat and pollutant concentration [Barnes et al., 2014]. Vegetation can have a significant effect on the flow field [Kenjereš and ter Kuile, 2013] [Šíp and Beneš, 2016]. This means that in order to combat the urban heat island effect, and the decrease of air quality, configurations have to be the tested and simulated carefully to determine their effectiveness. Gromke et al. [2015] studied the transport of heat in a complex urban setting. The cooling effect of the vegetation was included by specifying a uniform cooling power term, based on the measurements performed by Rahman et al. [2011]. Kichah et al. [2012] performed temperature measurements and simulations on impatiens to validate a leaf energy balance model that eliminated the need for a pre-specified cooling power term. Manickathan et al. [2017] improved upon this research by including additional effects of the vegetation on the flow field.

It is clear that pollution and heat are being treated as separate entities. Both can be modelled using their respective models, but no connection exists between them. However, there is clear evidence that the biological function of vegetation is related to the presence of pollution. Smith [1974] states that the presence of pollution can lead to reduced photosynthetic rate, disease induction or even acute morbidity. Stomatal function is also reported to be heavily influenced by the presence of pollutants [Darrall, 1989] [Allen, 1990] [Baldocchi et al., 1987]. In order to numerically study this effect, an implementation is needed that is able to model

both the concentration and heat effects of vegetation, before being able to propose and test a numerical relation between pollution and heat.

This brings us to the goal of this research. This research will focus on the extension of an existing RANS $k-\epsilon$ solver with numerical models for the effect of vegetation on the dispersion of heat and pollution. The aim of this work is to be able to accurately model these separate effects, such that further research can be conducted to numerically study the connection between the presence of pollution and the biological function of vegetation. Consequently, the sub questions of this research are:

- *Can the existing RANS $k-\epsilon$ solver be extended with a numerical model in such a way that it is able to accurately reproduce experimental measurements of the effect of vegetation on pollution dispersion?*
- *Can the existing RANS $k-\epsilon$ solver be extended with a numerical model in such a way that it is able to accurately reproduce experimental measurements of the effect of vegetation on the dispersion of heat?*

2 Velocity field

In order to obtain the flow field, we solve the Reynolds-averaged Navier-Stokes equation:

$$\frac{\partial U_i}{\partial t} + U_j \frac{\partial U_i}{\partial x_j} = -\frac{1}{\rho}\frac{\partial P}{\partial x_i} + \frac{\partial}{\partial x_j}\Big[\nu(\frac{\partial U_i}{\partial x_j} + \frac{\partial U_j}{\partial x_i}) - \overline{u_i' u_j'}\Big] + S_{m,i} \tag{1}$$

where ν is the viscosity, $\overline{u_i' u_j'}$ are the Reynolds stresses and $S_{m,i}$ is sink/source term. The Reynolds stresses are modelled using an eddy-viscosity model:

$$\overline{u_i' u_j'} = \nu_t(\frac{\partial U_i}{\partial x_j} + \frac{\partial U_j}{\partial x_i}) + \frac{2}{3}k\delta_{i,j} \tag{2}$$

where ν_t is the turbulent viscosity and k is the TKE, which is simply $\frac{1}{2}\overline{u_i u_i}$. The turbulent viscosity is modelled as:

$$\nu_t = C_\mu k T \tag{3}$$

where C_μ is a model constant and $T = \frac{k}{\epsilon}$. ϵ is the viscous dissipation of TKE, defined as:

$$\epsilon = \overline{\Big(\frac{\partial u_i'}{\partial x_j}\Big)^2} \tag{4}$$

Transport equations for ϵ and k are needed to close the model:

$$\frac{\partial k}{\partial t} + U_j \frac{\partial k}{\partial x_j} = \frac{\partial}{\partial x_j}\Big[(\nu + \frac{\nu_t}{\sigma_k}\frac{\partial k}{\partial x_j}\Big] - \overline{u_i' u_j'}\frac{\partial U_i}{\partial x_j} - \epsilon + S_k \tag{5}$$

$$\frac{\partial \epsilon}{\partial t} + U_j \frac{\partial \epsilon}{\partial x_j} = \frac{\partial}{\partial x_j}\Big[(\nu + \frac{\nu_t}{\sigma_\epsilon}\frac{\partial \epsilon}{\partial x_j}\Big] - C_{1\epsilon}\overline{u_i' u_j'}\frac{\partial U_i}{\partial x_j}\frac{\epsilon}{k} - C_{2\epsilon}\frac{\epsilon^2}{k} + S_\epsilon \tag{6}$$

where σ_k, σ_ϵ, $C_{1\epsilon}$ and $C_{2\epsilon}$ are model constants. S_k, S_ϵ are the respective sink/source terms of the TKE and viscous dissipation of TKE.

The effect of vegetation on the flow field is included using the sink/source terms that are present in each transport equation; $S_{m,i}$, S_k, and S_ϵ. The vegetation acts on the flow through several interactions, which are translated to mathematical sink/source terms. First of all, some streamlines will simply hit the vegetation, the same way air flow interacts with a solid obstacle like a building. This is the effect of the form drag. This causes large-scale turbulent motion, which eventually cascades to small eddies where viscous dissipation occurs at the smallest scale. Secondly, the flow hits the individual leaves. This creates small eddies that are roughly the size of the leaves itself. This bypasses a large portion of the turbulence cascade, causing it to reach the dissipative state significantly faster. This process is unique to porous obstacles.

2.1 Sink/Source terms

The sink/source term in the moment equation is the form drag $F_{D,i}$. The expression for the form drag is relatively straightforward:

$$S_{m,i} = \frac{1}{2}C_D a |U| U_i \tag{7}$$

where a is the Leaf Area Density in $\frac{m^2}{m^3}$ and C_D is the drag coefficient.

The sink/source terms of k and ϵ depend on the shortcut of the cascade process and the generation of large eddies due to the form drag. The individual leaves generate eddies that are of the size of the leaves itself. The collective of smaller eddies generate by each individual leaf is called the wake. So, mean flow motion is converted into wake turbulence. The vegetation obstacle itself generates eddies that are of the size of the obstacle itself due to shear [Tan, 2009]. This process is displayed in figure (1). The eddies generated by the leaves are dissipated more rapidly due to the short cut of the energy cascade. The shortcut of the cascade process scales with the product of the velocity and the TKE. The production of TKE due to the form drag scales with the cube of the velocity. This gives us the following expression for the TKE source term:

$$S_k = \frac{1}{2} C_d a \Big(\beta_p |U^3| - \beta_d |U| k \Big) \tag{8}$$

where β_p and β_d are model constants that describe the significance of these processes. The sink/source term of ϵ is derived from S_k. However, the dimension of k is $\frac{m^2}{s^2}$, and the dimension of ϵ is $\frac{m^2}{s^3}$. Consequently, S_k needs to be divided by s to obtain the correct dimension. The characteristic time is defined as $\frac{k}{\epsilon}$. This gives us the following expression for S_ϵ:

$$S_\epsilon = \frac{1}{2} C_d a \Big(C_{4\epsilon} \beta_p |U^3| \frac{\epsilon}{k} - C_{5\epsilon} \beta_d |U| \epsilon \Big) \tag{9}$$

where $C_{4\epsilon}$ and $C_{5\epsilon}$ are additional model constants.

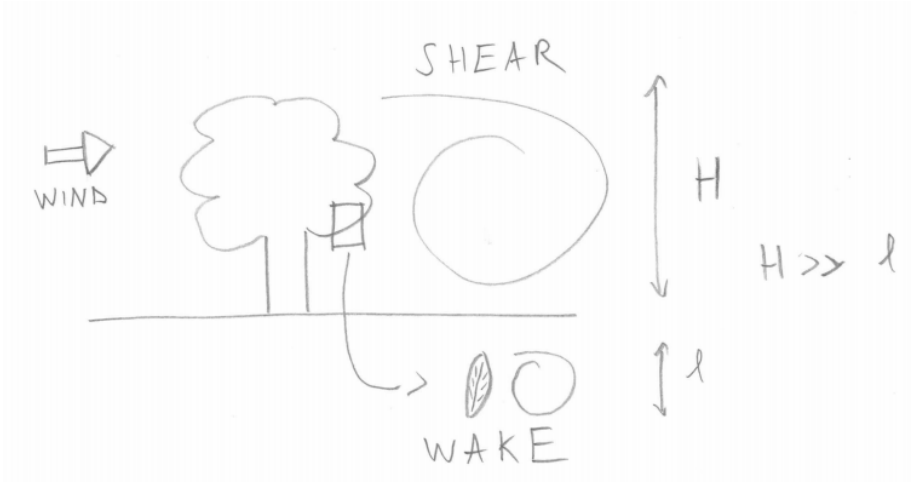

Figure 1: The generation of different sized eddies due to vegetation

We see that the modelling of velocity field relies heavily on a number of different constants. There is little debate on the values of the constants related to the standard RANS equations. The following values were proposed by Launder and Sharma [1974] and are still used: $\Big(C_{1\epsilon}, C_{2\epsilon}, \sigma_k, \sigma_\epsilon, C_\mu \Big) = \Big(1.44, 1.92, 1.0, 1.3, 0.09 \Big)$. For the constants related to the effect on vegetation, the model developed by Katul et. al in 2004 is used, as it provided the best overall agreement with measured TKE data, and proved to be more numerically stable than other proposed models [Kenjereš and ter Kuile, 2013]. This gives us the following values: $\Big(\beta_p, \beta_d, C_{4\epsilon}, C_{5\epsilon} \Big) = \Big(1.0, 5.1, 0.9, 0.9 \Big)$.

3 Temperature effects

The temperature is affected by the presence of vegetation due to transpirational cooling. The cooling process can be seen as as a temperature sink. The transport equation for the Reynolds-averaged temperature is:

$$\frac{\partial T}{\partial t} + U_j \frac{\partial T}{\partial x_j} = \frac{\partial}{\partial x_j}\Big[\frac{\nu}{\mathrm{Pr}}\frac{\partial T}{\partial x_j} - \overline{T' u_j'}\Big] + S_T \tag{10}$$

where Pr is the Prandtl number and $\overline{T' u_j'}$ are the thermal stresses. The thermal stresses are modelled using the Simple Gradient Diffusion Hypothesis:

$$\overline{T' u_j'} = -\frac{\nu_t}{\mathrm{Pr}_t}\frac{\partial T}{\partial x_j} \tag{11}$$

where Pr_t is the turbulent Prandtl number. The Prandtl number depends on the geometry of the problem, but generally a turbulent Prandtl number ranging from 0.7 to 0.9 is used [Launder and Sharma, 1974] [Baik et al., 2003]. In this work, $Pr_t = 0.71$ is used, in accordance with Manickathan et al. [2017].

3.1 Sink/Source Terms

Evapotranspiration is responsible for the sink term in the transport equation of Reynolds-averaged temperature. Due to presence of vegetation, heat is absorbed to evaporate moisture that is transpired through the leaves of the vegetation. Heat is extracted from the air and the vegetation itself. Also, heat is exchanged between the vegetation and the air. These processes rely on the temperature difference of the leaves and the air, the heat capacity of the air c_p, and the velocity of the air flowing past the leaves. Using the Buckingham Pi Theorem, dimensional analysis can be performed to obtain the following scaling:

$$S_T \propto \Big(\frac{c_p(T - T_{leaf})}{|\overline{U}|^2}\Big)^{\alpha} \tag{12}$$

Generally, the scaling factor α is assumed to be 0, such that the thermal heat sink of the vegetation is simply an empirical constant [Dimoudi and Nikolopoulou, 2003], [Gromke et al., 2015]. For example, the experimental data from Rahman et al. [2011], that states that the cooling power of vegetation ranges from from 284 to 335 $\frac{W}{m^3}$, is used in the CFD study by Gromke et al. [2015].

However, it is not very likely that these experimental values are universally applicable. Therefore, the model proposed by Manickathan et al. [2017] is used to calculated the sensible heat flux from the vegetation into the air. This model is discussed in the next section.

3.1.1 Leaf Energy Balance Model

The model by Manickathan et al. [2017] is based on the assumption that the cooling of the air due to the presence of water vapour is negligible. The presence of water vapour cools the leaves, which in turn cool the surrounding air by sensible heat flux. The authors base these assumptions on the findings by Hiraoka [2005]. As a result, the sink term takes the following form:

$$S_T = a\frac{q_{sen.leaf}}{\rho c_p} \tag{13}$$

where $q_{sen,leaf}$ is the sensible heat flux in $\frac{W}{m^2}$. The sensible heat flux from the leaf into the air is determined using the leaf energy balance:

$$q_{rad,leaf} - q_{sen,leaf} - q_{lat,leaf} = 0 \tag{14}$$

The leaves absorb heat due to the incoming radiative flux $q_{rad,leaf}$, and lose heat due the sensible heat flux into the air $q_{sen,leaf}$, and the latent heat flux into the air $q_{lat,leaf}$ due to evapotranspiration. Water is vaporized and expelled through the leaf stomata. A schematic representation of the energy balance of the leaf surface is shown in figure (2). Each flux experiences resistance in the form of aerodynamic resistance r_a and/or stomatal resistance r_s.

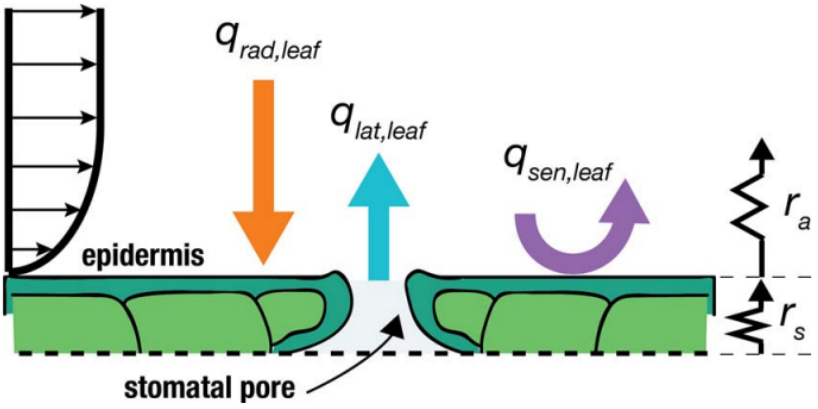

Figure 2: A schematic representation of the leaf energy balance. The leaf loses heat due to the sensible heat flux with the air and the latent heat flux due to evapotranspiration. The leaf absorbs heat due to the incoming radiative flux. Each flux experiences resistance in the form of aerodynamic resistance and/or stomatal resistance. The figure is obtained from Manickathan et al. [2017]

.

The latent heat flux is defined as:

$$q_{lat,leaf} = L_v g_{v,leaf} \tag{15}$$

where $L_v = 2.5 \times 10^6 \ \frac{\text{J}}{\text{kg}}$ is the latent heat of vaporization, and $g_{v,leaf}$ is the water vapor flux into the air, defined as:

$$g_{v,leaf} = \frac{\rho R_a}{p R_v} \frac{1}{r_a + r_s} (p_{v,leaf} - p_v) \tag{16}$$

where $R_a = 287.0 \ \frac{1}{\text{kgK}}$ is the gas constant of dry air, $R_v = 462.5 \ \frac{1}{\text{kgK}}$ is the gas constant of water vapour, $p_{v,leaf}$ is the vapour pressure at the leaf and p_v is the vapor pressure of the air above the boundary layer. The authors assume that the vapor pressure at the leaf can be approximated as the saturated vapor pressure at the leaf temperature. In this work, the Magnus-Tetens equation is used to calculated the saturated vapor pressure as function of the temperature.
The vapor pressure of the air is a function of the atmospheric pressure and the humidity ratio

w, which expresses the moisture content of the air in kilograms of water per kilogram of dry air. The vapor pressure is calculated from the humidity ratio using the following relation:

$$w = \frac{R_a}{R_v} \frac{p_{vapor}}{P - p_{vapor}} \tag{17}$$

The sensible heat flux is defined as:

$$q_{sen,leaf} = \frac{2\rho c_p}{r_a}(T_{leaf} - T) \tag{18}$$

r_a can be interpreted as the aerodynamic resistance against the boundary layer and is calculated as:

$$r_a = C_a \Big(\frac{l}{|\overline{U}|} \Big)^{\frac{1}{2}} \tag{19}$$

where $C_a = 130 \ \frac{s^{\frac{1}{2}}}{m}$ is a proportionality factor. The stomatal resistance is related to the aerodynamic resistance, the concentration of vapor in the air and the incoming shortwave radiation $q_{r,sw}$. The influence of the vapor concentration is included in the model by using the difference between the saturation vapor pressure and the vapor pressure of air $D = p_{v,sat} - p_v$. The authors use the following model to determine its value:

$$r_s = r_{s,min} \frac{a_1 + q_{r,sw}}{a_2 + q_{r,sw}} \Big(1 + a_3 (D - D_0)^2 \Big) \tag{20}$$

where $a_1 = 169 \ \frac{\mathrm{W}}{\mathrm{m}^2}$, $a_2 = 18 \ \frac{\mathrm{W}}{\mathrm{m}^2}$, $a_3 = 5 \times 10^{-6} \ \frac{\mathrm{N}}{\mathrm{m}^2}$, and $D_0 = 1.2 \times 10^3 \ \frac{\mathrm{N}}{\mathrm{m}^2}$ are empirical constants. $r_{s.min}$ is the minimum stomatal resistance and depends on the plant type. For deciduous plants, its value is 400 $\frac{\mathrm{m}}{\mathrm{s}}$.

$q_{rad,leaf}$ can be calculated using the fact that the divergence of the total radiative q_r flux in the air at the leaf is equal to absorption of radiation by the leaf area of the vegetation:

$$\Big(\nabla q_r \Big)_{leaf} = a q_{rad,leaf} \tag{21}$$

The total radiative flux consists of short- and long-wave radiation:

$$q_r = q_{r,sw} + q_{r,lw} \tag{22}$$

such that

$$q_{rad,leaf} = \frac{\nabla q_{r,sw} + \nabla q_{r,lw}}{a} \tag{23}$$

The short-wave radiative flux within the vegetation is calculated using the Beer-Lambert law, under the assumption that the sun is directly above the vegetation.

$$q_{r,sw}(z) = q_{r,sw,0} e^{-\Big(\beta \int_z^H a(z) dz \Big)} \tag{24}$$

where $q_{r,sw,0}$ is the short-wave radiative flux at the top of the vegetation. $\beta = 0.78$ is the extinction coefficient of short-wave radiation within vegetation. he authors use simplified empirical formula's to approximate the gradients of the long-wave radiation, derived from greenhouse studies:

$$\nabla q_{r,lw} = C_{lw} \frac{q_{r,lw}}{H} \tag{25}$$

where $C_{lw} = 0.04$ is a model constant and $q_{r,lw}$ is the long wave radiative flux at the reference temperature. The long-wave radiative flux depends on the temperature of the ground and the amount of clouds in the sky. The only remaining unknown is T_{leaf}. Equation (3.6) and equation (3.9) are combined to yield the following expression:

$$T_{leaf} = T + r_a \frac{q_{rad,leaf} - q_{lat,leaf}(T_{leaf})}{2\rho c_p} \tag{26}$$

Using the listed set of equations, the leaf temperature is determined, and the sink term is compute using equation (3.9).

It is clear that the leaf temperature, and therefore the cooling power, heavily depend on the humidity of the air around the leaves. It is likely that the humidity will not be uniform within the vegetation. Therefore, we need to solve an additional PDE that deals with the transport of the humidity ratio. The Reynolds-averaged transport equation for the humidity ratio is:

$$\frac{\partial \bar{w}}{\partial t} + U_j \frac{\partial \bar{w}}{\partial x_j} = \frac{\partial}{\partial x_j}\left[\frac{\nu}{\mathrm{Pr}} \frac{\partial \bar{w}}{\partial x_j} - \overline{w' u_j'}\right] + S_w \tag{27}$$

where the turbulent humidity flux is modelled in a similar way as the thermal stresses, using the following equation:

$$\overline{w' u_j'} = -\frac{\nu_t}{\mathrm{Pr}_t} \frac{\partial \bar{w}}{\partial x_j} \tag{28}$$

S_w is the humidity source term due to the presence of vegetation, and depends on the vapor mass flux into the air, g_v.

$$S_w = a \frac{g_v}{\rho} = a \frac{q_{lat,leaf}}{\rho L_v} \tag{29}$$

This means that we have a model where almost all variables are co-dependent. The most important coupling is the one between the latent heat flux, the air temperature, the leaf temperature and the humidity of the air. These interactions are displayed in the following figure:

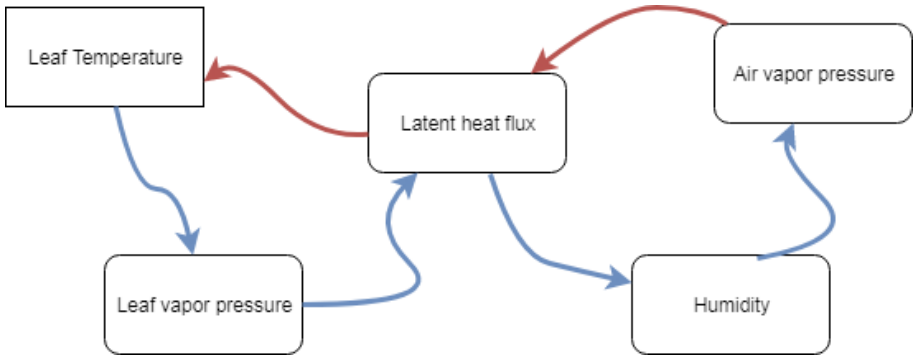

Figure 3: This schematic represents the coupling of T_{leaf}, $p_{v,leaf}$, $p_{v,air}$, w and $q_{lat,leaf}$. The blue arrows represent a positive coupling, and the red arrow represent a negative coupling.

The leaf temperature decreases as the latent heat flux increases. This causes the leaf vapor pressure to decrease, which again causes the latent heat flux to decrease. When the latent heat

flux decreases, the humidity also decreases, just like the air vapor pressure. The drop of the vapor pressure causes the latent heat flux to increase again.

Manickathan et al. [2017] propose the following procedure to obtain the correct leaf temperature:

1. Determine the radiative flux using equation (3.14)
2. Calculate the aerodynamic and stomatal resistance using equation (3.10) and (3.11)
3. Set $T_{leaf} = T$ as an initial estimate
4. Calculate the saturated vapour pressure at T_{leaf}
5. Calculate the latent heat flux using equation (3.7)
6. Adjust the leaf temperature using equation (3.18)
7. Repeat steps 4-6 until T_{leaf} has converged

In this work, the convergence limit is 10^{-4}.

4 Pollutant dispersion

We assume that the diameter and concentration of the particles is sufficiently low such that the velocity field is not affected by the presence of pollutants. This means that the RANS remains the same. The transport equation for the concentration of the pollutant is:

$$\frac{\partial C}{\partial t} + U_j \frac{\partial C}{\partial x_j} = \frac{\partial}{\partial x_j}\Big[D\frac{\partial C}{\partial x_j} - \overline{C' u_j'}\Big] + S_C \tag{30}$$

where D is the diffusion coefficient and S_C is the sink/source term related to concentration. The turbulent concentration flux term is modelled as:

$$\overline{C' u_j'} = -\frac{\nu_t}{\mathrm{Sc}_t}\frac{\partial C}{\partial x_j} \tag{31}$$

Where Sc_t is the turbulent Schmidt number. There is no consensus on the correct turbulent Schmidt number for urban canopy flows. Generally, values ranging between 0.5 and 0.9 are used [Jeanjean et al., 2015] [Baik et al., 2003] [Gualtieri et al., 2017]. However, a value of 0.3 is best suited when modelling a single building, as turbulent fluctuations are often underestimated due to the fact that RANS does not correctly produce unsteady vortex shedding [Tominaga and Stathopoulos, 2007]. However, reasonable results are obtained by Šíp and Beneš [2016] when modelling edge flow using $\mathrm{Sc}_t = 0.7$.

4.1 Sink/Source terms

The sink/source term of the Reynolds-averaged concentration is determined by 2 processes; gravitational settling and dry deposition due to the vegetation. So $S_C = S_C^G + S_C^D$. Their respective expressions are relatively straightforward:

$$S_C^G = -\frac{\partial}{\partial x_i}\Big(C U_{s,i}\Big) \tag{32}$$

where $U_{s,i} = (0, 0, U_s)$ is the settling velocity. This is calculated using a force balance between drag and gravitational pull:

$$F_D = F_G \tag{33}$$

$$6\pi\mu U_s \frac{d_p}{2} = \frac{4}{3}\pi(\frac{d_p}{2})^3 \rho_p g \tag{34}$$

$$U_s = \frac{d_p^2 \rho_p g}{18\mu} \tag{35}$$

$$\tag{36}$$

The Cunningham Correction factor C_c is added to account for the non-continuum effects, as proposed by E Cunningham [1910]. This gives us the following expression:

$$U_s = \frac{d_p^2 \rho_p g C_c}{18\mu} \tag{37}$$

The Cunningham Correction factor is defined as:

$$C_c = 1 + \frac{2\lambda}{d_p}\Big(1.257 + e^{-1.1\frac{d_p}{2\lambda}}\Big) \tag{38}$$

where $\lambda = 0.066\mu$m is the mean free path of the particle. The expression for the Cunning-Ham Correction factor is simplified to facilitated its numerical implementation:

$$C_c = 1 + 3.334\frac{\lambda}{d_p} \tag{39}$$

The simplification causes a maximum difference of 12%, for a particle diameter of 0.12 μm. A laminar boundary is assumed to surround the individual leaves [Šíp and Beneš, 2016].

The sink term due to dry deposition is also straightforward:

$$S_C^D = -aU^D C \tag{40}$$

where U^D is deposition velocity, which consists of contributions due to Brownian motion, interception, impaction and sedimentation of the particle [Šíp and Beneš, 2016]:

$$U^D(d_p) = f(U_b^D, U_{IM}^D, U_{IN}^D, U_{TI}^D, U_{sedi}^D) \tag{41}$$

Deposition happens due to collection on two types of collectors; needle-like collectors and broad leaf collectors. Slightly different models are used for both collectors. For needle-like collectors, the model as described by Petroff et al. [2008] is used. For broad leaves, the model described by Petroff et al. [2009] is used. Both models are presented in the following sections. Some of the modifications proposed by Šíp and Beneš [2016] are implemented.

The model starts with an elemental deposition velocity, u_i^D, which is the deposition velocity for a single leaf. The i subscript indicates the deposition process. Then, the sink of concentration for a single leaf is:

$$S_{C,leaf}^D = -sC\sum_i u_i^D \tag{42}$$

where s is the area of the individual leaf. The elemental deposition velocity can vary within a reference volume. This dealt with by averaging the elemental deposition velocity of a reference volume D_{ref}, to obtain the average deposition velocity $U_{d,i}$:

$$U_i^D = \int_{D_{ref}(\Psi_{i,j})} u_i^D \Pi_j \phi_j \delta\Psi_{i,j} \tag{43}$$

where $\Psi_{i,j}$ are the parameters that influence the deposition velocity and ϕ_j is the probability density function of associated with each parameter within the reference volume.

4.1.1 Brownian Motion

The elemental Brownian motion deposition velocity contribution is modelled as diffusion over smooth infinite cylinders or planes for needles and leaves respectively. This processes depends on the boundary layer of the obstacle, which makes it dependent on the Reynolds number. It also depends on the Sherwood number, Sh, which is a measure of mass transfer due to convection over diffusion. The elemental Brownian deposition is calculated using the following relation:

$$u_b^D = Sh\frac{D_B}{d_n} \tag{44}$$

or

$$u_b^D = Sh\frac{D_B}{l} \tag{45}$$

for broad leaf collectors, where $D_B = \frac{C_c k_b T}{3\pi\mu d_p}$ is the Brownian diffusion coefficient, l is the leaf width, and d_n is the needle diameter. Sh is related to the flow regime, according to the formula:

$$Sh = C_b Sc^{1/3} Re^{n_B} \tag{46}$$

where Re is the Reynolds number calculated with the needle diameter or the leaf width. C_B and n_B are model parameters that depend on the state of the boundary layer. S_c is the Schmidt number, calculated as $\frac{\nu}{D_B}$, giving us the following expression for the elemental deposition velocity.

$$u_b^D = C_b S_c^{-2/3} Re^{n_B - 1} |U| \tag{47}$$

The random parameters on which the Brownian Motion deposition depends are the surface area of the leaf or needle, and the particle size. The particle diffusion model assumes infinitely long objects, so the surface area of the leaf or needle depends on the leaf width l or the needle diameter d_n. This gives us the following expression for the average Brownian deposition velocity:

$$U_b^D = \int_{D(d_n)} u_b^D(d_n) \Big(\frac{x}{\bar{d_n}}\Big)^{n_B} \phi_{d_n}(x) dx \tag{48}$$

$$= u_b^D(\bar{d_n}) \int_{D(d_n)} \Big(\frac{x}{\bar{d_n}}\Big)^{n_B} \phi_{d_n}(x) dx \tag{49}$$

$$= u_b^D(\bar{d_n}) I_B \tag{50}$$

for needle like collectors and

$$U_b^d = \int_{D(l)} u_b^d(l) \Big(\frac{x}{\bar{l}}\Big)^{n_B} \phi_l(x) dx \tag{51}$$

$$= u_b^d(\bar{l}) \int_{D(l)} \Big(\frac{x}{\bar{l}}\Big)^{n_B} \phi_l(x) dx \tag{52}$$

$$= u_b^d(\bar{l}) I_B \tag{53}$$

for broad leaf collectors.

4.1.2 Interception

Interception happens when particles follow the streamlines of the flow, but still get attached to a leaf due to its vicinity to the surface of the leaf. This happens when the distance between the particle and the leaf is less than half the particle diameter. This process is displayed in 4. The elemental deposition velocity for needle-like collectors is formulated as:

$$u_{IN}^D = \frac{s_x}{s} \frac{2d_p}{d_n} |U| \tag{54}$$

where s_x is the projection of the needle area onto the x-plane. The varying parameters are the needle diameter, the needle surface and the orientation angles of the needle. The orientation angles are the θ, the angle between the leaf normal and the flow direction, and ψ, the angle between the leaf normal and the $\hat{z}$ axis. These are assumed to be independent. This gives us the following expression for the average deposition velocity:

$$U_{IN}^D = 2d_p |U| \int_{D(s),D(d_n),D(\theta),D(\psi)} \frac{1}{d_n} \frac{s_x}{s} \phi_\psi(x) \phi_\theta(x) \phi_{d_n}(x) \phi_s(x) dx \tag{55}$$

$$= 2k_x \frac{d_p}{\bar{d_n}} |U| \tag{56}$$

where k_x is the result of the spatial average of s_x/s. This value is largely determined by the probability distributions of the orientation angles. The projection of the surface onto the direction of the flow is given by:

$$s_x = \frac{s}{\pi}\sqrt{1 + \cos^2\theta(\sin^2\psi - 1)} \tag{57}$$

This gives us the following equation for k_x:

$$k_x = \frac{1}{pi}\int_{\theta=0}^{\pi/2}\int_{\psi=0}^{2\pi}\frac{\sqrt{1 + \cos^2\theta(\sin^2\psi - 1)}}{s}\phi_\theta\phi_\psi d\theta d\psi \tag{58}$$

The distribution of θ and ψ are assumed to be uniform.

The elemental deposition velocity for a broad leaf is gives as:

$$u_{IN}^D = |U|\sqrt{d_p/(4l)}\,\sin\,\theta \tag{59}$$

Again, the varying parameters are the orientation angles and the leaf size. This leads to the following equation for the averaged deposition velocity of broad leaves:

$$U_{IN}^D = \int_{\theta=0}^{\pi/2}\sin\,\theta\phi_\theta d\theta\int_l\frac{l^2}{\overline{l^2}}\int_{\psi=0}^{\pi/2}|U|\sqrt{d_p/(4l)}\phi_\psi d\psi \tag{60}$$

For a uniform distribution of leaf widths, this reduces to:

$$U_{IN}^D = |U|\frac{3k_x}{8}\frac{d_p}{l}\Big[\frac{3}{2} + \ln\frac{8l}{d_p}\Big] \tag{61}$$

k_x is slightly different, due to the fact that for broad leaves $s_x = s/2\sin\,\theta|\cos\,\psi|$. This gives us the following expression for k_x:

$$k_x = \int_{\theta=0}^{\pi/2}\int_{\psi=0}^{2\pi}\frac{1}{2\sin\,\theta|\cos\psi|}\phi_\theta\phi_\psi d\theta d\psi \tag{62}$$

4.1.3 Inertial Impaction

Inertial impaction occurs when the inertia of the particles causes the particle not to follow the streamlines, which curve around the obstacles. This means that the particle will collide with and adhere to the obstacle. This process is displayed in figure (4). Inertial impaction depends on the Stokes number, calculated with the needle diameter, or the leaf width. The Stokes number is the ratio of the particle response time and the flow response time. If the Stokes number is high, the coupling between the particle and the fluid is not very firm, allowing it to deviate from the streamlines of the flow. The elemental deposition velocity is given as:

$$U_{IM}^D = \frac{s_x}{s}E_{IM} \tag{63}$$

where E_{IM} is the inertial impaction efficiency. It is calculated using the following empirical expression:

$$E_{IM} = \Big(\frac{St}{\beta + St}\Big)^2 \tag{64}$$

where β is the impaction constant. We see that impaction efficiency goes towards 1 when the Stokes number becomes very large. The varying parameters are the obstacle surface, the orientation angles, and the needle diameter or the leaf width. Using the previous argumentation, we get the following expression for the averaged deposition velocity for needle-like collectors:

$$U_{IM}^{D} = |U|k_x \int_{D(d_n)} \frac{x}{\bar{d}_n} E_{IM}(x)\phi_{d_n}(x)dx \tag{65}$$

and the following expression for broad leaf collectors:

$$U_{IM}^{D} = |U|k_x \int_{D(l)} \frac{l^2}{\bar{l}^2} E_{IM}(l)\phi_{l}(x)dx \tag{66}$$

For uniform distributions of the needle diameter and the leaf size, we get the following expression for the averaged deposition velocity of needle-like collectors and broad leaves respectively:

$$U_{IM}^{D} = |U|k_x \frac{St_m^2}{2\beta^2}\Big[\frac{1}{1+2\beta/St_m} + \ln\Big(1+\frac{2\beta}{St_m}\Big)\Big] \tag{67}$$

$$U_{IM}^{D} = |U|\frac{3k_x}{4}\frac{St_m^2}{\beta^2}\Big[2\frac{1+St_m^2/\beta}{2+St_m^2/\beta} - \frac{St_m}{\beta}\ln\Big(1+2\frac{\beta}{St_m}\Big)\Big] \tag{68}$$

where St_m is the Stokes number calculated with the mean width of the leaves or the mean needle diameter.The particle relaxation time,τ_p that is used to calculate St_m is defined as:

$$\tau_p = \frac{d_p^2 \rho_p C_c}{18\mu} \tag{69}$$

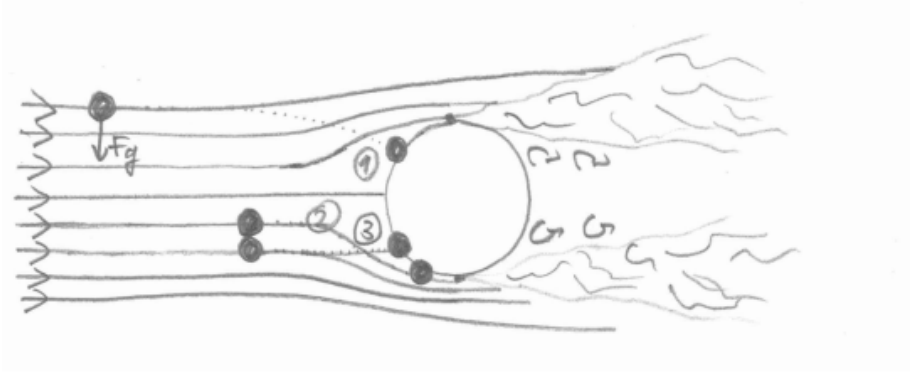

Figure 4: Dry deposition of particles onto a solid collector by Sedimentation (1), Interception (2), and Inertial Impaction (3).

4.1.4 Turbulent Impaction

Turbulent impactions occurs when the inertia of the particles is large enough to overcome the effect of the present turbulent eddies, causing it to collide with the obstacles. It has been shown that inertial particles tend to move in the direction of decreasing turbulence [Petroff et al., 2009]. At the collector surface, we have a very small laminar boundary layer. So, there is a negative 'turbulence gradient' when approaching the surface, which should causes the particles to move

in said direction. It is assumed that this phenomena mainly depends on the local turbulence and the inertia of the particles, which means that the turbulent impaction is equal for both needle-like collectors and broad leaves [Petroff et al., 2008], [Petroff et al., 2009]. This also means that the elemental deposition velocity is equal to the elemental deposition velocity. The following equation is used to calculate its contribution:

$$U_{TI}^{D} = \begin{cases} u_* K_{TI1} \tau_p^{+2} & \text{if } \tau_p^+ < 20 \\ u_* K_{TI2} & \text{if } \tau_p^+ \geq 20 \end{cases} \tag{70}$$

where u_*n is the frictional velocity, $\tau_p^+ = \frac{\tau_p u_*^2}{\nu_a}$ is the dimensionless relaxation time, K_{TI1} and K_{TI2} are model constants.

4.1.5 Sedimentation

Sedimentation is simply particle settling due to gravity. This process is displayed in figure (4). It is assumed to be independent of the turbulence and can be calculated using the settling velocity and the projected surface area of the collector in the $\hat{z}$-direction. The elemental deposition velocity is the same for both collectors:

$$u_{sedi}^{D} = V_{settling}(d_p)\frac{s_z}{s} \tag{71}$$

where $V_{settling}$ is the settling velocity. $s_z = \frac{s}{\pi}\cos\theta$ for needle-like collectors and $s_z = \frac{s}{2\cos\theta}$. The varying parameters are d_n and θ. This gives us the following expression for the averaged deposition velocity for both needle-like collectors and broad leaves:

$$U_{d,S} = V_{settling}(d_p)k_z \tag{72}$$

The following equations are used to determine k_z for needle-like collectors and broad leaves respectively:

$$k_z = \frac{1}{\pi}\int_{\theta=0}^{\pi/2} \cos\theta \phi_\theta d\theta \tag{73}$$

$$k_z = \int_{\theta=0}^{\pi/2} \frac{1}{2\cos\theta}\phi_\theta d\theta \tag{74}$$

The values of the various constants that are mentioned, for both collectors, assuming a uniform distribution of lead width and needle diameter, in the following table:

Table 1: Model constants for both collector types with a uniform distribution of leaf widths, assuming a laminar boundary layer around the individual leaves

Collector Types	C_b	I_B	n_B	k_x	k_z	β	K_{TI1}	K_{TI2}
Needle like	0.467	0.94	1/2	0.27	$2/\pi^2$	0.6	3.5×10^-4	0.18
Broad	0.664	0.85	1/2	$2/\pi^2$	$1/\pi$	0.47	3.5×10^-4	0.18

The behaviour of the dry deposition model for needle-like and broad leaf collectors is summarized in the following figures. The dry deposition velocity has been calculated using $U = 1\frac{m}{s}$, $u_* = 0.1\frac{m}{s}$, $l = 0.01$ m, $d_n = 0.005$ m and an obstacle height of 2.2 m.

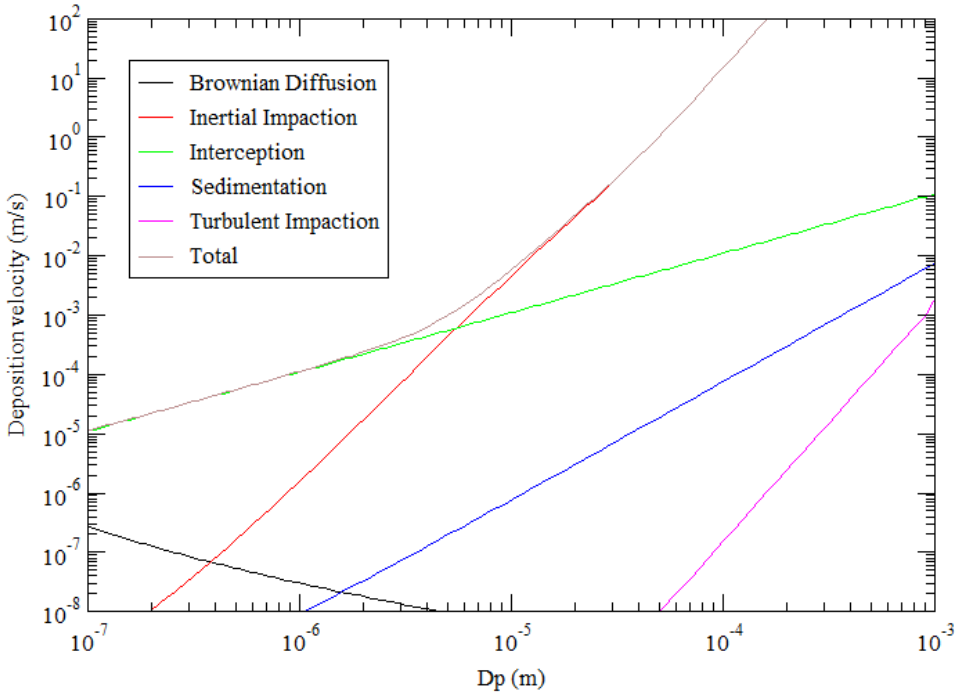

(a) The dry deposition velocity for needle-like collectors with $U = 1\frac{m}{s}$, $u_* = 0.1\frac{m}{s}$, $l = 0.01$ m, $d_n = 0.005$ m and an obstacle height of 2.2 m

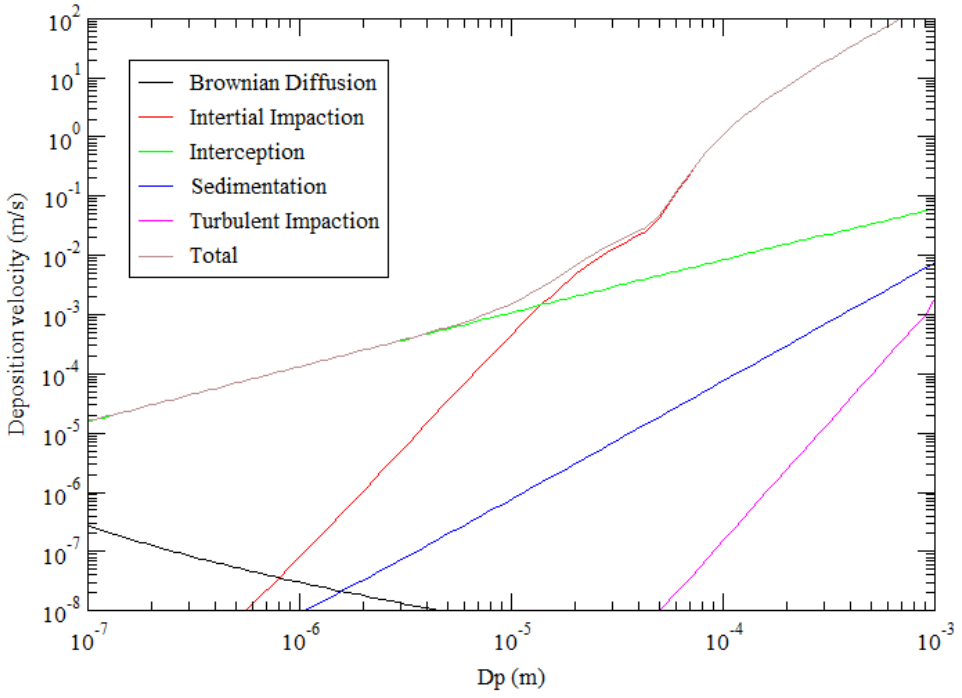

(b) The dry deposition velocity for broad leaf collectors collectors with $U = 1\frac{m}{s}$, $u_* = 0.1\frac{m}{s}$, $l = 0.01$ m, $d_n = 0.005$ m and an obstacle height of 2.2 m

Figure 5

5 Numerical Method

In order to solve the time-averaged transport equations of the momentum, concentration, and temperature numerically some steps have to taken; First, the domain has to be discretized. It has to be divided into a number of sub-domains, also called control volumes or cells. Secondly, the original transport equations have to be turned into discrete algebraic equations. Finally, this system of linear algebraic equations needs to be solved.
The process of solving the complete system of sub-domains, consists of solving each individual sub-domain. The solution of an individual cell depends on its boundary condition. Generally, sub-domains are enclosed by other sub-domains. This means that the sub-domains are linked by their boundary conditions. For sub-domains at the boundary of the geometry, the geometrical boundary conditions are applied. The numerical methods that are used to tackle these steps can have a large effect on the outcome of the simulation. In the following section, the used numerical methods are discussed.

5.1 Discretization and difference schemes

In order to discretize the transport equations, the Finite Volume Method (FVM) is used. The main idea of the FVM is that the transport equations are integrated over the individual sub-domains. It is assumed that the state of the cell is defined by a single value. This is the value of the scalar described by the transport equations, evaluated at the center of the sub-domain. Terms that contain a divergence term are converted to a surface integral using Gauss's Theorem. Therefore, the fluxes of each sub-domain are conserved.
In this research, every sub-domain is a rectangular cuboid. Every sub-domain has 6 neighbouring volumes, denoted with W (West), E (East), N (North), S (South), T (Top), and B (Bottom). The half-way points between the sub-domains are denoted using lowercase letters w,e,n,s,t,b.

We start with the general differential equations describing the transport of a scalar ϕ:

$$\frac{\partial}{\partial t}(\rho\Phi) + \frac{\partial}{\partial x_j}\Big(\rho U_j \Phi\Big) = \frac{\partial}{\partial x_j}\Big(\Gamma \frac{\partial \Phi}{\partial x_j}\Big) + S \tag{75}$$

We will discretize this equation in 1D using the FVM to illustrate the how the different terms are handled. The following equation is obtained after volume integration in 1D:

$$\int_w^e \frac{\partial}{\partial t}(\rho\Phi)dV + \int_w^e \frac{\partial}{\partial x}\Big(\rho U\Phi\Big) = \int_w^e \frac{\partial}{\partial x}\Big(\Gamma\frac{\partial\Phi}{\partial x}\Big) + \int_w^e S \tag{76}$$

$$\frac{\partial}{\partial t}(\rho\Phi)\Delta x S + \Big(\rho U\Phi\Big)_e - \Big(\rho U\Phi\Big)_w = \Big(\Gamma\frac{\partial\Phi}{\partial x}\Big)_e - \Big(\Gamma\frac{\partial\Phi}{\partial x}\Big)_w + \overline{S}\Delta x \tag{77}$$

where Δx is the size of the domain in $\hat{x}$ direction and $\overline{S}$ is the average value of the source term in the domain, evaluated at the center. The diffusion terms are evaluated using linear interpolation:

$$\Big(\Gamma\frac{\partial\Phi}{\partial x}\Big)_e = \Gamma\frac{\Phi_E - \Phi_P}{\delta x_e} \tag{78}$$

$$\Big(\Gamma\frac{\partial\Phi}{\partial x}\Big)_w = \Gamma\frac{\Phi_P - \Phi_W}{\delta x_w} \tag{79}$$

where δx_e is the distance between P and E, and δx_w is the distance between P and W. The convection terms are slightly more complicated. The simplest method to represent these terms is using the *Central Differencing Scheme*. It uses linear interpolation to determine the value of Φ at the half-way distance between the sub-domains:

$$\Phi_e = \frac{1}{C}\Big(\Phi_E + \Phi_P) \tag{80}$$

$$\Phi_w = \frac{1}{C}\Big(\Phi_W + \Phi_P) \tag{81}$$

Where C is a constant that depends on the size difference between the sub-domain and its neighbours. For a uniform mesh $C = \frac{1}{2}$. However, the central differencing scheme can produce unrealistic results if convection dominates over diffusion. These results can be unbounded, which makes the overall unstable.

To combat this, the *Upwind Differencing Scheme* can be used. It project the upwind central values onto the cell faces of the sub-domains. So, it there is net flow in the $\hat{x}$ direction ($U > 0$), then $\Phi_e = \Phi_P$ and $\Phi_w = \Phi_W$. If the flow is reversed, $\Phi_e = \Phi_E$ and $\Phi_w = \Phi_P$. To improve its numerical accuracy, a higher order upwind differencing scheme can be used. In this research, the *Quadratic Upstream Interpolation for Convective Kinematics* (QUICK) or *Quadratic Upwind Differencing Scheme* (QUDS) is used. It determines the cell face values around the central points using three consecutive grid points. it also take the flow direction into consideration. For a net flow in the $\hat{x}$ direction we have the following expressions:

$$\Phi_w = \frac{6}{8}\Phi_W + \frac{3}{8}\Phi_P - \frac{1}{8}\Phi_{WW} \tag{82}$$

$$\Phi_e = \frac{6}{8}\Phi_P + \frac{3}{8}\Phi_E - \frac{1}{8}\Phi_W \tag{83}$$

if the flow is reversed, we get the following expression:

$$\Phi_w = \frac{6}{8}\Phi_P + \frac{3}{8}\Phi_W - \frac{1}{8}\Phi_E \tag{84}$$

$$\Phi_e = \frac{6}{8}\Phi_E + \frac{3}{8}\Phi_P - \frac{1}{8}\Phi_{EE} \tag{85}$$

We also use the *Linear Upwind Difference Scheme* (LUDS), that use 2 consecutive grid points to determine the cell face values using linear interpolation, taking the flow direction into account. For a net flow in the $\hat{x}$ direction we have the following expressions:

$$\Phi_w = \frac{3}{2}\Phi_W - \frac{1}{2}\Phi_{WW} \tag{86}$$

$$\Phi_e = \frac{3}{2}\Phi_P - \frac{1}{2}\Phi_W \tag{87}$$

if the flow is reversed, we get the following expression:

$$\Phi_w = \frac{3}{2}\Phi_P - \frac{1}{2}\Phi_E \tag{88}$$

$$\Phi_e = \frac{3}{2}\Phi_E - \frac{1}{2}\Phi_{EE} \tag{89}$$

In order to solve the velocity field, the mentioned method has to be adjusted. This is due to the appearance of the discretized pressure term, as seen in section 2.1. The discretized pressure

has the following form:

$$P_w - P_e = \frac{P_W + P_P}{C_1} - \frac{P_P + P_E}{C_2} \tag{90}$$

If the mesh is uniform, $C_1 = C_2 = 2$, which reduces the discretized, volume integrated pressure term to:

$$P_w - P_e = \frac{P_W - P_E}{2} \tag{91}$$

This implies that the pressure difference that is observed by the Navier-Stokes equation is twice as coarse. This means that a non-realistic pressure distribution would be possible. This also holds for the convectivion of momentum terms. This is solved by using a second staggered grid, such that the pressure and the convection terms are defined at the cell faces. The SIMPLE algorithm is used to calculate the complete coupling between the velocity and the pressure field.

5.2 Scaling

The model was implemented to deal with environmental flows. This means that the domains are generally very large, in the order of 10^3 meters. The avoid having to deal with very large numbers, scaling is applied. The scaling factor is depends on the height of the domain. The scaling factor is chosen is such a way that the scaled height is exactly 1. It is applied to all geometric parameters, including the roughness parameter and the leaf area density. To make sure that the behaviour of the scaled model is still physical, Reynolds similarity and Kolmogorov similarity are applied. Reynolds similarity is simply obtained by multiplying the viscosity by the scaling factor:

$$\nu' = \nu \times \text{scaling} \tag{92}$$

Using this result, the scaling of the dissipation of TKE can be obtained. We start from Kolmogorov similarity:

$$\eta' = \text{scaling} \times \left(\frac{\nu^3}{\epsilon}\right)^{1/4} = \left(\frac{\nu'^3}{\epsilon'}\right)^{1/4} = \left(\frac{\text{scaling}^3\nu^3}{\epsilon'}\right)^{1/4} \tag{93}$$

this reduces to:

$$\epsilon' = \frac{\epsilon}{\text{scaling}} \tag{94}$$

5.3 Boundary Conditions

Boundary conditions are needed to solve the listed PDE's. They can be viewed as source terms, and have a large effect on the eventual solution of the systems of equations. Therefore, it is very important that the correct boundary conditions are used. Every domain that is used in this work is a rectangular cuboid. So, at least 6 boundary conditions have to be specified. The east and west boundaries are modelled as inlet and outlet, respectively. The inlet boundary condition is specified using *inlet profiles*. They specify the value of the important variables at every point of the *z-y* plane at the start of the domain. A zero-gradient condition is used at the outlet. The North, South and top faces of the rectangle are modelled as symmetry faces. The velocity is assumed to be parallel to the boundary plane. It is important that the domain is chosen in such a way that these conditions will not affect the solution. The bottom face is modelled as a wall. The behaviour of the flow changes due to wall, so appropriate wall functions are needed. These are discussed in the next paragraph.

5.3.1 Wall functions

Wall functions are used to describe any turbulent flow in the vicinity of a wall. We consider three different regions; the viscous sublayer, the logarithmic layer and the overlap region. The viscous sublayer is closed to wall, where turbulence effects are no longer dominant. Consequently, the velocity gradient depends on the viscosity. The logarithmic layer is assumed to be fully turbulent, with no viscous effects whatsoever. The overlap region describes the transition from a viscous to a turbulent regime.

The gradient in the viscous sublayer is very large. A very fine grid is needed to model this layer correctly. In our model, the first grid point is defined to be inside the logarithmic layer. The logarithmic wall function is derived in the following paragraph.

The logarithmic wall function is derived using a simple dimensional argument. The velocity gradient does not depend on the viscosity, so it has to be a function of the remaining characteristics of the flow:

$$\frac{dU}{dy} = f(\tau_t, \rho, y) \tag{95}$$

or in dimensional terms:

$$\left[\frac{1}{s}\right] = \left[\frac{kg}{ms^2}\right]^a \cdot \left[\frac{kg}{m^3}\right]^b \cdot \left[m\right]^c \tag{96}$$

This reduces to the following system of equations:

$$0 = a + b \tag{97}$$

$$0 = -a - 3b + c \tag{98}$$

$$1 = 2a \tag{99}$$

Consequently, we obtain the following equation for the gradient:

$$\frac{dU}{dy} = \frac{C_1}{y}\sqrt{\frac{\tau_t}{\rho}} \tag{100}$$

After integration this yields:

$$U = C_1\sqrt{\frac{\tau_t}{\rho}}\ln(y) + C_2 \tag{101}$$

$\sqrt{\frac{\tau_t}{\rho}}$ is used to non dimensionalize U and defines the friction velocity. Rearranging the logarithmic part yield the following equation:

$$\frac{U}{u_*} = C_1\ln(C_3 y) + C_4 \tag{102}$$

$C_3 = u_*/\nu$ is chosen such that a non-dimensional wall distance is obtained in the logarithm. The generalized logarithmic wall function is obtained when taking $C_1 = \frac{1}{\kappa}$ and $C_4 \approx 5.0$:

$$\frac{U}{u_*} = \frac{1}{\kappa}\ln(\frac{u_* y}{\nu}) + C_4 \tag{103}$$

This can also be written as:

$$U^+ = \frac{1}{\kappa}\ln(E\frac{u_* y}{\nu}) \tag{104}$$

where $E = 8.432$. It is important to note that the transition from the viscous sublayer to the logarithmic layer occurs at around $y^+ \approx 11$. So, the mesh should be defined in such a way that

the first grid point is far enough away from the wall to be in the logarithmic layer.

The numerical implementation is straightforward. The friction velocity is modelled as $u_* = C_\mu^{1/4} k^{1/2}$. Then the following equation is obtained for the wall shear stress:

$$\tau_t = \tau_w = \rho C_\mu^{1/4} k_p^{1/2} \frac{U}{\ln\Big(Ey\Big)} \tag{105}$$

This equation is used to calculate the velocity in the grid point closest to the wall.

However, these equations are only valid for smooth walls. Because we will be dealing with vegetation flow, it is likely that wall roughness will play a role. Wall roughness is generally described using the height of the irregularities, the roughness parameter e. The effect of the roughness on the logarithmic wall function depends on $\frac{eu_*}{\nu}$, the Reynolds number calculated with the roughness height. The new logarithmic wall function is obtained from *Introduction to Theory and Applications of Turbulent Flow* by Nieuwstadt et al. [2016] and has the following form:

$$\frac{U}{u_*} = \frac{1}{\kappa} \ln\Big(\frac{y}{e}\Big) + B \tag{106}$$

where B is defined by the following function:

$$B = \begin{cases} 2.5 \ln\Big(\frac{eu_*}{\nu}\Big) + 5 & \text{if } \frac{eu_*}{\nu} \ll 1 \\ 8.5 & \text{if } \frac{eu_*}{\nu} \gg 1 \end{cases} \tag{107}$$

For a rough wall $\frac{eu_*}{\nu} \gg 1$ always holds. This gives us the following equation for the logarithmic wall function:

$$\frac{U}{u_*} = \frac{1}{\kappa} \ln\Big(\frac{y}{e}\Big) + 8.3 \tag{108}$$

This can be rewritten as:

$$\frac{U}{u_*} = \frac{1}{\kappa} \ln\Big(E_R \frac{y}{e}\Big) \tag{109}$$

where $E_R = e^{8.3\kappa}$. This means that our expression for the wall shear stress is now:

$$\tau_t = \tau_w = \rho C_\mu^{1/4} k_p^{1/2} \frac{U}{\ln\Big(\frac{E_R}{e} y\Big)} \tag{110}$$

It is important to note that z_0, the environmental roughness height is not the same as the roughness parameter. They are related by the following equation:

$$z_0 = \frac{e}{E_R} \tag{111}$$

5.4 Grid and Domain Definition

As mentioned before, the domains that are used in this work are rectangular cuboids. Their respective sizes is determined by four different parameters; the size of the obstacles and the space before and after the obstacles in $\hat{x}$, $\hat{y}$ and $\hat{z}$ direction. In this work, 2 types of obstacles are used:

- Blocks
- Trees

Trees are simply sections of the domain where the altered transport equations are used. Blocks are sections in the domain where no flow is present. This means that wall functions are applied at every face of the block. Consequently, the roughness parameter of the blocks has to be provided when the simulation is performed.

The distance after the obstacles has to be very large, to satisfy the symmetry condition of the North, South and top face and the no-gradient boundary condition of the East face. This means that the dimensions of the domain are generally at least 10^1 larger than the obstacles. However, most of the important physical phenomena occur close to the obstacles, and are characterized by large gradients. A fine mesh is needed to accurately model these phenomena. Using a uniform fine mesh would require to much computational resources, so a non-uniform mesh is used. The cell size is large at the symmetry faces, and is gradually decreased as the mesh approaches the obstacles and the bottom face of the domain.

The refinement is governed by three parameters, the maximum cell size, the cell size at the obstacles (the minimum cell size), and the expansion factor.

6 Dispersion Case Study: Collection efficiency of hedgerows for ambient aerosols

In order to determine the effectiveness of the proposed model to predict the change of concentration due to vegetation, it is compared with empirical measurements. The filtering capacity of vegetation depends heavily on the particle diameter. Hence, an experiment was selected where this was on of the tested parameters. This is the experiment included in *Modelling of size-dependent collection efficiency of hedgerows for ambient aerosols* by Tiwary et al. [2006]. The authors measured the stream wise velocity and the concentration of polystyrene particles before and after hawthorn, holly, and yew hedges in an open field. A sketch of the experimental setup is displayed in figure (6).

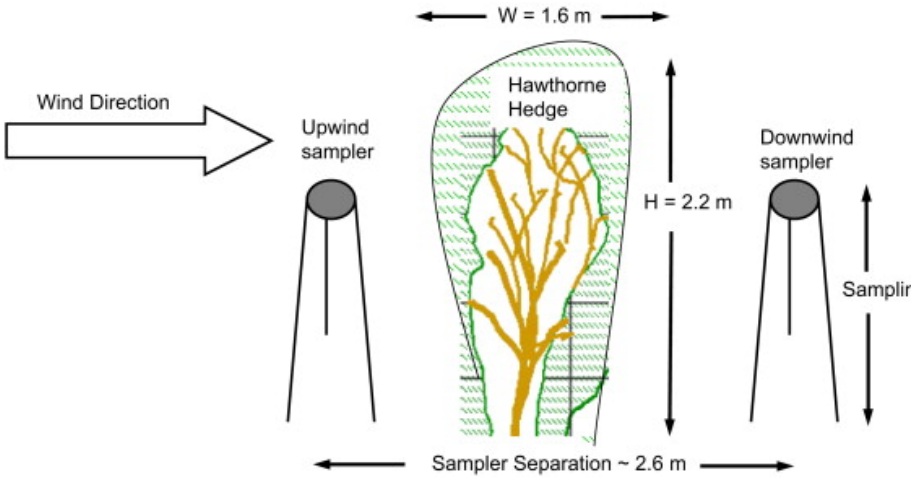

Figure 6: The experimental setup that was used by Tiwary et al. [2006]. Obtained from Tiwary et al. [2008].

Their results were presented in the form of the collection efficiency, defined as:

$$C_E = \frac{C_{in} - C_{out}}{C_{in}} \tag{112}$$

where C_{in} and C_{out} are the concentration levels at $z = 0.75H$ and $x = 0.1$ up- and downwind. Field validation of the overall C_E was only obtained for a hawthorn hedge. The measurements were performed with an average wind speed of 2.3 $\frac{m}{s}$ for particle diameters of 0.875, 1.5, 2.75, 4.25, 6.25, 8.75, 12.5 and 15 μm.

A model generated leaf area density profile was provided of the hedge. This was dicretized into 11 separate vegetation obstacles to model the vegetation in this work. The profiles are displayed in figures (7a and (7b).

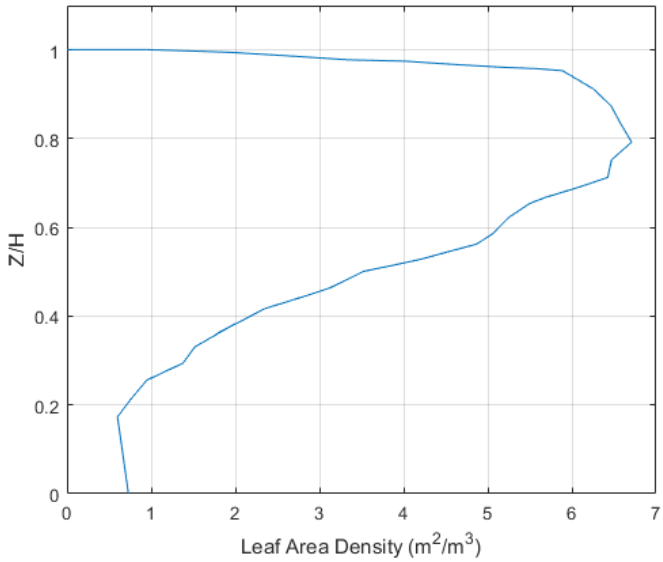

(a) Reported LAD profile by Tiwary et al. [2006]

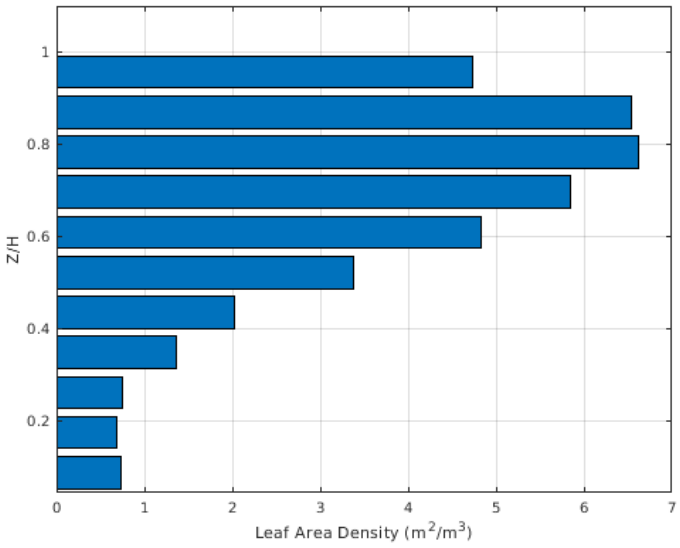

(b) Discretized LAD profile that was used in this research

Figure 7

The size of the leaves ranged from 11-30 mm [Tiwary et al., 2006]. C_D varies per species, and was determined using the measured stream wise velocity profile behind the hedge. The measurements were displayed as a function of k_r, the layer-wise resistance coefficient. It was calculated using the following formula:

$$\frac{U_{before}}{U_{after}} = \sqrt{\frac{\Gamma_{bl}}{k_r + (\Gamma_{bl} k_1)}} \tag{113}$$

where U_{before} and U_{after} are the velocities measured upwind and downwind of the hedge at $x/H = \pm 0.1$, $\Gamma_{bl} = 1.07$ was the bulk drag coefficient and $k_1 = 1.28$ was the roughness parameter [Tiwary et al., 2006].

The measurements obtained by Tiwary et al. [2006] have previously been used to validate a RANS, $k - \epsilon$ model solver that involves a similar deposition velocity model, described in *RANS solver for microscale pollution dispersion problems in areas with vegetation: Development and validation* by Šíp and Beneš [2016]. The approach of our research is largely based on the aforementioned work.

6.1 Inlet Profiles

In order to obtain the correct inlet profiles for the velocity, TKE and the dissipation of TKE, empty channel simulations were performed. Tiwary et al. [2006] provided the roughness height and the air speed at a reference height: $z_0/H = 0.0086$ and $U_{ref} = 2.3$ m/s. The process of performing the empty channel simulations was straightforward; a plug flow was used as the inlet profile, and the boundary layer developed due to the surface roughness. In the developed boundary layer, the velocity was measured at the reference height. The magnitude of the plug flow was adjusted accordingly and the pre-simulation was repeated until the correct logarithmic inlet profile was obtained. The corresponding friction velocity was obtained from the simulation and was found to be $u_* = 0.1903$ m/s. The inlet profiles are displayed in the following figure.

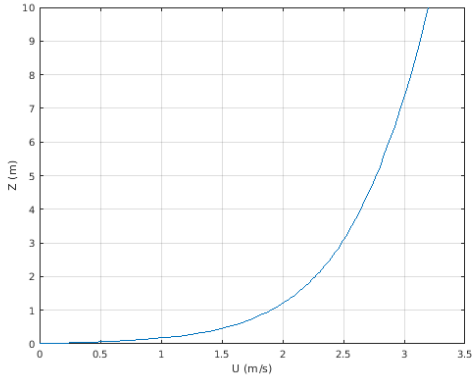

(a) The velocity inlet profile

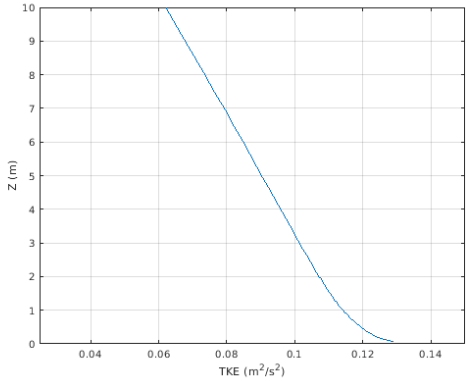

(b) The TKE inlet profile

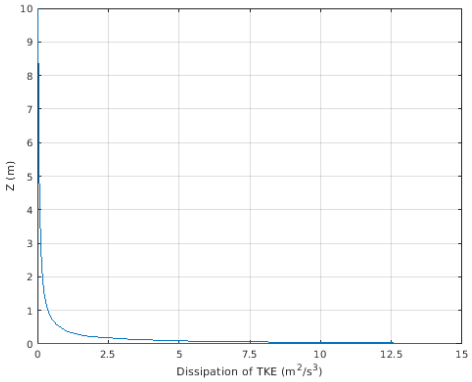

(c) Inlet profile of the dissipation of TKE

Figure 8: Inlet profiles of U, TKE (k) and the dissipation of TKE (ϵ)

For the simulations involving concentration effects, a uniform inlet profile of the concentration was used.

6.2 Simulation domain

The hedge obstacle was placed $x = 19W = 41.8$ m and $z = 0$ m. It was uniform in the $\hat{y}$ direction and stretched over the total length of the domain in $\hat{y}$ direction. As a result of this and the symmetry conditions at the North and South faces of the domain, the code acted as a 2D simulation. The hedge was modelled as 10 vegetation obstacles, stacked on top of each other. A sketch of the domain in $\hat{x}$ and $\hat{z}$ direction was obtained from [Šíp and Beneš, 2016] and is displayed in the following figure:

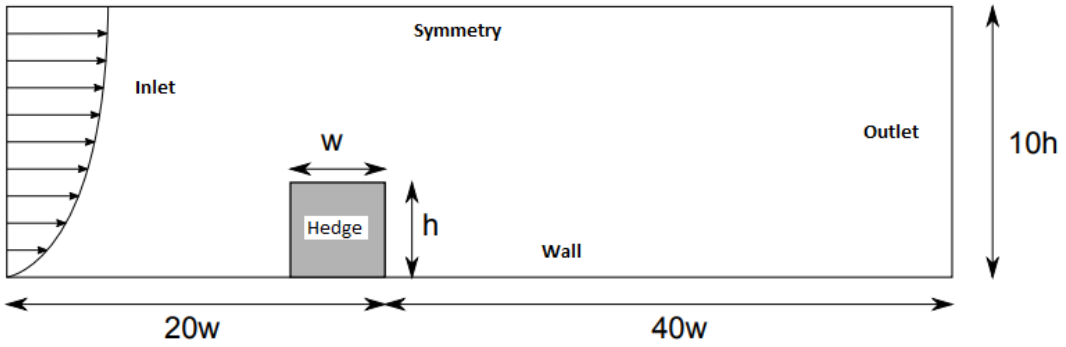

Figure 9: Sketch of the x-z plane of the simulation domain (not to scale). Obtained from *RANS solver for microscale pollution dispersion problems in areas with vegetation: Development and validation* by Šíp and Beneš [2016].

The simulation domain was $132 \times 20 \times 16$ m^3. The mesh consisted of $132 \times 25 \times 85$ control volumes. The maximum cell size was $2 \times 4 \times 2$ m^3. The cell size at the obstacles was $0.05 \times 0.5 \times 0.05$ m^3. The mesh is displayed in the following figure:

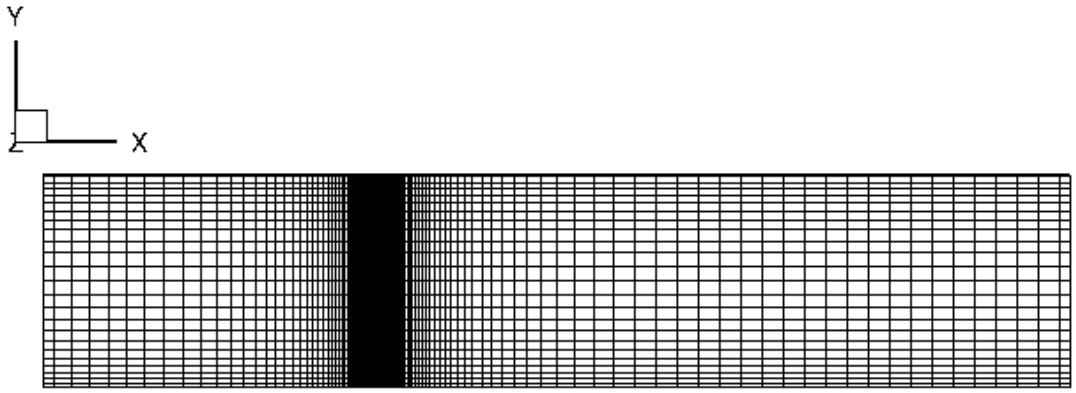

(a) Mesh of the x-y plane

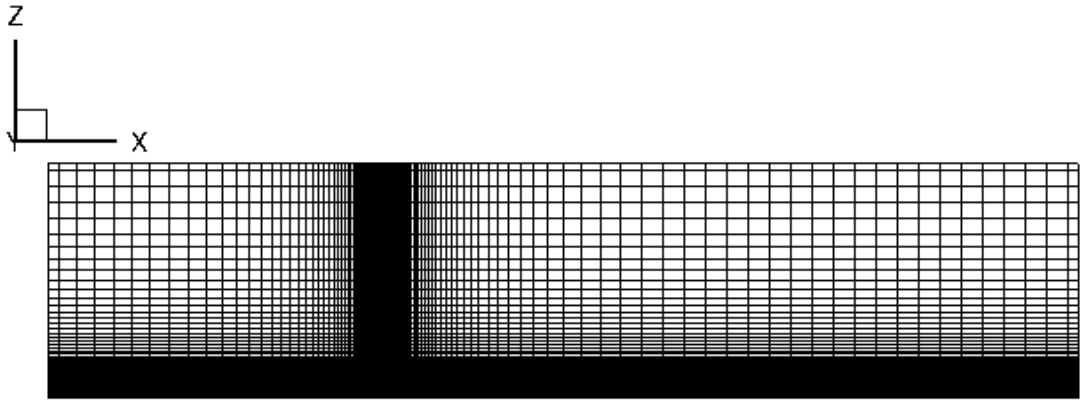

(b) Mesh of the x-z plane

Figure 10: The mesh of the x-y plane and the mesh of the x-z plane.

6.3 Results

6.3.1 Drag Coefficient

The flow through the hedge was simulated for different values of the drag coefficient. These values were $C_D = [0.15, 0.17, 0.19, 0.25, 0.30]$. The contours of the velocity and TKE, obtained for $C_D = 0.15$ and $C_D = 0.30$ are displayed in figure (11) and (12) to show the influence of C_D on the flow field.

It is clear that the magnitude of the drag coefficient has a large influence of the velocity field. The size of the boundary layer decreases significantly. The flow speeds up close to the ground, as it tries to avoid the upper layers of the hedge, where the LAD is significantly higher. Consequently, a significant decrease of velocity is observed in the upper layers of the hedge. The size of the wake increases when the value of the drag coefficient is increased.

We see that the hedge obstacle acts as a source of TKE. Apparently, the generation of large scale eddies is dominant over the short-cut of the energy cascade. Vegetation obstacles generally act as a sink of TKE if the LAD is very high, or if the obstacle is very large (like a forest) [Kenjereš and ter Kuile, 2013],[Šíp and Beneš, 2016]. This is in accordance with the results from the simulation with $C_D = 0.30$. We observe a small area at the height of the most dense part of the vegetation, where the TKE is significantly lower than its surroundings.

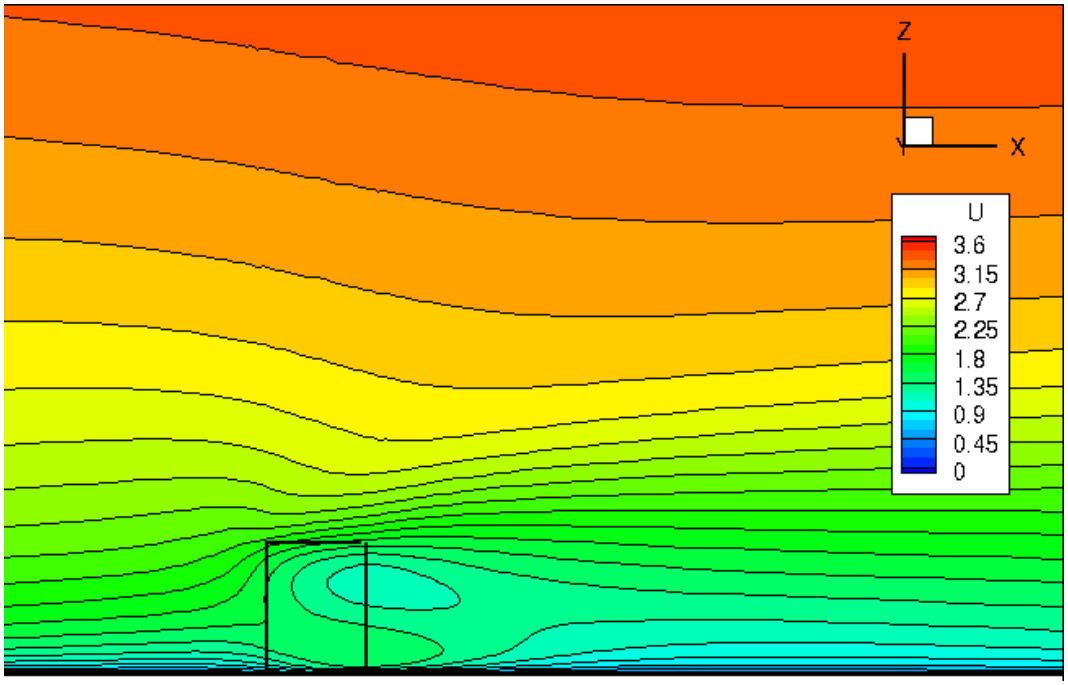

(a) $C_D = 0.15$

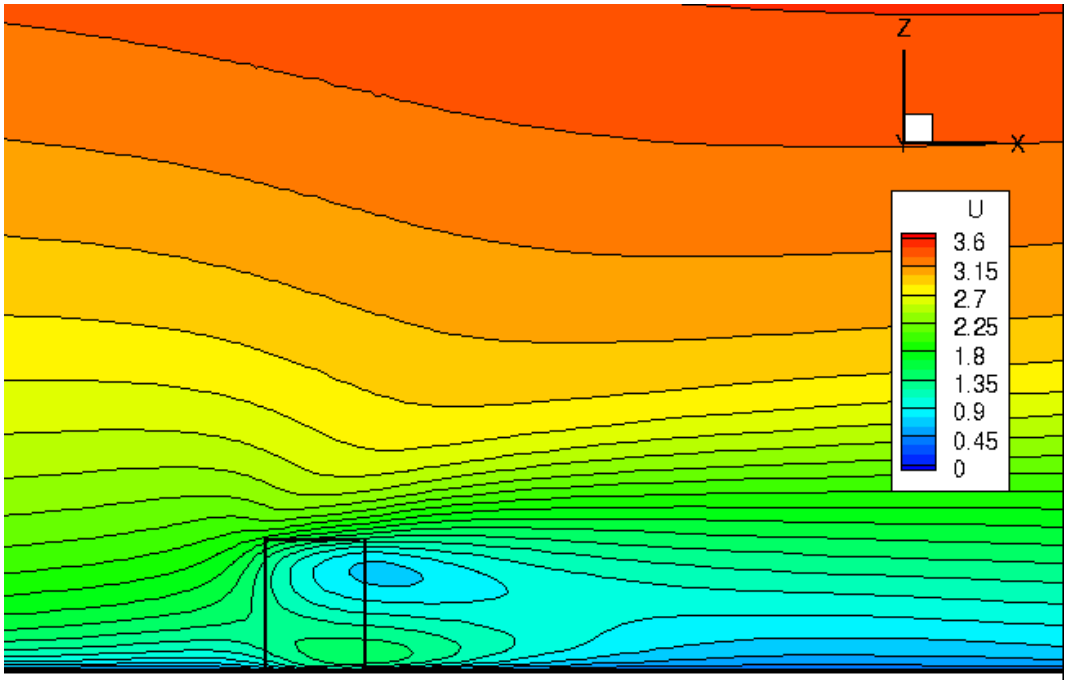

(b) $C_D = 0.30$

Figure 11: Flow field through and around the hedge obstacle for $C_D = 0.15$ and $C_D = 0.30$. The hedge obstacle is indicated by the solid lines

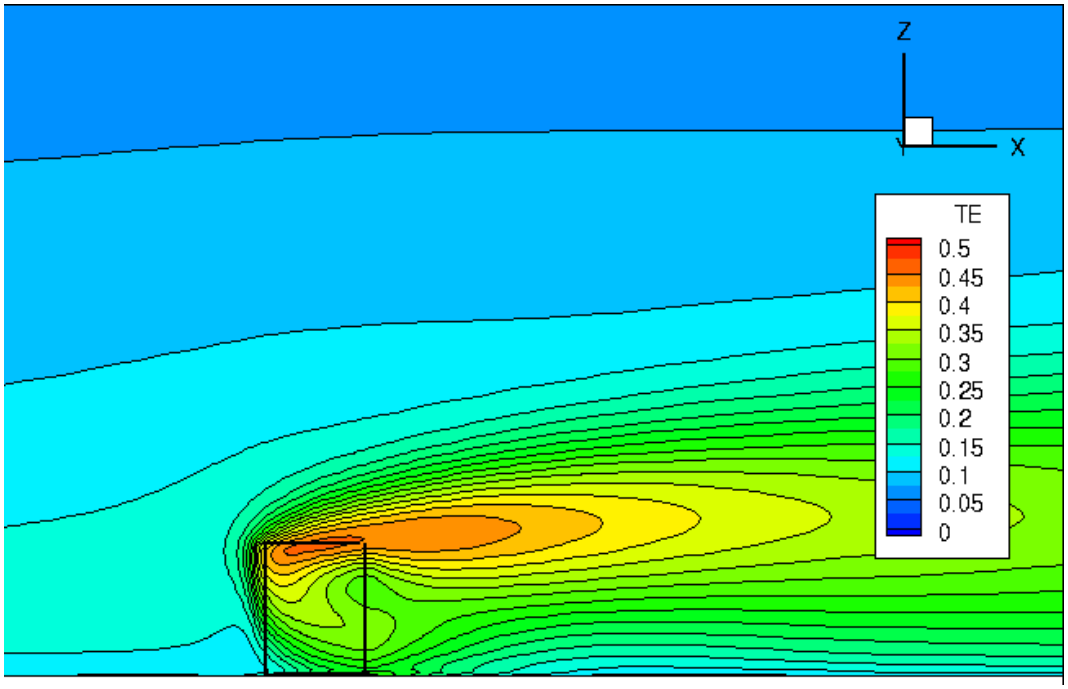

(a) $C_D = 0.15$

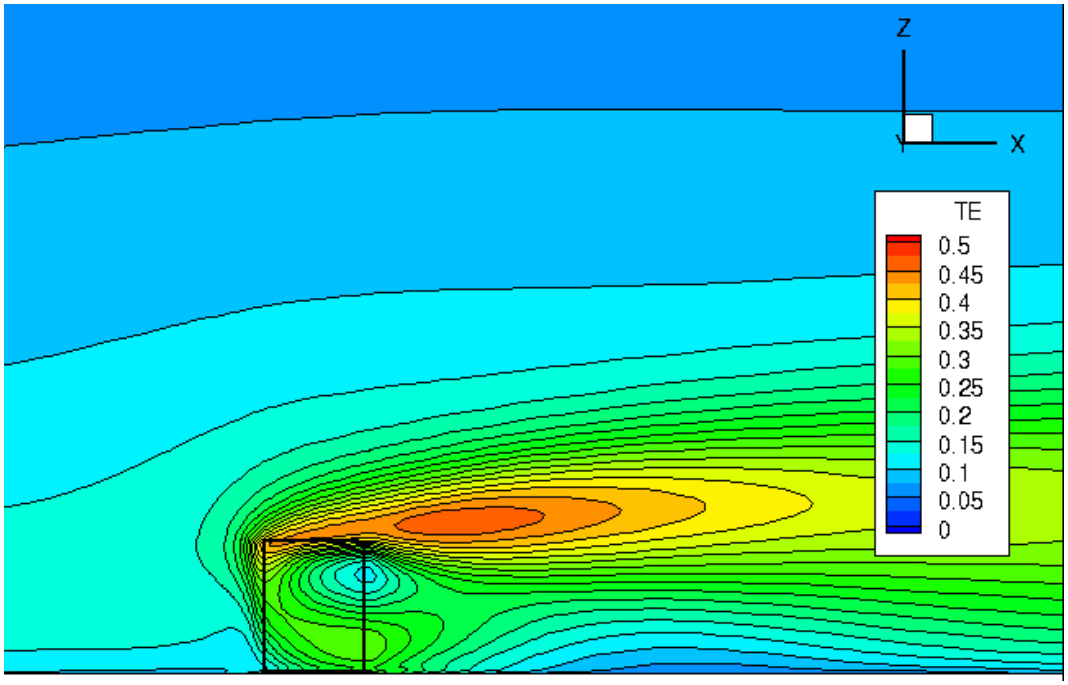

(b) $C_D = 0.30$

Figure 12: The simulated TKE field for $C_D = 0.15$ and $C_D = 0.30$. The hedge obstacle is indicated by the solid lines.

In order to determine the correct drag coefficient, the velocity profiles were extracted at $\frac{x}{10} = H$ downwind of the obstacles. These were compared with the measurements performed at $\frac{z}{H} = [0.25, 0.5, 0.75]$. The results are displayed in the following figure, along with the experimental data from Tiwary et al. [2006].

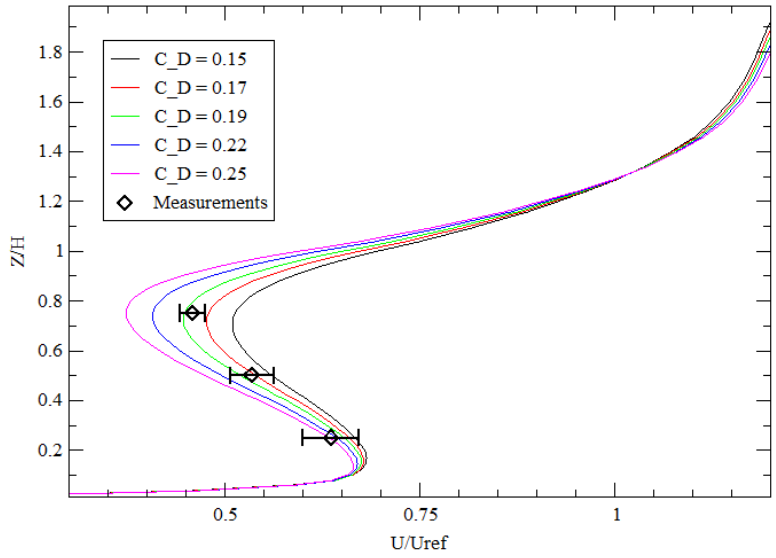

Figure 13: Velocity profiles right after the hedge obstacles. The velocity is normalized using the reference velocity, and the height is normalized using the height of the hedge. The experimental data is obtained from Tiwary et al. [2006].

We observe two important characteristics; the first inflection point occurs at approximately $\frac{z}{H} = 0.15$ and the second one at approximately $\frac{z}{H} = 0.75$. The velocity profile below the first inflection point is not affected by the drag coefficient. It is entirely governed by the wall function. The effect of the drag coefficient becomes more pronounced as the distance to the ground increases. Its effect decreases again as we move towards the upper layer of the vegetation, which features a low value of the LAD. The velocity increases again until it reaches the free stream velocity at the top of the domain.

We found the best agreement with the experimental data for $C_D = 0.19$. This value was used for the next part of the simulation, the calculation of the collection efficiency.

6.3.2 Collection Efficiency

The collection of particles in the hedge obstacles was modelled using the Petroff et al. [2008] and Petroff et al. [2009] model, described in section 4.2. We assumed that the hedge obstacle is a pure broad leaf collector. So, the deposition velocities were solely calculated using the broad leaf model. The collection efficiency was calculated for particles with the following sizes: 4.25, 6.25, 8.75, 12.5, and 15 μ m. This is done for leaf widths of 0.05, 0.01 and 0.02 m.
The concentration fields obtained with $D_P = 15\mu$ m for $l = 0.05$ m and $l = 0.02$ m are displayed

in figures (14a) and (14b) to illustrate the effect of filtering on the overall concentration field. The concentration profiles of every particle size are displayed in figure (15).

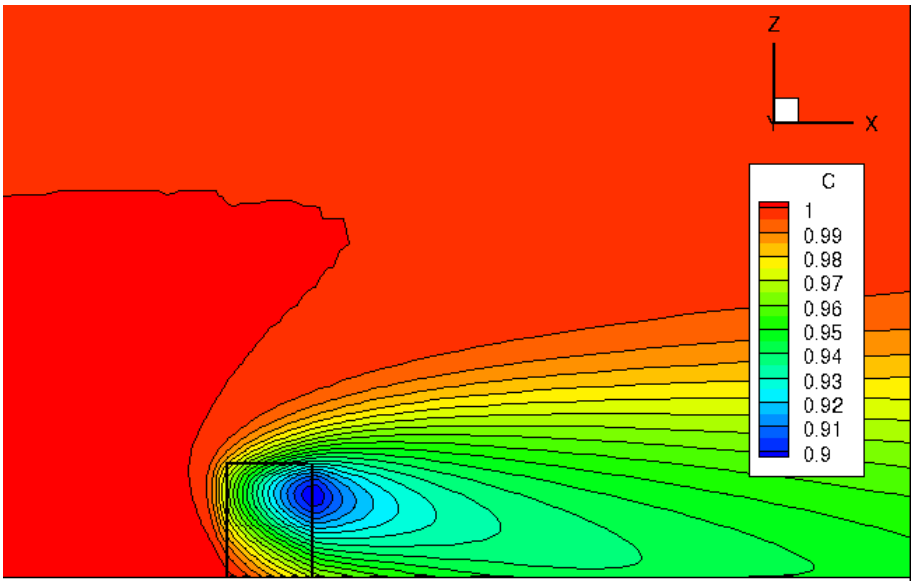

(a) $D_P = 15\mu$ m, $l = 0.005$ m.

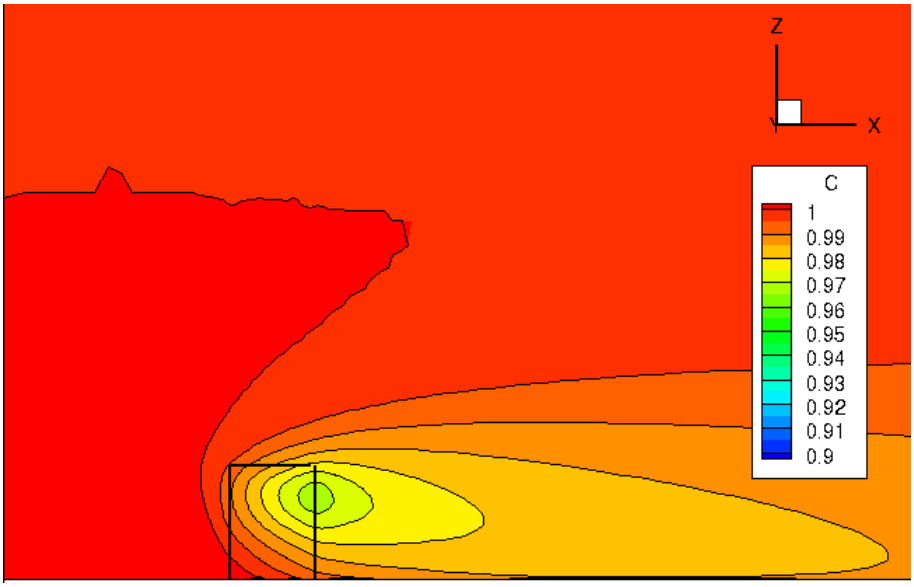

(b) $D_P = 15\mu$ m, $l = 0.02$ m

Figure 14: The simulated concentration field of $D_P = 15\mu$m for $l = 0.02$m. The hedge obstacle is indicated by the solid lines.

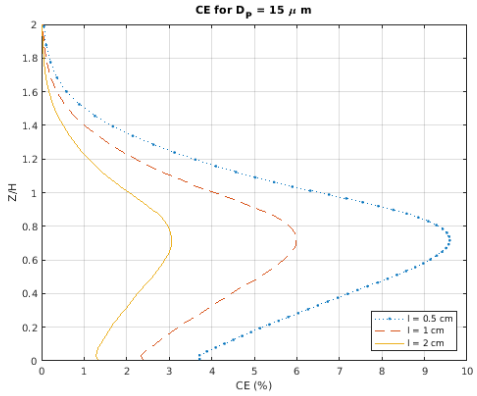

(a) $D_P = 15\mu$m

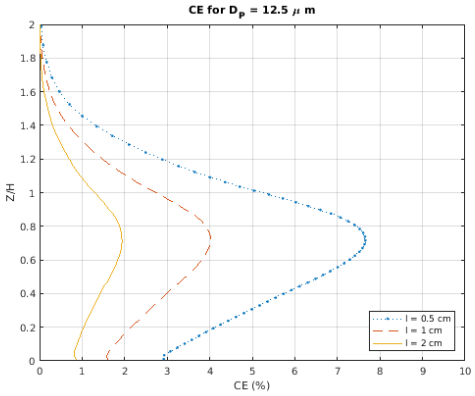

(b) $D_P = 12.5\mu$m

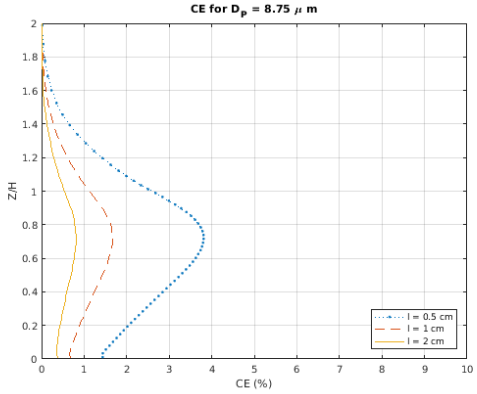

(c) $D_P = 8.75\mu$m

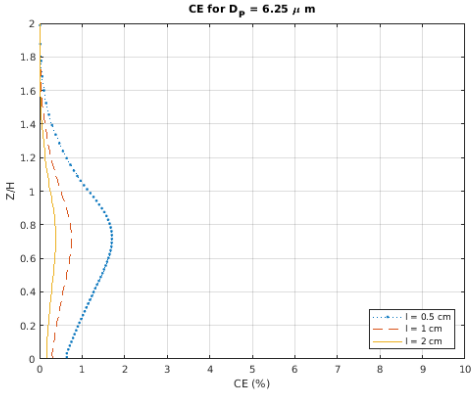

(d) $D_P = 6.25\mu$m

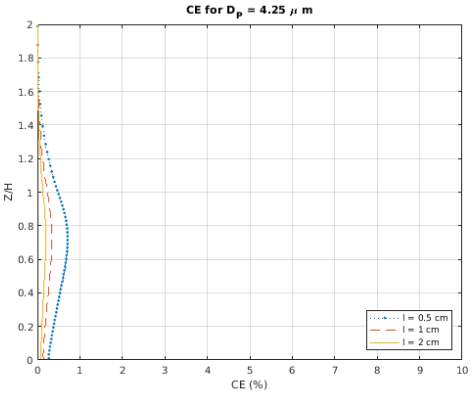

(e) $D_P = 4.25\mu$m

Figure 15: The collection efficiency profiles with $D_P = 15,\ 12.5,\ 8.75,\ 6.25,\ 4.25\ \mu$m and $l = 0.005,\ 0.01,\ 0.02$ cm.

The behaviour of the dry deposition model is straightforward and physical. The lowest concentration is observed at $\frac{Z}{H} = 0.75$. This corresponds with the height at which the LAD

is the greatest. The lowest concentration is observed at the down-wind edge of the hedge obstacle. At the top of the hedge obstacle, the concentration efficiency has decreased, but is still non-zero. The collection efficiency becomes zero at $\frac{Z}{H}$, independent of the magnitude of the dry deposition velocity. The concentration increases as we approach the wall, but is still lower than the inlet concentration. The overall shape of the concentration fields does not depend on the magnitude of the mean leaf width of the hedge obstacle, but becomes more pronounced as it decreases.
The correlation between the particle diameter and the mean leaf with the concentration can be deduced from figure (14a). It is positively correlated with the particle size, and negatively correlated with the mean width of the leaves. The results are compared with the experimental data from Tiwary et al. [2006] and are displayed in figure (16a).

The simulation results do not match the experimental data from Tiwary et al. [2006]. The measured values are significantly higher. Šíp and Beneš [2016] suggested that this is probably due the fact that the hedge is not a pure broad leaf collector. It is likely that some collection takes place due to the presence of needle-like collectors. This means that the deposition velocity has to be calculated as a mix of the broad leaf deposition velocity and the needle-like collection efficiency:

$$U_D = (1 - \phi)U_D^{broad} + \phi U_D^{needle} \tag{114}$$

where ϕ is the collection mixing parameter.

Simulations were performed using a mean leaf width of 0.021 m and a needle size of 0.005 m for $\phi = 0.10$, 0.30, 0.35, and 0.40. The results are compared with the experimental data and displayed in figure (16b).

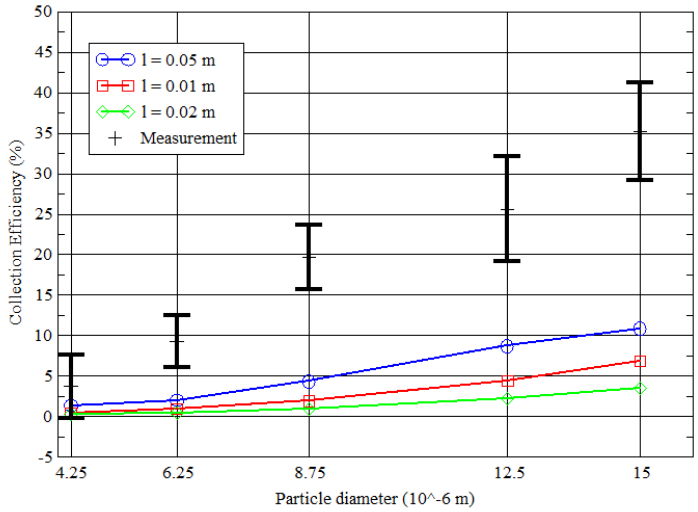

(a) The collection efficiency as a function of D_P, assuming broad leaf collection. Calculated for l = 0.005, 0.01 and 0.02 m.

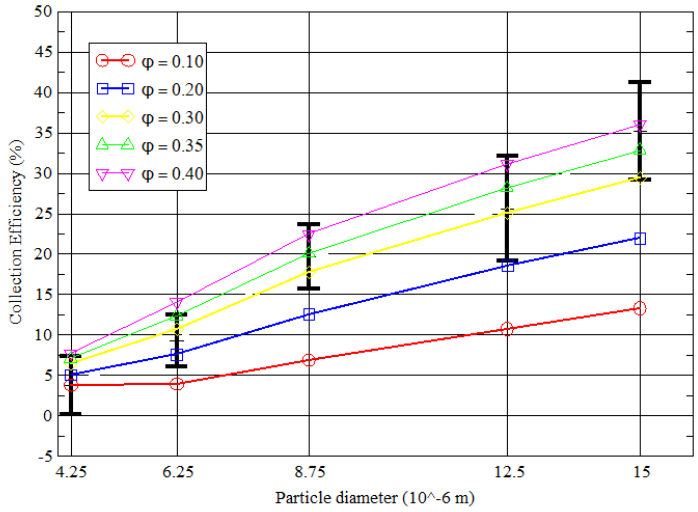

(b) The collection efficiency as a function of D_P. Calculated for l = 0.021 m, d_n = 0.005 m, and ϕ = 0.10, 0.20, 0.30, 0.35, 0.40.

Figure 16: Collection efficiency in the hawthorn hedge due to pure broad leaf collection (a), and collection due to both needle-like and broad leaf collectors. The experimental data is obtained from Tiwary et al. [2006].

It is clear that the altered model was able to reproduce the experimental data. The collection efficiency increased significantly as the effect of the needle-like collectors was introduced, due to the increase of the deposition velocity. For values of ϕ in the range of [0.30-0.40] provided sensible results, but $\phi = 0.35$ provided the best agreement between the simulation results and the experimental data.

6.4 Grid Dependency

In order to make sure that the obtained results are not dependent on the chosen numerical methods and the simulation domain, a grid dependency test was performed. Simulations were performed with the aforementioned grid, and a finer version. The fine mesh consisted of $254 \times 30 \times 114$ control volumes. The maximum cell size was $0.5 \times 1.0 \times 0.5$ m^3. The minimum cell size was $0.04 \times 0.4 \times 0.04$ m^3. The mesh was roughly 4 times as fine as the coarse mesh. Both CDS and QUDS were used to calculate the momentum convection terms. The TKE profile and the velocity profile were extracted at $\frac{x}{10} = H$ downwind of the hedge obstacle. The results are displayed in figure (17a) and figure (17b).
We see that velocity and TKE profiles were very grid dependent when QUDS was used. At the inflection points the difference between the coarse and the fine solution for the velocity was roughly 8%. The difference for the TKE was roughly 9%. The difference between the coarse and the fine solution was significantly lower. For both cases this is roughly 3%. Also, the difference between both the coarse and fine solution with CDS agrees with the solution that was found using QUDS and the fine mesh.

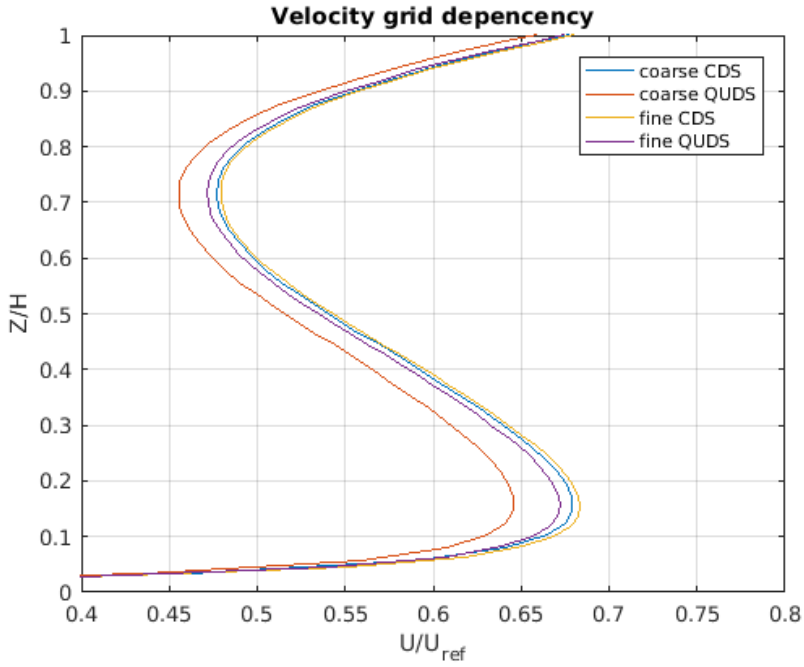

(a) The velocity profile at $\frac{x}{10} = H$ downwind of the hedge for a coarse and a fine mesh using both CDS and QUDS

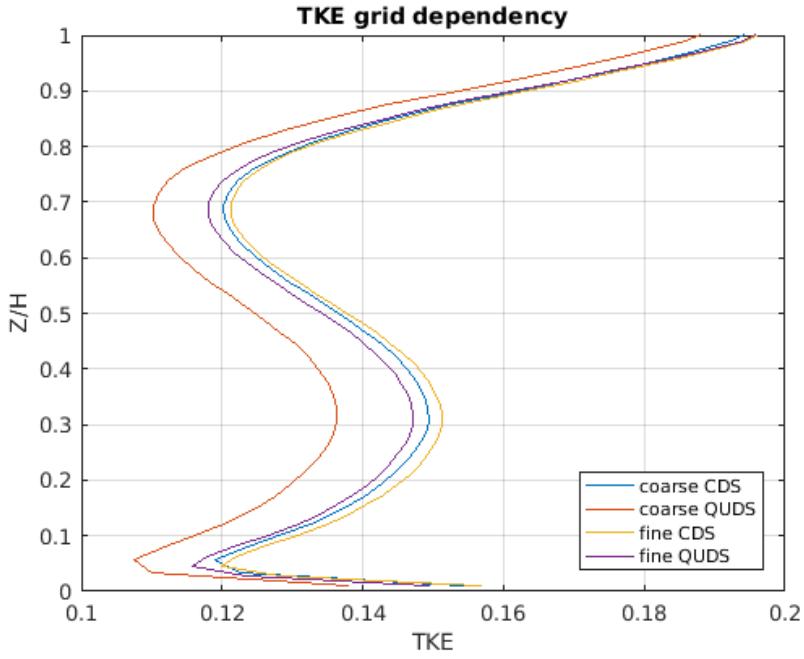

(b) Then TKE profile at $\frac{x}{10} = H$ downwind of the hedge for a coarse and a fine mesh using both CDS and QUDS

Figure 17

Also, the concentration profiles were extracted at the same location. They are displayed in figure (18).

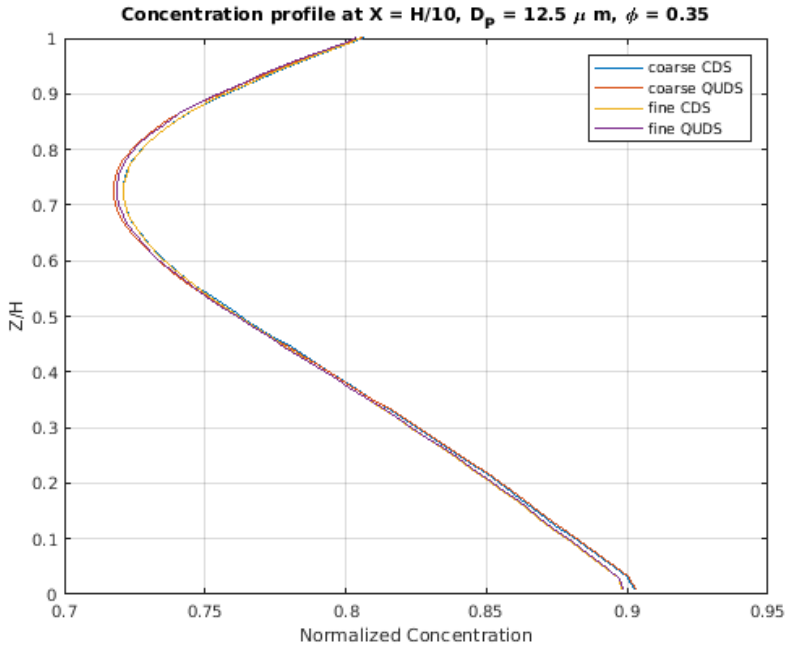

Figure 18: The velocity profile at $\frac{x}{10} = H$ downwind of the hedge for a coarse and a fine mesh using both CDS and QUDS

It is clear that both QUDS and CDS produce grid independent results of the concentration profile. Hence, further simulations were performed with CDS such that a proper solution could be obtained using the coarse mesh. This greatly decreased the overall computation time.

7 Temperature Case Study: Parametric study of the influence of environmental factors and tree properties on the transpirative cooling effect of trees

In order to validate the implementation of the leaf energy balance model, the results from our model are compared to simulations performed by Manickathan et al. [2017]. The authors used a simple domain 2D with a 1 m × 1m vegetation block, and varied the wind speed, air temperature, humidity and solar radiation to determine their effect on the energy balance model. The Leaf Area Density profile of the vegetation was 10.0 $\frac{m^2}{m^3}$. The authors used the RANS equations with a realizable $k-\epsilon$ closure model. The Katul et al. [2004] model was used to calculate the effect of the vegetation on the flow field. The Linear Upwind Difference Scheme was used to model the convective terms in the RANS equations. These numerical models were very similar to the ones that were used in this research. Contours of the velocity, air temperature and the humidity were provided. Also, the temperature profiles and the heat fluxes inside the vegetation were provided. The fact that a similar numerical approach was used, allowed us to validate our implementation of the leaf energy balance model.

The enviromental factors and tree properties used by Manickathan et al. [2017] in their research are displayed in table (2).

Table 2: Tree properties and environmental factors used by Manickathan et al. [2017]

$q_{r,sw}$ $(\frac{W}{m^2})$	$q_{r,lw}$ $(\frac{W}{m^2})$	T_{inlet} $(°C)$	w_{inlet} $(\frac{kg}{kg})$	$r_{s,min}$ $(\frac{s}{m})$	l (m)	C_D
800	400	30	16 $\times 10^{-3}$	150	0.1	0.2

In their research, Manickathan et al. [2017] assumed that stomatal resistance was independent of the radiative flux, such that $r_s = r_{s,min}$.

7.1 Inlet Profiles

The inlet profiles were calculated based on the roughness height and the friction velocity:

$$U(z) = \frac{u_*}{\kappa}\ln\Big(\frac{z+z_0}{z_0}\Big) \tag{115}$$

$$k(z) = \frac{u_*^2}{\sqrt{C_\mu}} \tag{116}$$

$$\epsilon(z) = \frac{u_*^3}{\kappa(z+z_0)} \tag{117}$$

where $z_0 = 0.217\ m$ and $u_* = 0.106\ \frac{m}{s}$. An empty channel simulation was performed with the existing domain and the outlet was used as the inlet for the actual simulation. Plug profiles were used for w and T.

7.2 Simulation Domain

The simulation domain consisted of a 1 m × 5 m × 1 m vegetation block, placed at a height of 0.5 m above the ground. The West boundary was modelled as an inlet, and the distance to the vegetation block was 10 m. The East boundary was modelled as an outlet, and the distance to the vegetation block was 25 m. The Bottom boundary was modelled as a wall, with a

roughness height of 0.0217 m. Temperature of humidity wall functions were excluded, so a zero gradient boundary condition was used for both. The Top boundary was modelled as a symmetry face. The distance to the vegetation blocks was 10 m. The North and South boundaries were modelled as symmetry faces. For both boundaries, the distance to the vegetation blocks was 2 m. A 2D view of the $\hat{x}$-$\hat{z}$ plane of the simulation domain is displayed in figure (19).

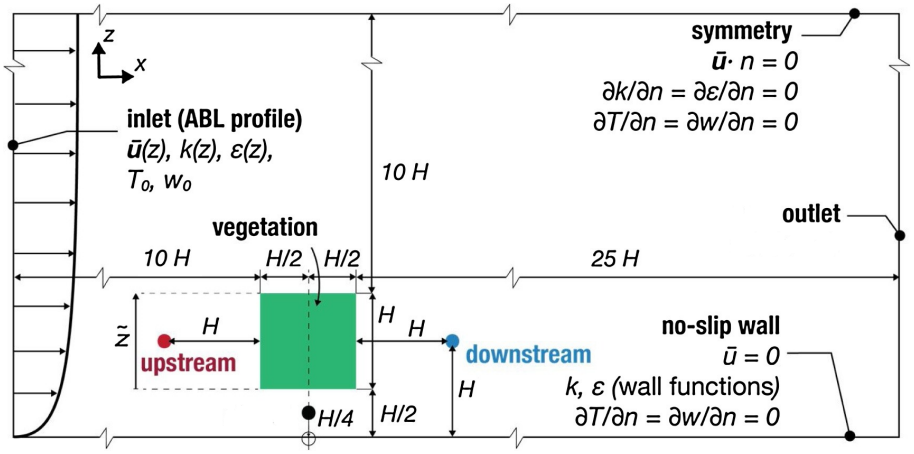

Figure 19: A 2D view of the simulation domain and the boundary conditions that were used to perform the simulations. Obtained from Manickathan et al. [2017]

.

The mesh consisted of 193 × 65 × 85 control volumes. The minimum cell size was 0.05 m × 0.1 m × 0.05 m. The maximum cell size was 0.25 m × 1.0 m × 0.25 m. The expansion factor was 1.05. A total number of 17 × 32 × 17 control volumes were used to mesh the vegetation block. The mesh is displayed in figure (20).

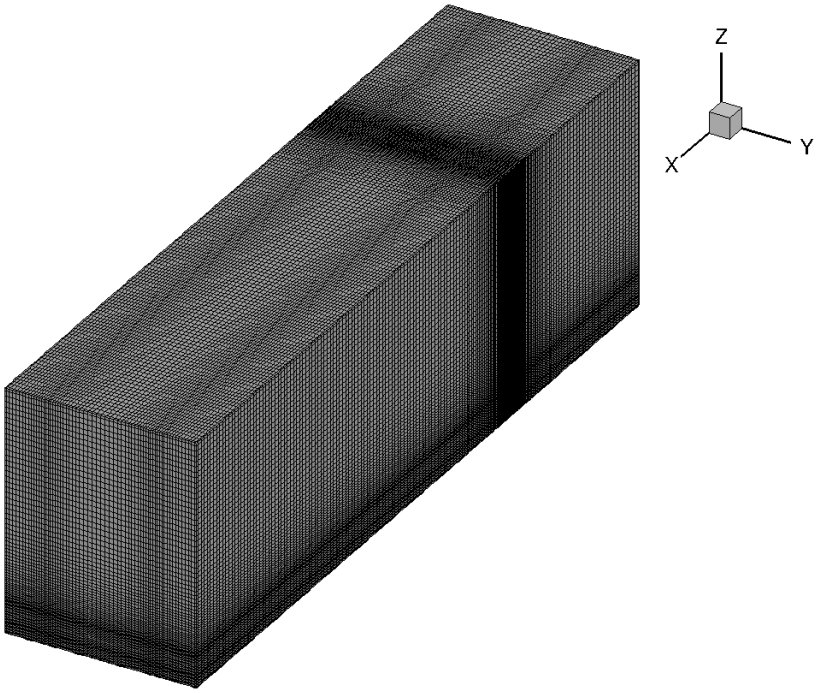

Figure 20: A 3D view of the mesh that was used to perform the simulations.

7.3 Results

The velocity profiles were extracted along the $\hat{x}$ direction, at a height of $z = H$ and $y = 4.5H$, and along the $\hat{z}$ direction at $x = 10.5H$ and $y = 4.5H$. Profiles of the air temperature, the leaf temperature and the humidity were also extracted along the aforementioned lines. Contours of the $\hat{x}$-$\hat{z}$ plane were extracted in the region $x = [8H, 16H]$, $z = [0, 3H]$ at $y = 4.5H$. This was done for u, k, T, w and T_{leaf}. These results are presented in the following section.

The velocity and turbulent kinetic energy profiles extracted along the $\hat{z}$ direction are displayed in figure (21a) and figure (21b). The vegetation is indicated using dashed green lines.

It is clear that the vegetation has a significant effect on the flow field. The velocity decreases significantly as we approach the vegetation. There is a 0.5 m gap between the vegetation block and the ground, which causes the size of the boundary layer to decrease. The form drag of the vegetation forces the air to pass underneath the vegetation, which causes a local increase of velocity. Inside the vegetation, the velocity decreases further as we move along the $\hat{z}$ direction, and starts to increase again at $z/h = 0.75$. Above the vegetation, the velocity increases further to match the free-stream velocity. Turbulent kinetic energy is created at the wall due to friction. As we move away from the wall, the turbulent kinetic energy first decreases, and increases again as we move closer to the vegetation. Inside the vegetation, the turbulent kinetic energy increases, and starts to decreases again above the vegetation.

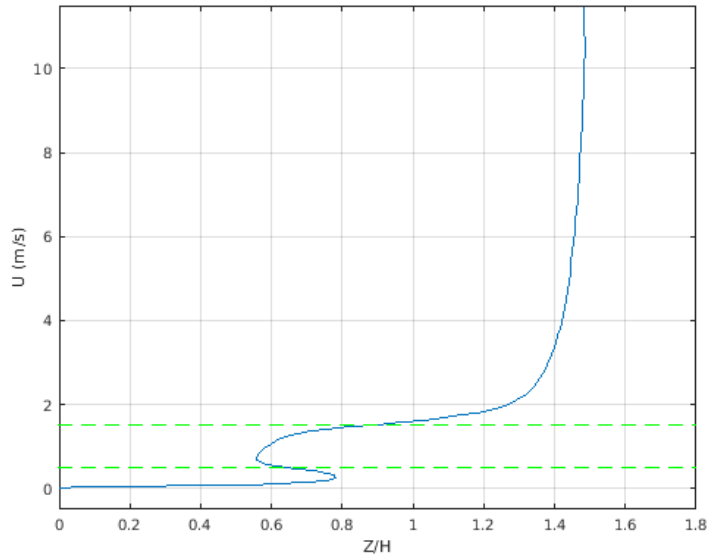

(a) The velocity profile along the $\hat{z}$ axis, extracted at $x/H = 10.5$ and $y/H = 4.5$. The vegetation is indicated using dashed green lines.

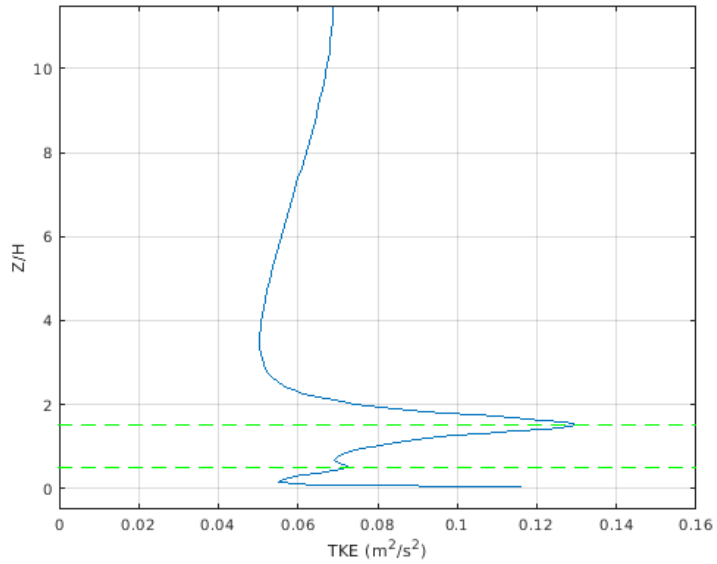

(b) The turbulent kinetic energy profile along the $\hat{z}$ axis, extracted at $x/H = 10.5$ and $y/H = 4.5$. The vegetation is indicated using dashed green lines.

Figure 21: Profiles extracted along the $\hat{z}$ axis, at $x/H = 10.5$ and $y/H = 4.5$.

The profiles of q_{lat}, q_{rad} and q_{sen} are extracted along the $\hat{z}$-axis at $x/H = 10$ and $y/H = 4.5$ are displayed in figure (22). In the same figure, the profiles of the fluxes obtained are Manickathan et al. [2017] are shown. The same is done for T_{leaf} and T in figure (23).

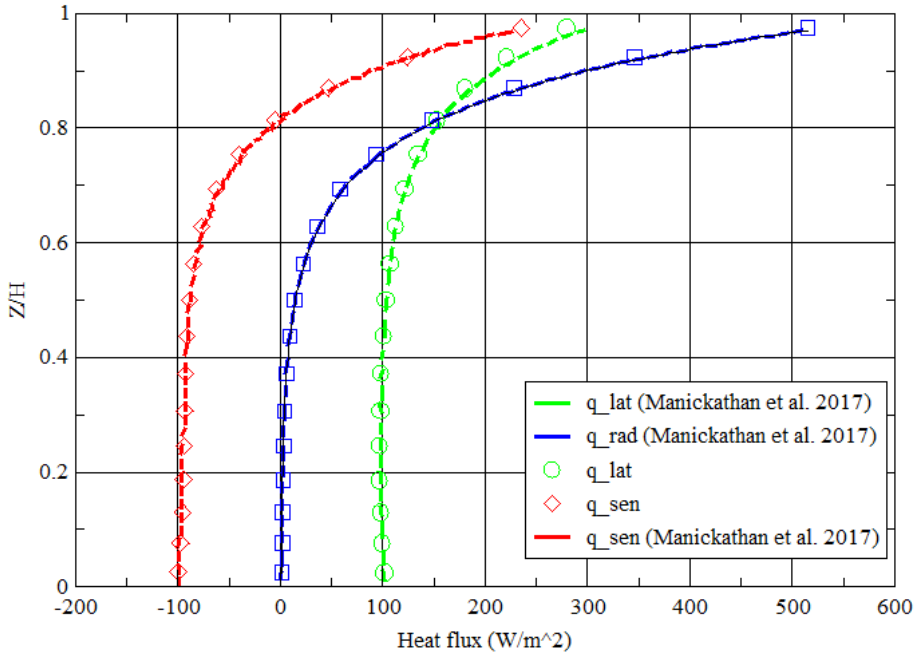

Figure 22: The heat flux profiles inside the vegetation, in $\frac{W}{m^2}$, extracted at $y/H = 4.5$, $x/H = 10.5$.

The flux profiles displayed in figure (22) showcase the physical behaviour of the Leaf Energy Balance Model. The figure also includes the profiles obtained by Manickathan et al. [2017]. Near the ground, q_{lat} approaches zero, due to the blockage of the individual leaves of the vegetation. It increases slowly until $z/H = 0.6$, after which it increases exponentially, in accordance with the Lambert-Beer law. Also, as was shown in figure (21a), the streamwise velocity is also reduced in the lower part of the vegetation. This means that r_a has to be large, according to formula (3.11). This is reflected in the behaviour of q_{lat}, which is directly related to both the resistances, as described in formula (3.7) and (3.8). In the lower part of the vegetation q_{lat} remains stable, and starts to increase as q_{rad} increases and r_s decreases. Near the top of the vegetation, q_{lat} increases rapidly, but not as fast as q_{rad}. This causes the sensible heat flux to become positive near the top of the vegetation. This means that near the top of the vegetation the air will be heated due to the incoming radiation. The heat flux profiles obtained in this research are very similar to the ones obtained by Manickathan et al. [2017].

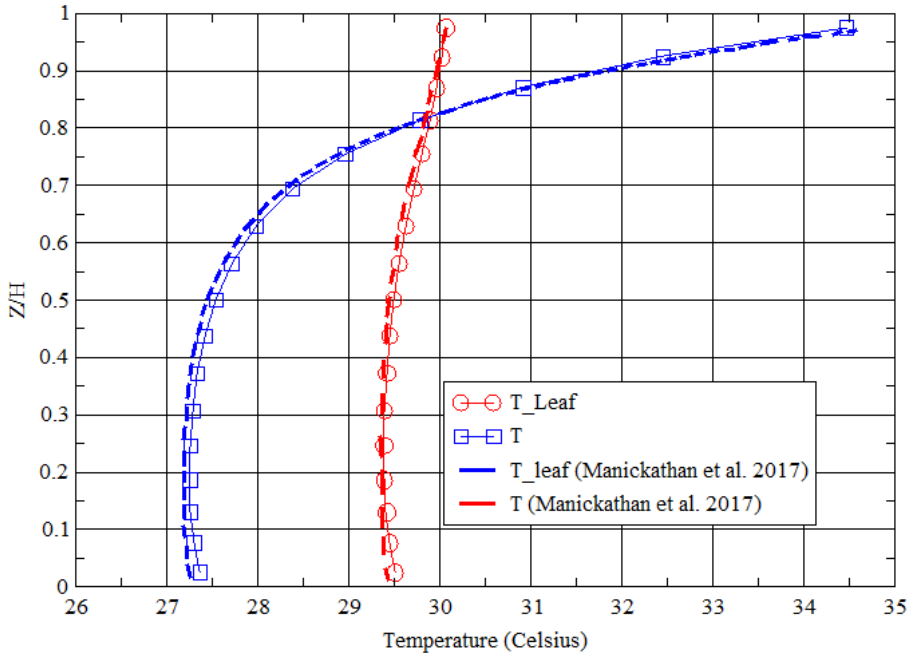

Figure 23: The air and the leaf temperature inside the vegetation, extracted at $y/H = 4.5$, $x/H = 10.5$.

The temperature profiles displayed in figure (23) show the effect of the heat flux profiles on T and T_{leaf}. Near the the bottom of the vegetation, T_{leaf} is the lowest, due to a lack of heating by incoming radiation and the fact that transpiration still occurs. As a result, the air temperature is reduced significantly. At $z/H = 0.2$, T_{leaf} and T increase slightly. Around $z/H = 0.6$ the leaf temperature starts to increase more rapidly due to increase of q_{rad}. q_{sen} decreases, which decreases the cooling effect of the vegetation. Near the top of the vegetation, q_{rad} is so large that T_{leaf} exceeds the inlet temperature. As a result, the sign of q_{sen} changes, which causes the air temperature to increase again. Near the top of the vegetation, the air temperature exceeds the inlet temperature. The profiles obtained are similar to the ones obtained in the research performed by Manickathan et al. [2017]. However, in the lower part of the vegetation, $x/H < 0.8$, both the leaf and the air temperature are slightly lower. Also, in the top part of the vegetation, $z/H > 0.8$, both temperatures are slightly higher.

In order to illustrate the global effect of the vegetation on the flow-field, the temperature, and the humidity, contours are extracted. The contours of the $\hat{x}$-$\hat{z}$ plane are extracted for the magnitude of the velocity, $|U|$, the air temperature, T, the humidity, w, and the turbulent kinetic energy, k. Manickathan et al. [2017] provided contours of $|U|$, T and w. The following figures display the contours extracted during this research, and the ones obtained by Manickathan et al. [2017]. The contours of $|U|$, T, w and k are displayed in figures (24), (25), (27), (28), (29), (30) and (26). Manickathan et al. [2017] have centered the $\hat{x}$-axis at 10.5 m.

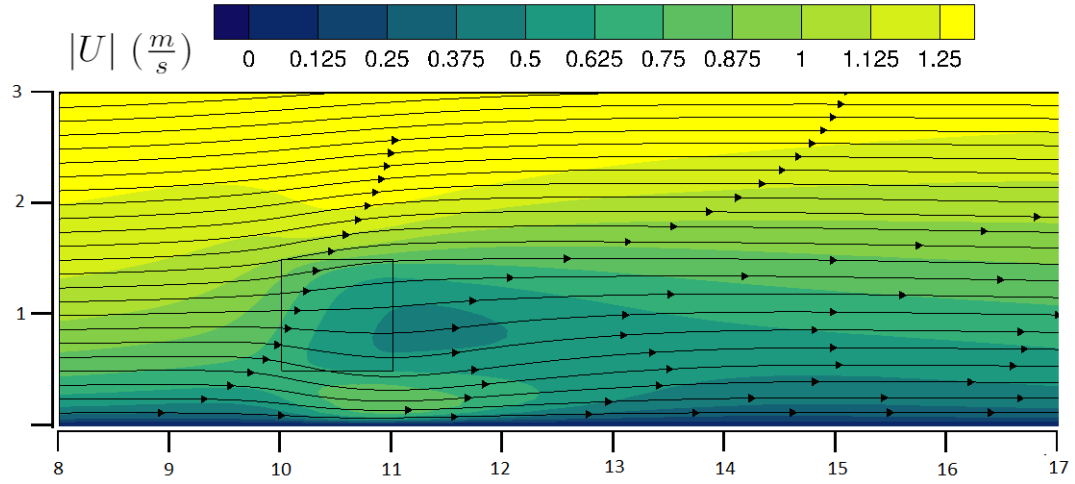

Figure 24: The magnitude of the velocity, $|U|$ $(\frac{m}{s})$, extracted at $y/H = 4.5$, $x = [8H, 16H]$ and $z = [0, 3H]$.

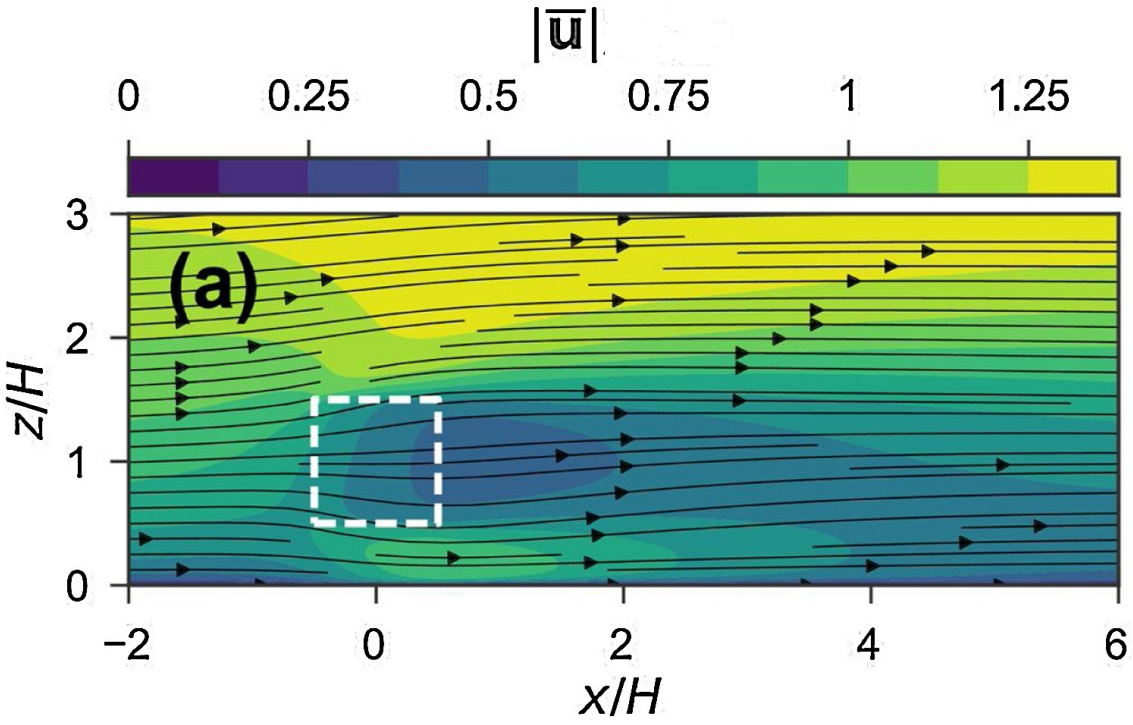

Figure 25: The magnitude of the velocity, $|U|$ $(\frac{m}{s})$, obtained by Manickathan et al. [2017].

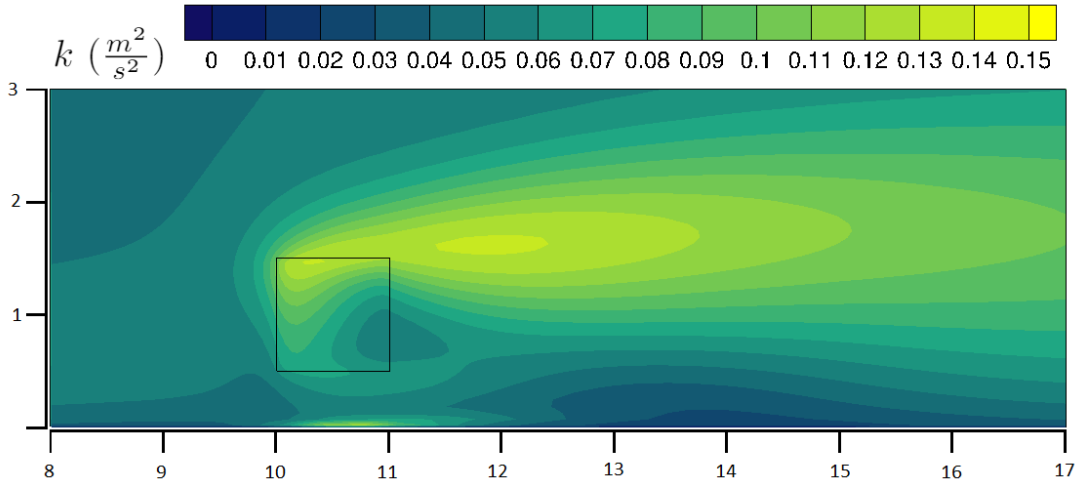

Figure 26: The turbulent kinetic energy, k $(\frac{m^2}{s^3})$, extracted at $y/H = 4.5$, $x = [8H, 16H]$ and $z = [0, 3H]$.

It is clear that the obtained flow field shows resemblance to the flow field obtained by Manickathan et al. [2017]. Beneath the vegetation, the size of the boundary layer decreases due to the flow being forced downwards. Inside the vegetation, $|U|$ decreases, and reaches its minimum value at the downwind edge of the vegetation. Down-wind of the vegetation, the same characteristic reduction of the velocity is observed. In this work, the upper part of the flow field $z/H > 2.5$, remains relatively unchanged. This is was not observed by Manickathan et al. [2017], where the velocity up-wind velocity in the upper part of the domain increases as we approach the vegetation.

The vegetation has a significant effect on the turbulent kinetic energy. We can clearly observe that the vegetation acts both as a sink, and a source of turbulent kinetic energy. At the top of the vegetation, we see that turbulent kinetic energy is being generated. The turbulent kinetic energy is also increased downwind of the vegetation, where recirculation is present. Below the vegetation, we observe an increase of turbulent kinetic energy.

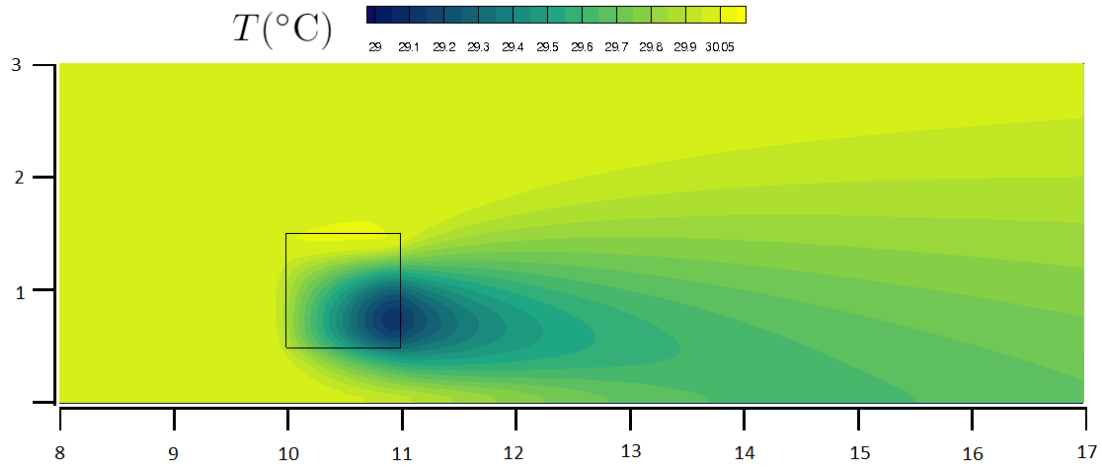

Figure 27: The air temperature, T $(°C)$, extracted at $y/H = 4.5$, $x = [8H, 16H]$ and $z = [0, 3H]$.

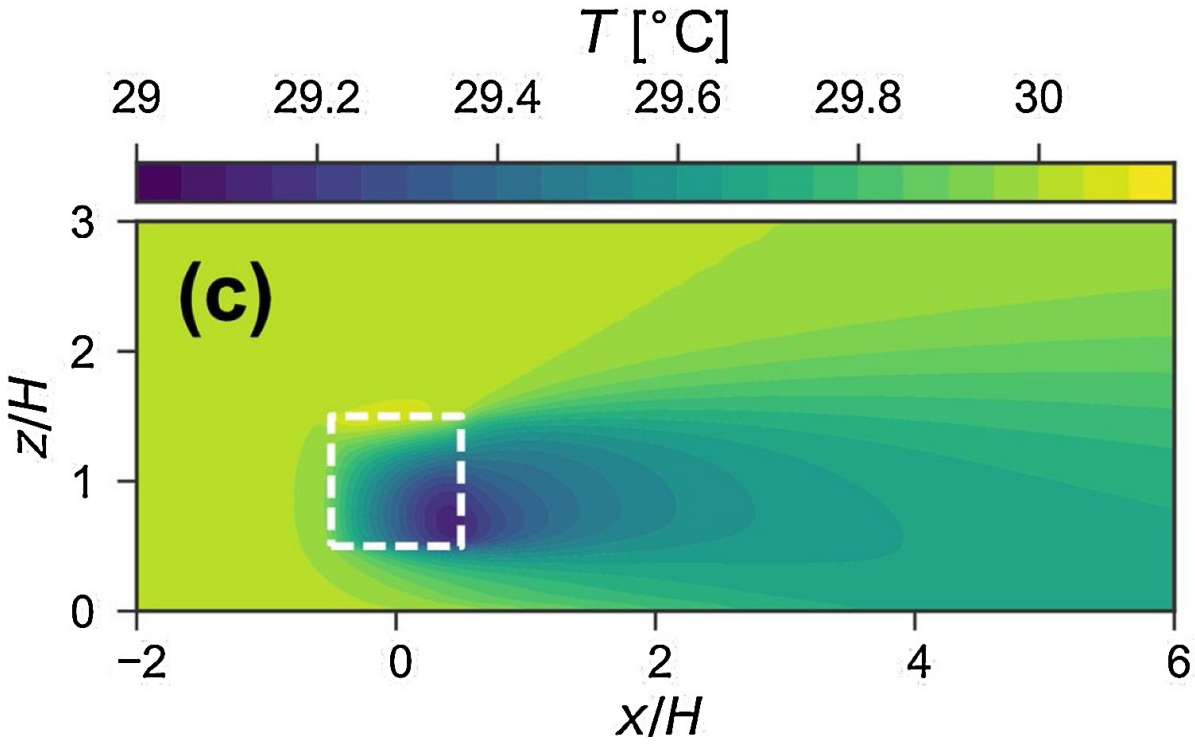

Figure 28: The air temperature, T $(°C)$, obtained by Manickathan et al. [2017].

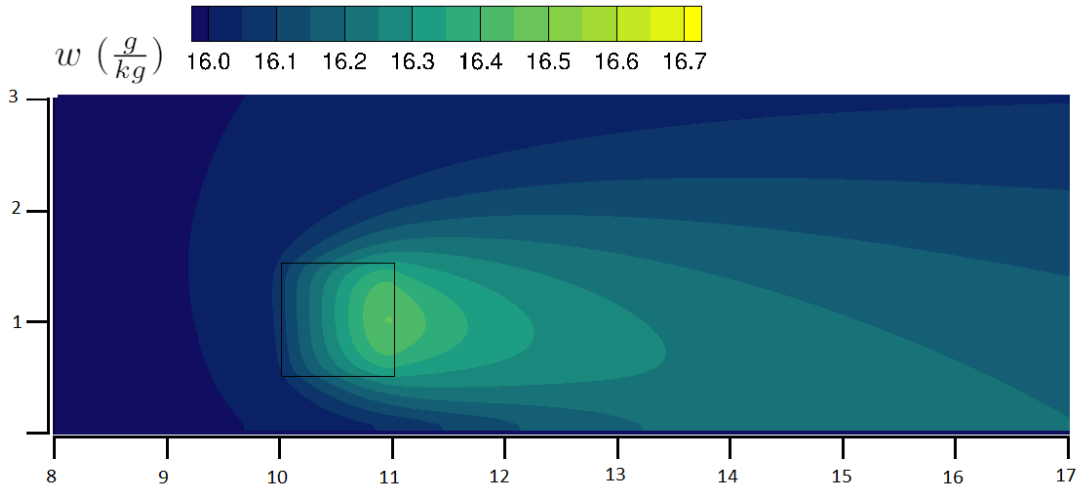

Figure 29: The humidity, w $(\frac{g}{kg})$, extracted at $y/H = 4.5$, $x = [8H, 16H]$ and $z = [0, 3H]$.

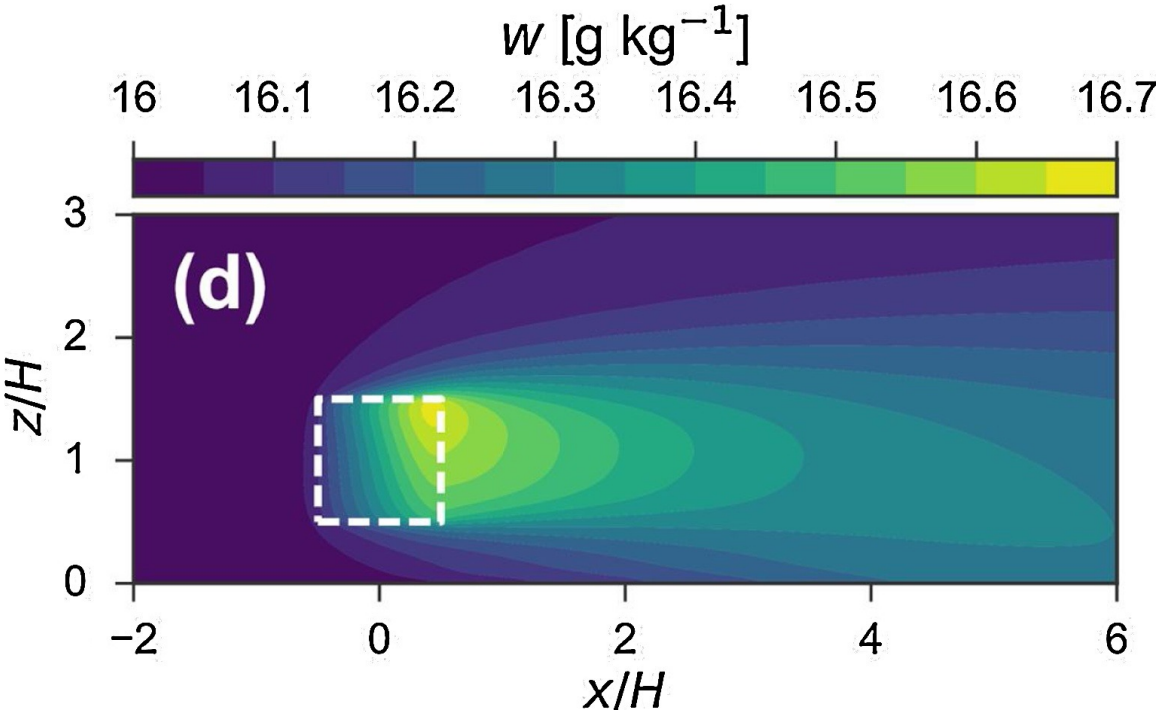

Figure 30: The humidity, w $(\frac{g}{kg})$, obtained from Manickathan et al. [2017].

The temperature field obtained in this research shows resemblance to the temperature field obtained by Manickathan et al. [2017]. A local increase of temperature is observed near the top of the vegetation due to radiative heating which is dominant there. The temperature drops as we approach the bottom of the vegetation. The local minimum, $T = 29.1\ ^{\circ}C$, is observed at the trailing edge of the vegetation near the bottom. The minimum temperature obtained by Manickathan et al. [2017] is roughly $T = 29\ ^{\circ}C$. The influence of the vegetative cooling can also be seen downwind of the vegetation. The shapes of the contours are not exactly equal. In this work, the contours have more rounded shapes and are pointed downward. This is less pronounced in contour obtained by Manickathan et al. [2017].

The most significant difference between the results of this research and the case study can be observed for the humidity. It is clear that both the shape of the contour and the maximum value of the humidity differ significantly. In this research, the maximum, $w = 16.45\frac{g}{kg}$, occurs at the trailing edge of the vegetation at roughly $z/H = 1$. In the case study, the maximum value is $w = 16.7\frac{g}{kg}$, and occurs at the trailing edge at $z/H = 1.5$. Also, the downwind shape of the contours are not as rounded and are roughly horizontal, compared to the downward orientation that can be observed in the contour obtained in this research.

7.4 Difference Scheme Sensitivity

Manickathan et al. [2017] used the Linear Upwind Difference Scheme to model the convection terms in the RANS equations. The LUDS scheme can display numerical diffusion and grid dependency. This could have an impact on the performance of the Leaf Energy Balance model. Therefore, the aforementioned simulations are repeated using the Quadratic Upwind Differencing Scheme and the Central Differencing Scheme. Profiles are extracted along the previously defined $\hat{x}$ and $\hat{z}$ direction to display the difference between the different convergence schemes. The profiles of U, k, T, and T_{leaf} along the $\hat{x}$ axis are displayed in figure (31). The profiles extracted along the $\hat{z}$ axis are displayed in figure (32).

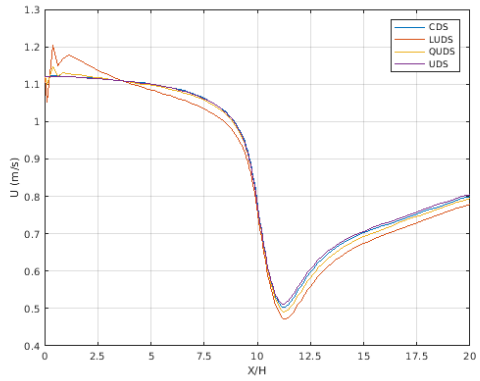

(a) U

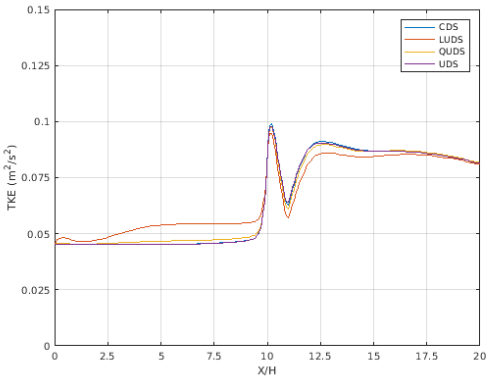

(b) k

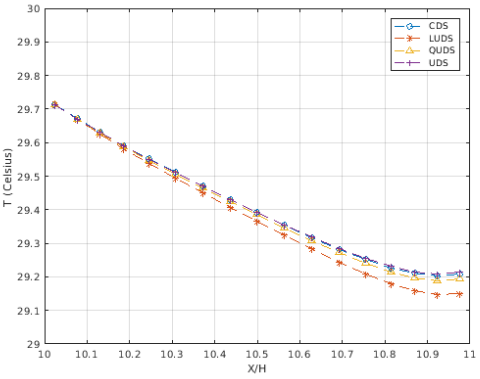

(c) T

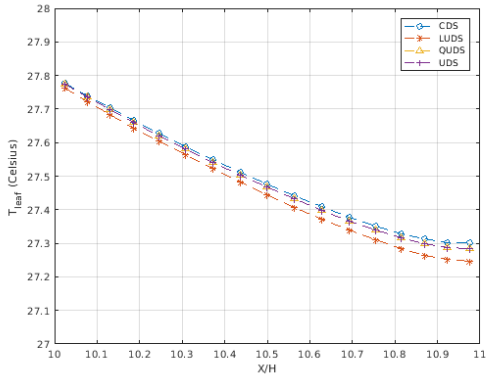

(d) T_{leaf}

Figure 31: The profiles along the $\hat{x}$-axis at $y/H = 4.5$, $z/H = 1$.

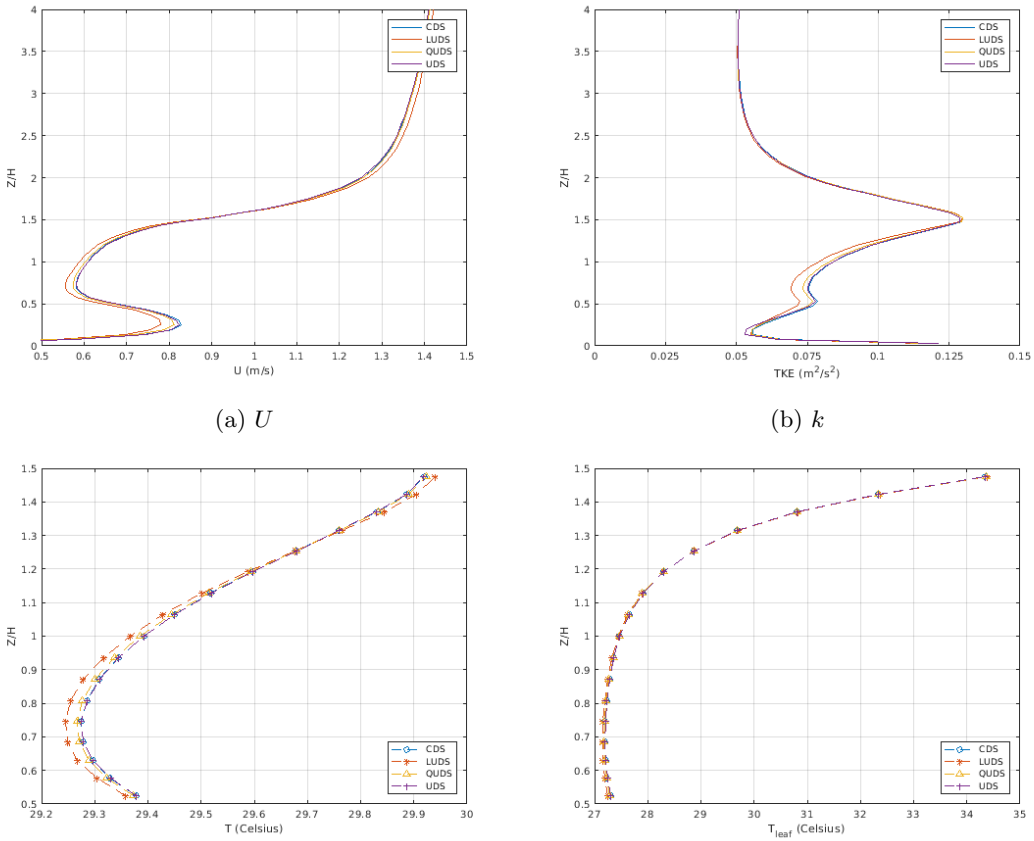

(a) U (b) k

(c) T (d) T_{leaf}

Figure 32: The profiles along the $\hat{z}$-axis at $y/H = 4.5$, $x/H = 10.5$.

The standard deviation of the differences between the results obtained using LUDS versus UDS, QUDS and CDS, normalized with the means of the LUDS profiles, are displayed in the following table.

Table 3: Standard deviations of the differences between the results obtained using LUDS versus UDS, QUDS and CDS, normalized with the means of the LUDS profiles.

	U		k		T		T_{leaf}	
	x	z	x	z	x	z	x	z
UDS	0.0997	0.0156	0.0695	0.0315	7.028E-04	6.311E-05	5.880E-04	1.10E-03
CDS	0.0994	0.0149	0.0693	0.0309	6.351E-04	6.152E-05	4.462E-04	1.00E-03
QDS	0.0495	0.0106	0.0548	0.0223	4.676E-04	4.762E-04	3.123E-04	7.522E-04

It is clear that the difference schemes have a number of effects on the simulation results. First, in figure (34a) and (34b), we observe that the unphysical behaviour at the inlet that was seen in figure (**??**) and (**??**), vanishes if any of the other difference schemes are used. With LUDS, UDS, or QUDS, the velocity remains steady in the first cells, after which it starts to decrease as the presence of the vegetation is felt. The same thing is observed for the turbulent

kinetic energy. Using the other difference schemes, the turbulent kinetic energy remains constant until we approach the trailing edge of the vegetation. Secondly, we see that the LUDS scheme produces values for T and T_{leaf} that are $0.05°C$ lower at the trailing edge of the vegetation, compared to the other schemes. Thirdly, along the $\hat{z}$-axis, we see that we obtain lower values of the velocity and the turbulent kinetic energy below and within the vegetation, when LUDS is used. Fourthly, the air temperature obtained using LUDS is lower near the bottom of the vegetation, and higher near the top of the vegetation, compared to the other difference schemes. The leaf temperature profile along the $\hat{z}$-axis is not affected by the different difference schemes. In general, no major differences are observed between UDS, QUDS, and CDS.

The UDS is highly numerically diffusive, so we would expect that the results obtained using this scheme would be different from the results obtained using LUDS, CDS and QUDS. These are second-order schemes, which should in theory lead to less numerical diffusion and more accurate results. As this is not the case in this work, we expect that the LUDS scheme is especially sensitive to the mesh that was used in this work, leading to unphysical results. As we the results from CDS and QUDS were similar to the result from UDS, we conclude that numerical diffusion plays a significant role, even when using second order upwind schemes.

8 Temperature Case Study: Measurement of microclimate characteristics and transpiration of an Impatiens pot plant crop in a greenhouse

In order to validate the accuracy and robustness of the leaf energy balance model, we performed a case study. The exact configuration of the experiment was replicated, and simulations were performed. The results from the simulations were compared with the experimental data. A case study was selected that included both measurements of the leaf temperature, and the temperature of the air above the vegetation. This allows us to validate multiple parts of the leaf energy balance model. The respective measurements were performed by Kichah et al. [2012].
The authors performed measurements on potted impatiens, elevated on benches at a height of 0.8 m. The plants were placed in a greenhouse, with a shading screen. The velocity of the air was measured at 1.12, 1.35 and 1.5 m above the ground. An aspirated probe was used to measure the air temperature of the air in the middle of the vegetation at a height of 1.125 m above the ground. Copper-constantan thermocouples were glued to the underside of the leaves and the used measure the the leaf temperate at 0.9, 1.125 and 1.35 m above the ground in the middle of the vegetation. Another aspirated probe, shielded from the solar radiation, was used to measure the ground temperature. The measurements performed on July 15th, 2009 are used. The Leaf Area Index of the plants was provided as 3.95 $\frac{m^2}{m^2}$. This gives us a Leaf Area Density of 8.78 $\frac{m^2}{m^3}$. The leaf size was not provided. The drag coefficient was listed as $C_D = 0.32$. The experimental setup that was used is displayed in figure (33).

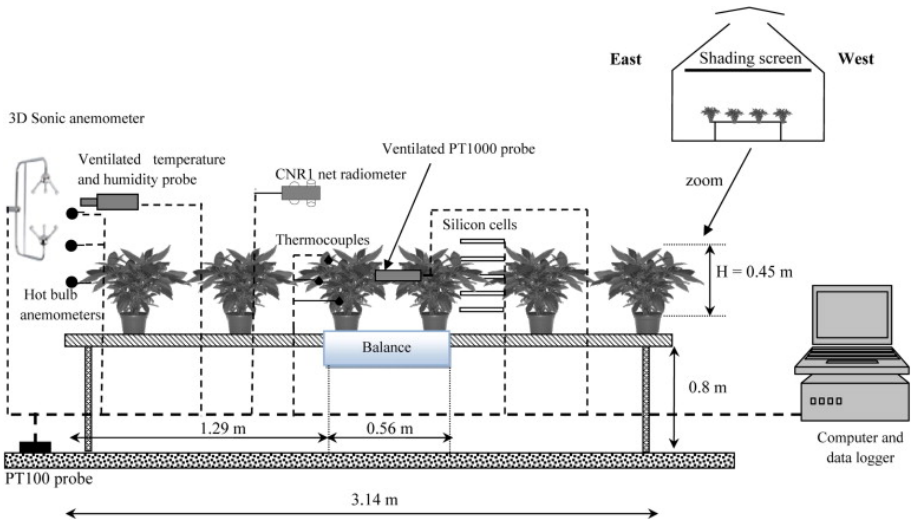

Figure 33: The experimental setup that was used to measure the velocity profile, the leaf temperature and the air temperature of air above the vegetation. Obtained from Kichah et al. [2012]

.

The measurements performed by Kichah et al. [2012] have previously been used to validate the 2D RANS, $k-\epsilon$ model solver with a leaf energy balance model, mentioned in the previous section. Our approach is largely based on their work, which is also used to compare our results.

Manickathan et al. [2017] provided a contour of the leaf temperature in their paper, and also provided contours of the velocity and the humidity through personal communication. In order to compare our results, contours were extracted of the $\hat{x}$-$\hat{y}$ plane. The elemental factors and tree properties are listed in the following table.

Table 4: Tree properties and environmental factors used by Manickathan et al. [2017]

$q_{r,sw}$ $(\frac{W}{m^2})$	$q_{r,lw}$ $(\frac{W}{m^2})$	T_{inlet} $(°C)$	w_{inlet} $(\frac{kg}{kg})$	$r_{s,min}$ $(\frac{s}{m})$	l (m)	C_D
99	522	32	6.21×10^{-3}	450		0.32

The leaf size of the impatiens is not listed. Therefore, multiple simulations were performed with different values for the leaf size. We assumed that the leaf size would be in the same order as the size of the flowers, which is 2-3 cm. We performed simulations with $l = [0.01, 0.025, 0.05, 0.10, 0.15]$ m.

8.1 Inlet Profiles

The inlet profiles are calculated based on the roughness height and the friction velocity:

$$U(z) = \frac{u_*}{\kappa} \ln\Big(\frac{z + z_0}{z_0}\Big) \tag{118}$$

$$k(z) = \frac{u_*^2}{\sqrt{C_\mu}} \tag{119}$$

$$\epsilon(z) = \frac{u_*^3}{\kappa(z + z_0)} \tag{120}$$

where $z_0 = 0.217\ m$. u_* is calculated based on the velocity at a height of 1.1 m, which is $U(1.1) = 0.048\ \frac{m}{s}$.

8.2 Simulation Domain

The simulation was performed by assuming that the individual rows of potted plants could be modelled as continuous blocks along the length of the table that they sat on. The pots were modelled as solid obstacles. The thickness of the table was not provided, so its thickness was assumed to be 0. The East face was modelled as an inlet, the West face as an outlet. The Top face was modelled as a symmetry boundary, and the South face as a wall. The North and South faces were modelled as symmetry faces. The pot and plants obstacles were uniform in $\hat{y}$ direction and measured 5 m in the $\hat{y}$ direction. A distance of 1 m between the pot and plants in that direction was included in the domain. A 2D view of the x-z plane of the simulated domain and the boundary conditions is displayed in figure (34).

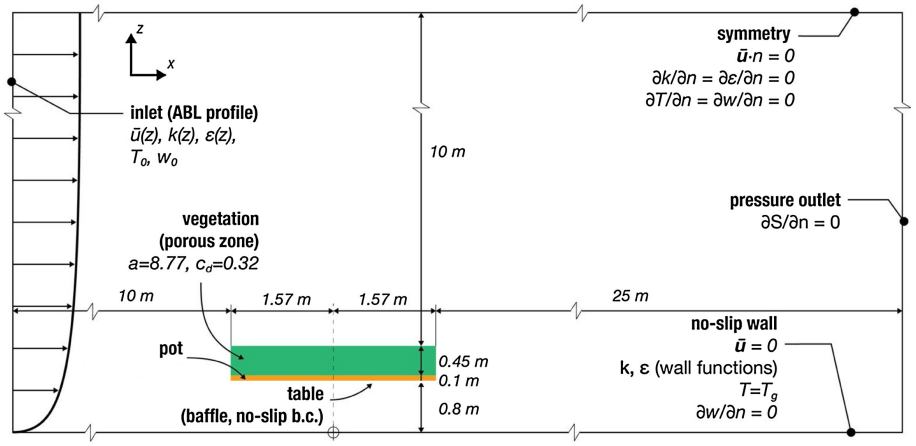

Figure 34: The simulation domain and the boundary conditions that were used to perform the simulations. Obtained from Manickathan et al. [2017]

.

The mesh consisted of 158 × 87 × 74 control volumes. The minimum cell size was 0.05 m × 0.1 m × 0.05 m. The maximum cell size was 1.0 m × 1.0 m × 1.0 m. The expansion factor was 1.05. A total number of 51 × 35 × 8 control volumes were used to mesh the vegetation block. The mesh is displayed in figure (35).

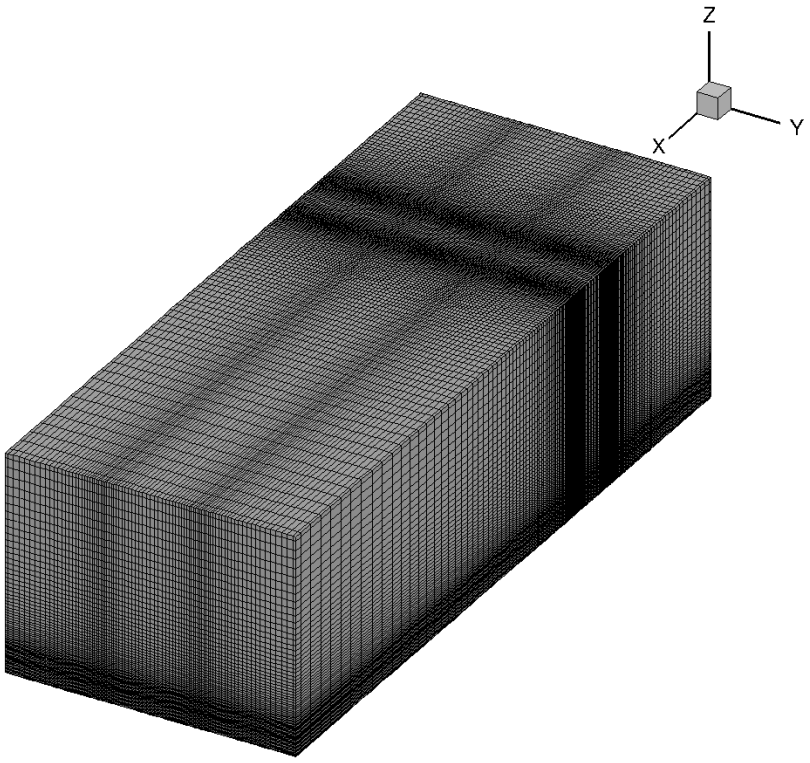

Figure 35: A 3D view of the mesh that was used to perform the simulations.

8.3 Results

The flow field results of the simulations are not fully convergent. The residual of U, V, W, p, and k drops to 10^{-2}, but the residual of ϵ remains above 10^4. The residual of T and w are of the order 10^{-3} and 10^{-7} respectively.
The obtained leaf temperatures for the different sizes of l have been displayed alongside the numerical results by Manickathan et al. [2017], and the experimental results by Kichah et al. [2012] in figure (36).

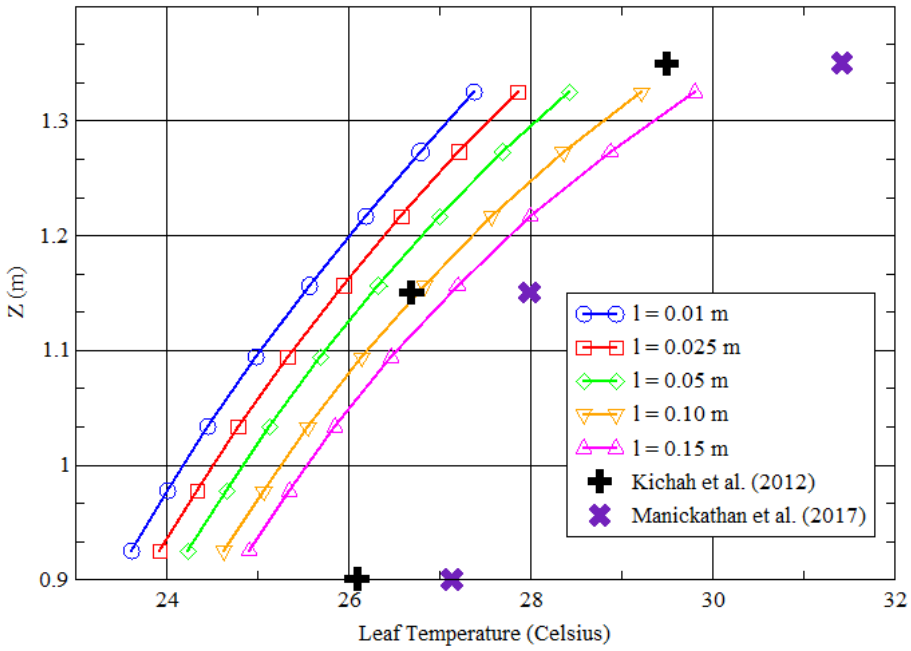

Figure 36: The obtained leaf temperatures for the different sizes l, the numerical results obtained by Manickathan et al. [2017] and the experimental results obtained by Kichah et al. [2012]

.

The obtained air temperature above the vegetation for the different sizes of l has been displayed alongside the numerical results by Manickathan et al. [2017], and the experimental results by Kichah et al. [2012] in the following table.

It is clear that the leaf size influences the cooling power of the vegetation through the aerodynamic resistance. As the leaf size increases, the cooling power decreases as described in equation (3.11). The plots also clearly show that our implementation of the leaf energy balance model is not able to reproduce the experimental results by Kichah et al. [2012] perfectly. Near the bottom of the vegetation, the cooling is a lot more pronounced. Even for $l = 0.15$ m, $\Delta T_{leaf} == 1.2°C$. The difference is still present in the middle and at the top of the vegeta-

Table 5: The air temperature at the top of the vegetation

	Manickathan et. al [2017]	Kichah et. al [2012]	l (m)				
			0.01	0.025	0.05	0.10	0.15
T $°C$	28.1	28.55	27.72	28.21	28.68	29.24	29.54

tion, but less evident. The $l = 0.10$ m profile corresponds well with those measurements. The opposite behaviour is observed for the result by Manickathan et al. [2017]. In that work the leaf temperature is systematically overestimated, but has the best agreement near the bottom of the vegetation.

In order to visualize the the parameters that dictate the values of the leaf temperature, contours of U, k, T, and w are extracted at $y = 7.5$ m, $x = [7.575, 18.575]$ m, $z = [0, 3]$ m. The contour of T_{leaf} is extracted at $y = 7.5$ m, $x = [9, 12.15$ m, $z = [0.9, 1.35]$ m. This is done for the simulation perfomed with $l = 0.025$ m. The contours are displayed in figure (37a), (38), (38), (39), (40a), and (). The result obtained by Manickathan et al. [2017] are displayed alongside those contours in figure (37b), (40b), and (41b). The $\hat{x}$-axis has been centered at $x = 10.575$ m in all figures.

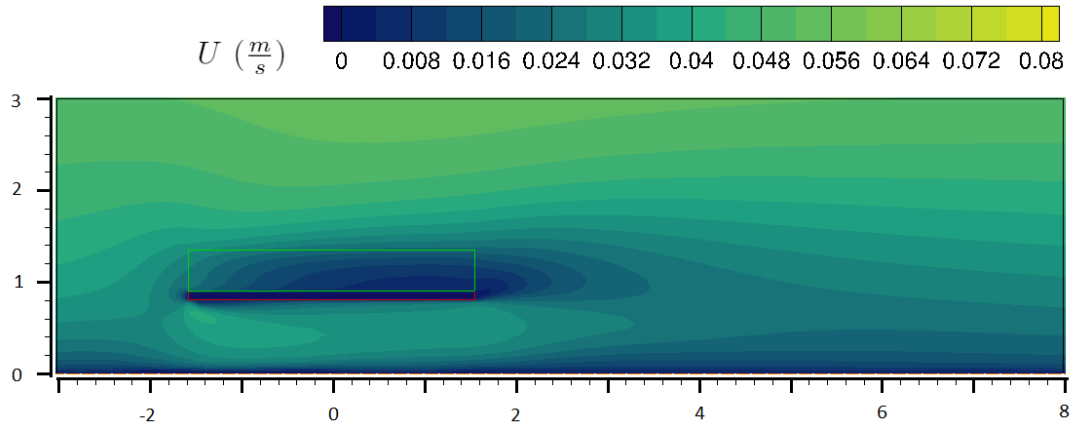

(a) The velocity, U $(\frac{m}{s})$, extracted at $y = 7.5$ m, $x = [7.575, 18.575]$ m, $z = [0, 3]$ m. The pots and vegetation are indicated with red and green respectively. $l = 0.025$ m

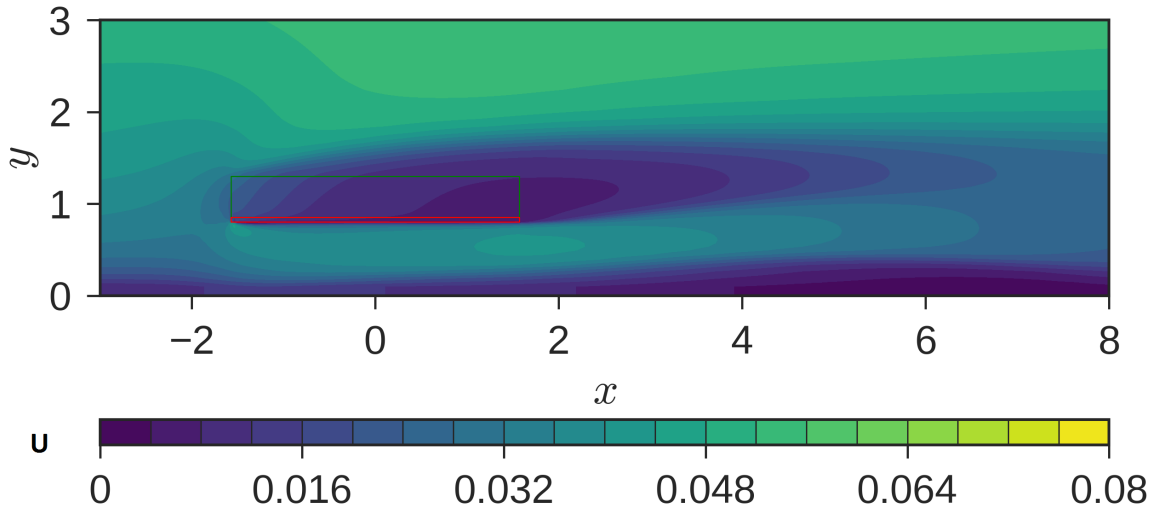

(b) The velocity, $|U|$ $(\frac{m}{s})$, obtained by Manickathan et al. [2017].

Figure 37

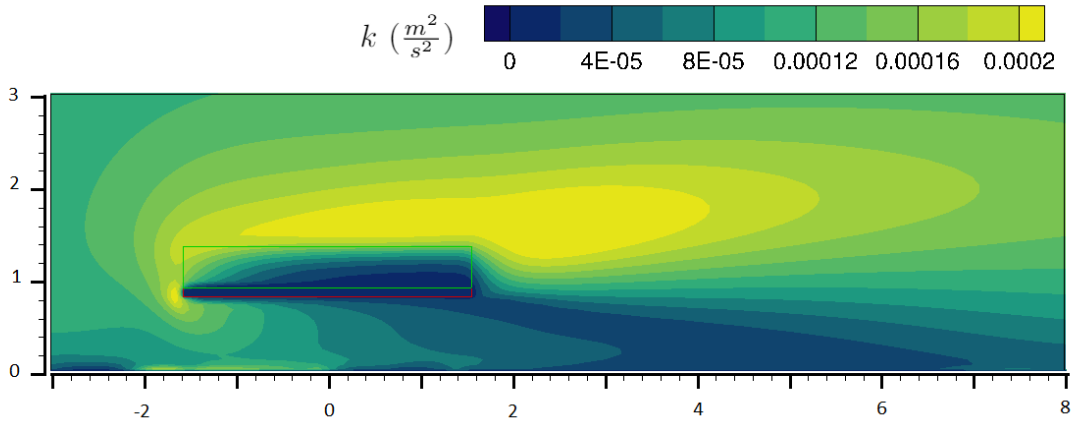

Figure 38: The turbulent kinetic energy, k $(\frac{m^2}{s^2})$, extracted at $y = 7.5$ m, $x = [7.575, 18.575]$ m, $z = [0, 3]$ m. The pots and vegetation are indicated with red and green respectively. $l = 0.025$ m

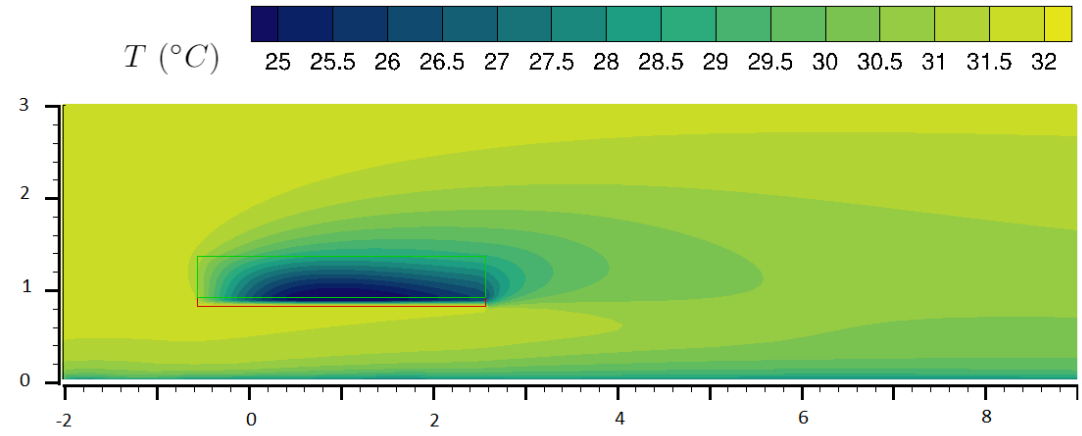

Figure 39: The air temperature, T $(°C)$, extracted at $y = 7.5$ m, $x = [7.575, 18.575]$ m, $z = [0, 3]$ m. The pots and vegetation are indicated with red and green respectively. $l = 0.025$ m

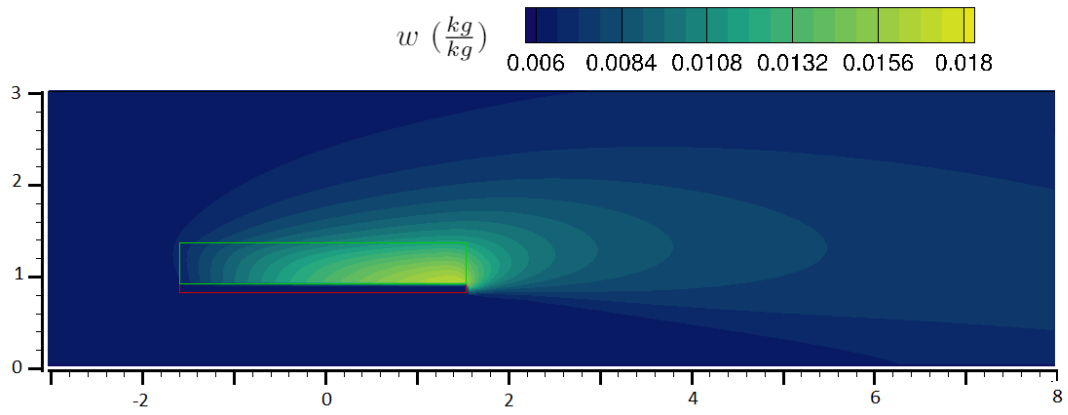

(a) The humidity, w $(\frac{kg}{kg})$, extracted at $y = 7.5$ m, $x = [7.575, 18.575]$ m, $z = [0, 3]$ m. The pots and vegetation are indicated with red and green respectively. $l = 0.025$ m

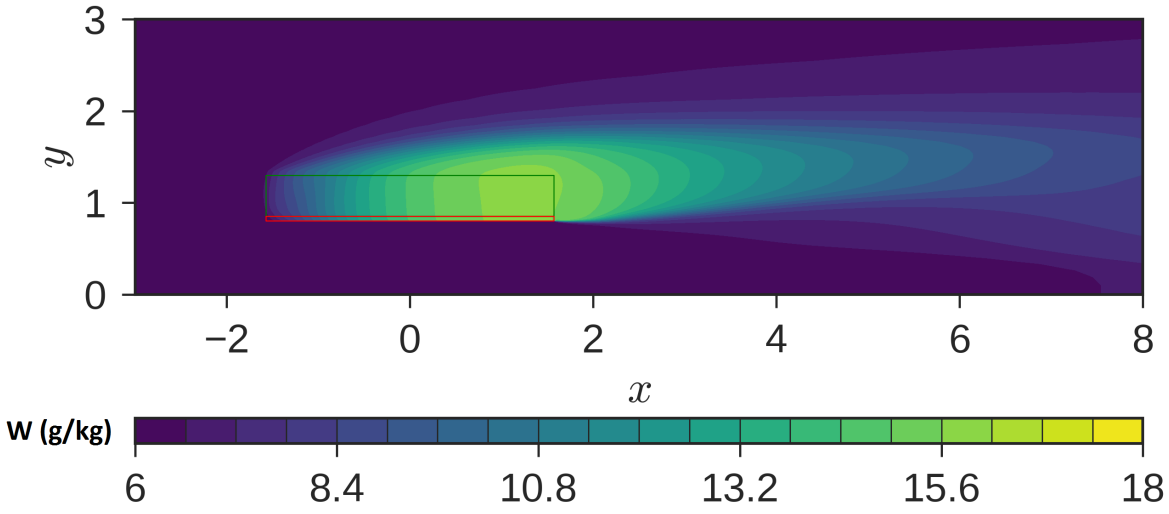

(b) The humidity, w $(\frac{g}{kg})$, obtained by Manickathan et al. [2017].

Figure 40

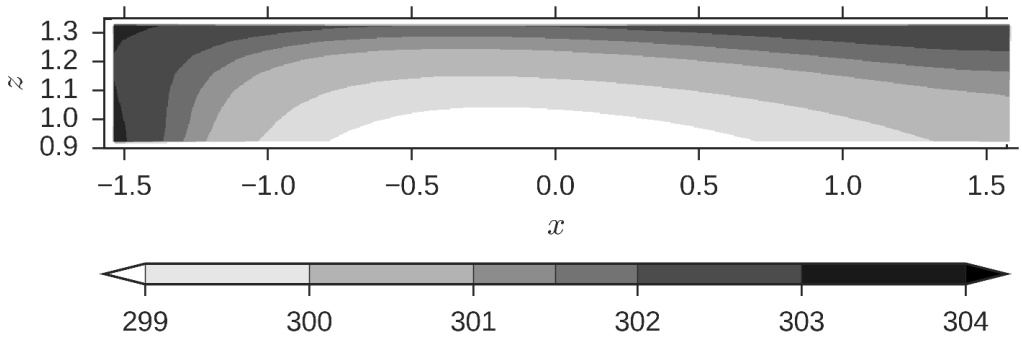

(a) The leaf temperature, T_{leaf} T ($^\circ K$), extracted at $y = 7.5$ m, $x = [7.575, 18.575]$ m, $z = [0, 3]$ m. The pots and vegetation are indicated with red and green respectively. $l = 0.025$ m

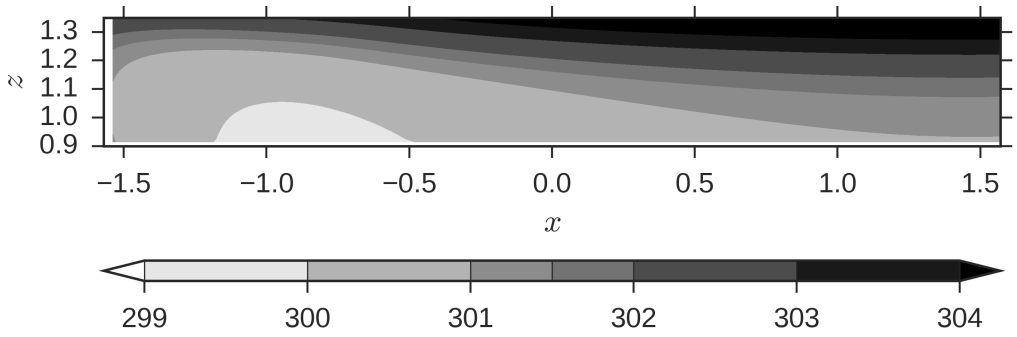

(b) The humidity, T_{leaf} ($^\circ K$), obtained by Manickathan et al. [2017].

Figure 41

It is evident that there are large differences between the results of this research and the work by Manickathan et al. [2017]. The contours of the velocity show that the slowdown inside the vegetation is not as pronounced in this work. The contours levels are a lot flatter, which indicates that the velocity increases more quickly as we move away from the pots.

The fact that the velocity contours do not match, is also visible in the contours of the humidity. Roughly the same maximum cooling power is observed, at the trailing edge of the vegetation near the pots. However, again the shape of the contour levels differ significantly. The levels are flatter, so the humidity decreases more quickly when moving away from the pots.

The contour of the turbulent kinetic energy showcases physical behaviour that is similar to the results obtained in the previous section in figure (26). In the upper layer of the vegetation and above TKE is generated due to the form drag. Inside the vegetation, the TKE decreases due to the shortcut of the energy cascade. At the leading edge of the pots TKE is also generate due to blockage of the flow. At the trailing edge, the TKE increases again due to recirculation.

It is clear that the results obtained for the temperature are physical. Close to the pots, the temperature is the lowest due to a lack of radiative heat flux and the presence of transpiration. The temperature increases as we move towards to the top of the vegetation and the radiative heat flux increases. At the leading edge of the vegetation the temperature drop is not as

pronounced, because the air has not passed through many leaves yet.

8.4 Difference Scheme Sensitivity

Manickathan et al. [2017] used the Linear Upwind Difference Scheme to model the convection terms in the RANS equations. The LUDS scheme is highly numerically diffusive. This could have an impact on the performance of the Leaf Energy Balance model. Therefore, the aforementioned simulations are repeated using the Quadratic Upwind Differencing Scheme and the Central Differencing Scheme. Profiles are extracted along the $\hat{z}$-axis at $x = 11.57$ m, $y = 7.5$ m. The profiles are displayed in figure (42). The height of the pots is indicated using red lines. The height of the vegetation is indicated using green lines.

The standard deviation of the differences between the results obtained using LUDS versus QUDS and CDS, normalized with the means of the LUDS profiles, are displayed in the following table.

Table 6: The standard deviation of the differences between the results obtained using LUDS versus QUDS and CDS, normalized with the means of the LUDS profiles, extracted at $x = 11.57$ m, $y = 7.5$ m.

	U	k	T	T_{leaf}
CDS	0.0215	0.0466	2.70-03	2.00-03
QUDS	0.0159	0.0672	2.30E-03	6.6167E-04
UDS	0.0144	0.055	3.3E-03	2.20E-03

It is clear that the differencing scheme that is used has some effect on the flow field that is obtained. For the streamwise velocity, the largest difference is observed at $z = 0.5$ m, where the result obtained with CDS is 6% larger than the results obtained with QUDS and LUDS. For the turbulent kinetic energy, the largest difference is observed close to the wall, where the first inflection point is much more pronounced in the profile obtained with CDS. k is roughly 10 % higher in this region. At $z = 0.5$ m, k is roughly 10% lower. In general, CDS and QUDS are comparable to LUDS in the sense of prevalence of numerical diffusion, with the existing mesh.

The effects observed for T and T_{leaf} are negligible.

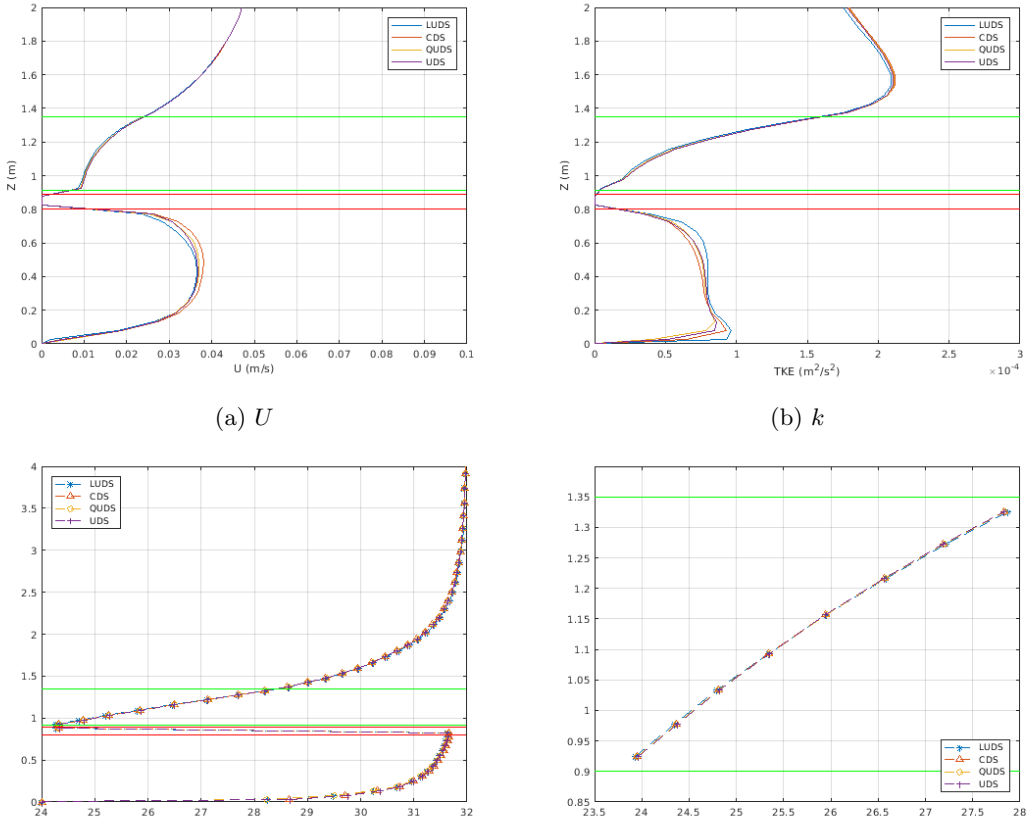

(a) U (b) k

(c) T (d) T_{leaf}

Figure 42: The profiles extracted along the $\hat{z}$-axis at $x = 11.57$ m, $y = 7.5$ m. The heights of the pots and the vegetation are indicated using red and green lines respectively.

Figure 43

9 Discussion

9.1 Concentration

Using the mixed dry deposition model described in section 4, we were able to reproduce the experimental data obtained from Tiwary et al. [2006]. The model acted physically, and showed a positive correlation between the particle diameter and the deposition velocity, and a negative correlation between the leaf size and the dry deposition velocity. The best agreement was obtained for $C_D = 0.19$ and $\phi = 0.37$. These results can be compared with the ones obtained in [Šíp and Beneš, 2016], where similar simulations were performed.
Most results obtained by Šíp and Beneš [2016] were not identical. The authors used a friction velocity of $u_* = 0.189\frac{m}{s}$, compared to $u_* = 0.1903\frac{m}{s}$ in this research. This was seen an acceptable error and was not viewed as a significant. However, the authors obtained the best agreement with the measurements for $C_D = 0.27$ and $\phi = 0.15$. The difference of the drag coefficient can be explained by a number of things.

First, the authors used a 2D simulation. Their mesh of the hedge obstacle consisted of 16 $\times$ 24 control volumes. In this research, the mesh of the hedge obstacle (in 2D), consisted of 22 $\times$ 45 control volumes. The mesh of the hedge obstacle in this research was thus approximately 2.5 times as fine. The authors used the QUICK scheme. However, we have shown in figure (17a) and figure (17b) that the QUICK scheme is highly grid dependent. Secondly, the authors used a standard $k-\epsilon$ turbulence model. However, the authors used the following expression to determine σ_ϵ:

$$\sigma_\epsilon = \frac{\kappa^2}{(C_{\epsilon 2} - C_{\epsilon 1}\sqrt{C_\mu}} \tag{121}$$

as proposed by Richards and Hoxey [1993]. As a result, the authors used $\sigma_\epsilon = 1.167$, instead of the standard $\sigma_\epsilon = 1.3$ [Kenjereš and ter Kuile, 2013]. This implies that the diffusion of ϵ was lower in our research, which influenced the results. Finally, the implementation of the wall functions was different. In this research, the velocity goes to zero as we approach the wall due to the boundary roughness. In the research by Šíp and Beneš [2016] the velocity is finite at the wall. This influences the overall conservation of momentum.

The difference between the obtained value for ϕ is explained by the fact that Šíp and Beneš [2016] use a slightly different model for the inertial impaction. Their model significantly over-predicts the inertial impaction contribution to the dry deposition velocity for Stokes number in the range of $10^0 - 10^1$. This corresponds to the Stokes number that are relevant in this research. Also, the inertial impaction is the most important contribution to the dry deposition velocity for the range of particles that are mentioned in this research. This over-prediction is present for both broad leaf and needle-like collectors.

9.2 Temperature

Two different case studies were examined to determine the effect of our implementation of the leaf energy balance. We tried to obtain the same numerical results that were obtained by Manickathan et al. [2017] for a simple vegetation block, and an actual experimental setup studied by Kichah et al. [2012] and Manickathan et al. [2017].

9.2.1 Parametric study of the influence of environmental factors and tree properties on the transpirative cooling effect of trees

For the simulation case, the heat fluxes agreed perfectly with the numerical results. The T_{leaf} profile was similar to the work by Manickathan et al. [2017], but was 0.1 $°C$ lower at the bottom of the vegetation. This behaviour indicates a slight overestimation of $|q_{sen}|$ near the vegetation.

The overestimation of $|q_{sen}|$ could be caused by the fact that the obtained w field is significantly different from the result obtained by Manickathan et al. [2017]. w increases only to 16.45 $\frac{g}{kg}$ instead of 16.7 $\frac{g}{kg}$. This means that q_{lat} is not being damped as much in this work due to the lack of a local increase of humidity. Also, maximum value of w was expected near the lower trailing edge of the vegetation, while it is observed in the middle of the trailing edge in this work. This means that q_{lat} is not being damped as much locally in this work due to the different humidity contours. The overestimation of q_{sen} is reflected in the result of T, as it is 0.1 $°C$ lower at the bottom of the vegetation.

The difference between the humidity contours obtained in this work and the result by Manickathan et al. [2017], is probably caused by multiple factors. The first being that Manickathan et al. [2017] use a realizable k-ϵ model. The realizable assumes that C_μ is not constant:

$$C_\mu = \frac{1}{A_0 + A_s \frac{k\sqrt{S_{ij}S_{ij}+\hat{\Omega_{ij}}\hat{\Omega_{ij}}}}{\epsilon}} \tag{122}$$

where $A_0 = 4.04$, $A_s = \sqrt{6}\cos\phi$, $\phi = \frac{1}{3}\cos^{-1}\sqrt{6}\frac{S_{ij}S_{jk}S_{ki}}{(S_{ij}S_{ij})^{\frac{3}{2}}}$, $\hat{\Omega_{ij}} = \Omega_{ij} - 2\epsilon_{ijk}\omega_k$, S_{ij} is the strain rate tensor, and Ω_{ij} is the rate of ration tensor in a reference frame rotation with w_k. This means that turbulent viscosity $\mu_t = \rho C_\mu \frac{k^2}{\epsilon}$ will be different, which influences the turbulent diffusion of momentum, k, ϵ, w, and T. Also, Manickathan et al. [2017] used a 2D approach, where the 3D effects of the flow were neglected. The turbulent eddies generated at the North and South faces of the obstacles have an additional effect on the turbulent diffusion. This could influence the overall obtained profiles.
Finally, the authors used a 2D mesh that was finer than the mesh used in this work of the $\hat{x} - \hat{z}$ plane. Their mesh consists of a total number of 40.000 control volumes, with a minimum cell size of 0.01 m $\times$ 0.01 m at the vegetation. Our mesh consisted of 193 $\times$ 85 control volumes, with a minimum cell size of 0.05 m $\times$ 0.05 m at the vegetation. In both works, the Linear Upwind Differencing Schema was used. The LUDS is highly numerically diffusive, especially if the mesh is coarse. In this work the mesh is more coarse, which indicates that numerical diffusion should be more present. This could also affect the obtained results.

9.2.2 Measurement of microclimate characteristics and transpiration of an Impatiens pot plant crop in a greenhouse

In this case study major differences were observed between both the numerical results by Manickathan et al. [2017] and the experimental results by Kichah et al. [2012]. Compared to the measurements and the simulations, the effect of transpirative cooling was to pronounced. The difference is at least 1.5 $°C$ for physical values of l, for all three measuring points. Also, the difference between the results by Manickathan et al. [2017] is even larger, while similar results would be expected based on the previous case study. Again, the use of the realizable $k - \epsilon$ model and a 2D approach explains part of discrepancy. Also, the mesh of the $\hat{x} - \hat{z}$ plane of this work consists of 158 $\times$ 74 control volumes, with a minimum cell size of 0.05 m $\times$ 0.05 m. Manickathan et al. [2017] used 24.000 control volumes with a minimum cell size of 0.01 m $\times$

0.0055 m. This also explains part of the difference between the obtained results.

However, the main difference is caused by the fact that the flow field is not converged. The residuals of the momentum, p, and k are all above 10^{-2} and the residual of ϵ is above 10^{4}. That means that our results are not a perfect solution of the transport equations listed previously. This explains the large differences between our results and the results by Manickathan et al. [2017]. Consequently, our results can not be used to draw any conclusions about the correctness of our implementation with regard to the experimental results. Convergence can not be reached due to the nature of the flow that is being modelled. The friction velocity is 0.004256 $\frac{m}{s}$, which is extremely low. At the vegetation, U is in the order of 10^{-2} $\frac{m}{s}$. This means that Re calculated with the height of the vegetation is in the order 10^{3}. This means that we are dealing with a flow that is barely turbulent. Our implementation of the RANS equations with the $k-\epsilon$ model has not been tested for flows with such a low Reynolds numbers, and the listed test case is right at the boundary of its capabilities. As a result, we are not able to accurately model the flow, temperature and humidity fields.

10 Concluding Remarks

In this research, simulations have been performed to validate the implementation and correctness of numerical models that are used to calculate the influence of vegetation on the transport of pollutants and heat. The dry-deposition model proposed by Petroff et al. [2008] Petroff et al. [2009] was used to model the filtering capacity of the vegetation. The simulations performed by Šíp and Beneš [2016] were repeated using our own implementation, to ensure correctness. The leaf energy balance model, proposed by Kichah et al. [2012], was used to model the cooling effect of the vegetation. The simulations performed by Manickathan et al. [2017] were repeated to ensure correctness. Based on these simulations, the research sub-questions can be answered:

- *Can the existing RANS $k-\epsilon$ solver be extended with a numerical model such that it is able to accurately reproduce experimental measurements of the effect of vegetation on pollution dispersion?*
  The dry-deposition model was successfully used to obtain physical results of the filtering capacity of a hawthorn hedge. Collection of pollutants was assumed to be due to be both needle like and broad leaf collectors, which agrees with the structure of the vegetation that was studied. The obtained value for the drag coefficient agreed well with the result by Šíp and Beneš [2016]. In this research, the filtering capacity of the broad leaves was lower compared to the results by Šíp and Beneš [2016]. As a result, we concluded that a larger portion of the deposition takes place due to needle like collectors. Additional testing is needed to determine the importance of the collection mixing parameter for multiple species.

- *Can the existing RANS $k-\epsilon$ solver be extended with a numerical model such that it is able to accurately reproduce experimental measurements of the effect of vegetation on the dispersion of heat?*
  The leaf energy balance model was used to calculate the influence of vegetation on the temperature. Two scenarios were studied, a pure simulation case study proposed by Manickathan et al. [2017], and an empirical study by Kichah et al. [2012]. Our results agreed very well with the result obtained by Manickathan et al. [2017] for the simulation case. However, we were not able to accurately reproduce the experimental values obtained by Kichah et al. [2012], due to the nature of the flow. As a consequence, we can only validate the implementation of the model, but not the accuracy of the model itself.

11 Recommendations

Based on the work performed in this research, several recommendations are made for further research.

- Additional testing of the dry-deposition model against experimental measurements should be performed. In this study, the main parameter that determines the effectiveness of the model is collection mixing parameter, which controls the amount of collection by needle-like collectors versus broad leaf collectors. Testing the model against pure needle-like collectors, like conifers, or pure broad leaf collectors, like an oak, would reveal if the model can be effective without the need of an extra unknown parameter.
- The leaf energy balance model should be tested against experimental data obtained under different flow conditions. Measurement of the air temperature and/or leaf temperature of vegetation that is subject to higher wind velocities would allow us to determine the physical accuracy of the leaf energy balance model.
- The leaf energy balance model assumes that all the heat needed to evaporate the moisture from the stomata is extracted from the leaves. As a result, the leaf temperature drops, and the air is cooled by the leaves itself. In reality, some of the heat required for evaporation will also be extracted from the air directly. Additional research is needed to determine if this effect is significant.
- The leaf energy balance model has been tested without the presence of a cooled wall on which the vegetation is placed. It is likely that the model will behave differently when this is the case.
- Similarly, the leaf energy balance model has not been tested with thermal buoyancy effects. The additional flow in the vertical plane, induced by the buoyancy effect, will probably alter the transport of temperature and humidity inside the vegetation.

12 Appendix: Code Listings

12.1 Concentration routine

```
!      Calculate Correction Factor
       C_C = 1. + 3.33*LAMBDA_P*(10.**(-6.))/D_P
       RELAX = (RHO_P*C_C*scaling*(D_P**2.))/(18.*DEN(INP)*VISCOS)
       USETTLE = RELAX*9.81

       UVELMOD=SQRT(U(INP)**2+V(INP)**2+W(INP)**2)

       SU(INP) = SU(INP)+USETTLE*(CON(INP+NIJ)-CON(INP-NIJ))/&
       (ZC(INP+NIJ)-ZC(INP-NIJ))*VOL(INP)*scaling

       conctrees : IF(ITREES.EQ.1.AND.PETROFF) THEN

!      Calculate brownian diffusion
       DB = C_C*KB*(T(INP)+273.)*scaling/(3*DEN(INP)*VISCOS &
       *D_P*3.14159265)
       RE_B = UREF*l*scaling/VISCOS
       RE_N = UREF*D_N*scaling/VISCOS

       UBD_N = CB_N*((VIS(INP)/(DB*scaling))**(-2./3.))*&
       RE_N**(N_B)*IB_N*UVELMOD

       UBD_B = CB_B*((VIS(INP)/(DB*scaling))**(-2./3.))*&
       RE_B**(N_B)*IB_B*UVELMOD

!      Calculate interception
       UIN_N = 2.*KX_N*D_P*UVELMOD/D_N
       UIN_B = UVELMOD*(3.*KX_B/8.)*(D_P/l)*(1.5+LOG(8.*l/D_P))

!      Calculate Inertial Impaction
       STM_B = RELAX*UREF/l
       STM_N = RELAX*UREF/D_N

       UIM_B = UVELMOD*0.75*KX_N*((STM_B/BETA_B)**2.)*&
       (2.*(1.+(STM_B**2.)/BETA_B)/(2.+(STM_B**2.)/BETA_B) - &
       (STM_B/BETA_B)*LOG(1.+2.*BETA_B/STM_B))

       UIM_N = UVELMOD*KX_N*0.5*((STM_N/BETA_N)**2.)*&
       (1./(1.+2.*BETA_N/STM_N)+LOG(1.+2.*BETA_N/STM_N)-1.)


!      Turbulent Impaction
       RELAXSTAR = RELAX*scaling*(UFRICTION**2.)/VISCOS
       IF(RELAXSTAR.LT.20) THEN
         UTI = UFRICTION*KTI1*(RELAXSTAR**2.)
       ElSE
```

```
        UTI = UFRICTION*KTI2
      END IF

!     Sedimentation
      USEDI_N = USETTLE*KZ_N
      USEDI_B = USETTLE*KZ_B

!     Compute totals
      UTOTAL_N = UBD_N+UIN_N+UIM_N+UTI+USEDI_N
      UTOTAL_B = UBD_B+UIN_B+UIM_B+UTI+USEDI_B

!      PRINT *,UTOTAL_B,UTOTAL_N
      SU(INP)=SU(INP)-VOL(INP)*&
      CON(INP)*(DISTRIBUTION*UTOTAL_N + &
      (1-DISTRIBUTION)*UTOTAL_B)*&
      POROSITY(INP)


      END IF conctrees
```

12.2 Temperature Routine

```
      trees : IF(ITREES.EQ.1) THEN
!-----Old implementation,deprecated---------------
!-----> here we assume: PC=f(LAD)=C*LAD : 250 < C < 335, Cp=1005. --> Sink = C*LAD
!      SU(INP) = SU(INP) - 300.*POROSITY(INP)*VOL(INP)/1005.
!      PRINT *,'SINK',300.*POROSITY(INP)/1005.

!-----Leaf Energy Balance Model-------------------
!-----Added by E. Tierolff 01/18-------------------
      UVELMOD=SQRT(U(INP)**2+V(INP)**2+W(INP)**2)
!-----Calculate aerodynamic resistamce
      IF(POROSITY(INP).GT.0.0) THEN
        r_a = C_T *((1/UVELMOD)**0.5)
!-----Calculate the gradients of LW and SW, LAD is homogeneous
        NABLA_LW = C_LW*q_r_lw/(HEIGHT-LB_TREE)
        q_r_sw = q_r_sw_0*EXP(-BETA_EXT*POROSITY(INP)*(HEIGHT*scaling-ZC(INP)))
        NABLA_SW = q_r_sw*POROSITY(INP)*scaling*BETA_EXT
!-----Calculate the saturated vapor pressure and the R_H
        P_VSAT = 0.61094*EXP(17.625*T(INP)/(T(INP)+243.04 ))!kPa
        IF(LCAL(IHUM)) THEN
          P_VAPOR = HUM(INP)*(10.**5 + P(INP))/(0.62198+HUM(INP))!Pa
          R_H = P_VAPOR/(P_VSAT*1000)
        END IF
        DIFF = (1.-R_H)*P_VSAT
!-----Calculate the stomatal resitance
        r_s = r_s_min*(A1+q_r_sw)/(A2+q_r_sw)*(1+A3*(DIFF-D_0)**2.)
!-----Calculate radiative  flux
        q_rad = (NABLA_LW + NABLA_SW)/(POROSITY(INP)*scaling)
!-----Guess the leaf temperature and calcualate
```

```
          T_LEAF = T(INP)
          T_LEAF_0 = 0.
          counter = 0
          DO WHILE ((ABS(T_LEAF-T_LEAF_0).GT.10.**(-5.))&
          .AND.(counter.LT.20))
            P_VLEAF = 0.61094*EXP(17.625*T_LEAF/&
            (T_LEAF+243.04 ))
            q_lat = L_v*DEN(INP)*R_air*(P_VLEAF-R_H*P_VSAT)*(10.**3.)&
            /((10.**5 + P(INP))*R_vapor*(r_a+r_s))

            T_LEAF_0 = T_LEAF
            T_LEAF = T(INP)+r_a*(q_rad-q_lat)/(2.*DEN(INP)*1005.)
            counter = counter +1
            IF (counter.GT.20) THEN
              PRINT *, counter
            END IF
          END DO
          SU(INP) = SU(INP) + 2.*POROSITY(INP)*(T_LEAF-T(INP))*&
          DEN(INP)*VOL(INP)/r_a
!-----Save the characteristics to the arrays 10/2/2018
          TLEAF(INP) = T_LEAF
          r_a_array(INP) = r_a
          r_s_array(INP) = r_s
          q_rad_array(INP) = q_rad
          q_lat_array(INP) = q_lat
          q_r_sw_array(INP) = q_r_sw
          R_H_array(INP) = R_H
        END IF
        END IF trees
```

12.3 Humidity Routine

```
! Added by E.T. Tierolff 12/2/2018
        IF(POROSITY(INP).GT.0.0) THEN
          IF (LCAL(IEN)) THEN
            SU(INP) = SU(INP)+q_lat_array(INP)*POROSITY(INP)*&
            VOL(INP)/(L_v)
          ELSE
            UVELMOD=SQRT(U(INP)**2+V(INP)**2+W(INP)**2)
            r_a = C_T *((1/UVELMOD)**0.5)
!-----Calculate the gradients of LW and SW, LAD is homogeneous
            NABLA_LW = C_LW*q_r_lw/(HEIGHT-LB_TREE)
            q_r_sw = q_r_sw_0*EXP(-BETA_EXT*POROSITY(INP)*(HEIGHT*scaling-ZC(INP)))
            NABLA_SW = q_r_sw*POROSITY(INP)*scaling*BETA_EXT
!-----Calculate the saturated vapor pressure and the R_H
            P_VSAT = 0.61094*EXP(17.625*T(INP)/(T(INP)+243.04 ))!kPa
            IF(LCAL(IHUM)) THEN
              P_VAPOR = HUM(INP)*(10.**5 + P(INP))/(0.62198+HUM(INP))!Pa
              R_H = P_VAPOR/(P_VSAT*1000)
            END IF
```

```
          DIFF = (1.-R_H)*P_VSAT
!-----Calculate the stomatal resitance
          r_s = r_s_min*(A1+q_r_sw)/(A2+q_r_sw)
!-----Calculate radiative  flux
          q_rad = (NABLA_LW + NABLA_SW)/(POROSITY(INP)*scaling)
!-----Guess the leaf temperature and calcualate
          T_LEAF = T(INP)
          T_LEAF_0 = 0.
          counter = 0
          DO WHILE ((ABS(T_LEAF-T_LEAF_0).GT.10.**(-5.))&
          .AND.(counter.LT.20))
            P_VLEAF = 0.61094*EXP(17.625*T_LEAF/&
            (T_LEAF+243.04 ))
            q_lat = L_v*DEN(INP)*R_air*(P_VLEAF-R_H*P_VSAT)*(10.**3.)&
            /((10.**5 + P(INP))*R_vapor*(r_a+r_s))
            T_LEAF_0 = T_LEAF
            T_LEAF = T(INP)+r_a*(q_rad-q_lat)/(2.*DEN(INP)*1005.)
            counter = counter +1
            IF (counter.GT.20) THEN
              PRINT *, counter
            END IF
          END DO
          SU(INP) = SU(INP)!+  q_lat*POROSITY(INP)*VOL(INP)/L_v
          TLEAF(INP) = T_LEAF
          r_a_array(INP) = r_a
          r_s_array(INP) = r_s
          q_rad_array(INP) = q_rad
          q_lat_array(INP) = q_lat
          q_r_sw_array(INP) = q_r_sw
          R_H_array(INP) = R_H
        END IF
      END IF
```

References

LH Allen. Plant responses to rising carbon dioxide and potential interactions with air pollutants. *Journal of Environmental Quality*, 19(1):15–34, 1990.

Jong-Jin Baik, Jae-Jin Kim, and Harindra JS Fernando. A cfd model for simulating urban flow and dispersion. *Journal of Applied Meteorology*, 42(11):1636–1648, 2003.

Dennis D Baldocchi, Bruce B Hicks, and Pamela Camara. A canopy stomatal resistance model for gaseous deposition to vegetated surfaces. *Atmospheric Environment (1967)*, 21(1):91–101, 1987.

MJ Barnes, Thomas K Brade, A Robert Mackenzie, JD Whyatt, DJ Carruthers, Jenny Stocker, Xiaoming Cai, and CN Hewitt. Spatially-varying surface roughness and ground-level air quality in an operational dispersion model. *Environmental pollution*, 185:44–51, 2014.

William L Bauerle, Joseph D Bowden, G Geoff Wang, and Mohamed A Shahba. Exploring the importance of within-canopy spatial temperature variation on transpiration predictions. *Journal of experimental botany*, 60(13):3665–3676, 2009.

NM Darrall. The effect of air pollutants on physiological processes in plants. *Plant, Cell & Environment*, 12(1):1–30, 1989.

Argiro Dimoudi and Marialena Nikolopoulou. Vegetation in the urban environment: microclimatic analysis and benefits. *Energy and buildings*, 35(1):69–76, 2003.

MA E Cunningham. On the velocity of steady fall of spherical particles through fluid medium. *Proc. R. Soc. Lond. A*, 83(563):357–365, 1910.

Panagiotis Gkatsopoulos. A methodology for calculating cooling from vegetation evapotranspiration for use in urban space microclimate simulations. *Procedia Environmental Sciences*, 38:477–484, 2017.

Christof Gromke and Bert Blocken. Influence of avenue-trees on air quality at the urban neighborhood scale. part i: Quality assurance studies and turbulent schmidt number analysis for rans cfd simulations. *Environmental Pollution*, 196:214–223, 2015.

Christof Gromke, Bert Blocken, Wendy Janssen, Bart Merema, Twan van Hooff, and Harry Timmermans. Cfd analysis of transpirational cooling by vegetation: Case study for specific meteorological conditions during a heat wave in arnhem, netherlands. *Building and environment*, 83:11–26, 2015.

Carlo Gualtieri, Athanasios Angeloudis, Fabian Bombardelli, Sanjeev Jha, and Thorsten Stoesser. On the values for the turbulent schmidt number in environmental flows. *Fluids*, 2 (2):17, 2017.

Hisashi Hiraoka. An investigation of the effect of environmental factors on the budgets of heat, water vapor, and carbon dioxide within a tree. *Energy*, 30(2):281–298, 2005.

Daniel J Jacob and Darrell A Winner. Effect of climate change on air quality. *Atmospheric environment*, 43(1):51–63, 2009.

Antoine PR Jeanjean, G Hinchliffe, WA McMullan, Paul S Monks, and Roland J Leigh. A cfd study on the effectiveness of trees to disperse road traffic emissions at a city scale. *Atmospheric Environment*, 120:1–14, 2015.

Gabriel G Katul, Larry Mahrt, Davide Poggi, and Christophe Sanz. One-and two-equation models for canopy turbulence. *Boundary-Layer Meteorology*, 113(1):81–109, 2004.

Saša Kenjereš and Benjamin ter Kuile. Modelling and simulations of turbulent flows in urban areas with vegetation. *Journal of wind engineering and industrial aerodynamics*, 123:43–55, 2013.

Abderzak Kichah, Pierre-Emmanuel Bournet, Christophe Migeon, and Thierry Boulard. Measurement and cfd simulation of microclimate characteristics and transpiration of an impatiens pot plant crop in a greenhouse. *Biosystems engineering*, 112(1):22–34, 2012.

BE Launder and BI Sharma. Application of the energy-dissipation model of turbulence to the calculation of flow near a spinning disc. *Letters in heat and mass transfer*, 1(2):131–137, 1974.

L Manickathan, T Defraeye, J Allegrini, D Derome, and J Carmeliet. Transpirative cooling potential of vegetation in urban environment using coupled cfd and leaf energy balance model. *Advance online publication*, 2017.

Particulate Matter and Unsafe Water Supply. Environmental outlook to 2050. 2012.

E Gregory McPherson, David Nowak, Gordon Heisler, Sue Grimmond, Catherine Souch, Rich Grant, and Rowan Rowntree. Quantifying urban forest structure, function, and value: the chicago urban forest climate project. *Urban ecosystems*, 1(1):49–61, 1997.

Frans TM Nieuwstadt, Jerry Westerweel, and Bendiks J Boersma. *Turbulence: introduction to theory and applications of turbulent flows*. Springer, 2016.

David J Nowak et al. The effects of urban trees on air quality. *USDA Forest Service*, pages 96–102, 2002.

Alexandre Petroff, Alain Mailliat, Muriel Amielh, and Fabien Anselmet. Aerosol dry deposition on vegetative canopies. part ii: A new modelling approach and applications. *Atmospheric Environment*, 42(16):3654–3683, 2008.

Alexandre Petroff, Leiming Zhang, SC Pryor, and Yves Belot. An extended dry deposition model for aerosols onto broadleaf canopies. *Journal of Aerosol Science*, 40(3):218–240, 2009.

MA Rahman, JG Smith, P Stringer, and AR Ennos. Effect of rooting conditions on the growth and cooling ability of pyrus calleryana. *Urban forestry & Urban greening*, 10(3):185–192, 2011.

PJ Richards and RP Hoxey. Appropriate boundary conditions for computational wind engineering models using the $k-\epsilon$ turbulence model. *Journal of wind engineering and industrial aerodynamics*, 46:145–153, 1993.

Limor Shashua-Bar, David Pearlmutter, and Evyatar Erell. The cooling efficiency of urban landscape strategies in a hot dry climate. *Landscape and Urban Planning*, 92(3-4):179–186, 2009.

Viktor Šíp and Luděk Beneš. Rans solver for microscale pollution dispersion problems in areas with vegetation: Development and validation. *arXiv preprint arXiv:1609.03427*, 2016.

William H Smith. Air pollution—effects on the structure and function of the temperate forest ecosystem. *Environmental Pollution (1970)*, 6(2):111–129, 1974.

Haider Taha. Urban climates and heat islands: albedo, evapotranspiration, and anthropogenic heat. *Energy and buildings*, 25(2):99–103, 1997.

T Takakura, S Kitade, and E Goto. Cooling effect of greenery cover over a building. *Energy and Buildings*, 31(1):1–6, 2000.

Laurens Tan. *Numerical comparison of models for vegetation effects on airflows using the $k-\epsilon$ turbulence model*. PhD thesis, Technical University Delft, 2009.

Abhishek Tiwary, Hervé P Morvan, and Jeremy J Colls. Modelling the size-dependent collection efficiency of hedgerows for ambient aerosols. *Journal of Aerosol Science*, 37(8):990–1015, 2006.

Abhishek Tiwary, Adam Reff, and Jeremy J Colls. Collection of ambient particulate matter by porous vegetation barriers: sampling and characterization methods. *Journal of Aerosol Science*, 39(1):40–47, 2008.

Yoshihide Tominaga and Ted Stathopoulos. Turbulent schmidt numbers for cfd analysis with various types of flowfield. *Atmospheric Environment*, 41(37):8091–8099, 2007.

United Nations. World urbanization prospects: The 2014 revision, highlights. department of economic and social affairs. *Population Division, United Nations*, 2014.

World Health Organization. Who air quality guidelines for particulate matter, ozone, nitrogen dioxide and sulfur dioxide-global update 2005-summary of risk assessment, 2006. *Geneva: WHO*, 2006.

An-Shik Yang, Yu-Hsuan Juan, Chih-Yung Wen, and Chao-Jui Chang. Numerical simulation of cooling effect of vegetation enhancement in a subtropical urban park. *Applied Energy*, 192: 178–200, 2017.